Coronary Artery Plaque Assessment with Fast Switched Dual Energy X-Ray Computed Tomography Angiography

by

Thomas Boltz

A Dissertation Presented in Partial Fulfillment
of the Requirements for the Degree
Doctor of Philosophy

Approved November 2013 by the
Graduate Supervisory Committee:

David Frakes, Chair
Bruce Towe
Vikram Kodibagkar
William Pavlicek
Charles Bouman

ARIZONA STATE UNIVERSITY

December 2013

ABSTRACT

Coronary computed tomography angiography (CTA) has a high negative predictive value for ruling out coronary artery disease with non-invasive evaluation of the coronary arteries. My work has attempted to provide metrics that could increase the positive predictive value of coronary CTA through the use of dual energy CTA imaging. After developing an algorithm for obtaining calcium scores from a CTA exam, a dual energy CTA exam was performed on patients at dose levels equivalent to levels for single energy CTA with a calcium scoring exam. Calcium Agatston scores obtained from the dual energy CTA exam were within ±11% of scores obtained with conventional calcium scoring exams. In the presence of highly attenuating coronary calcium plaques, the virtual non-calcium images obtained with dual energy CTA were able to successfully measure percent coronary stenosis within 5% of known stenosis values, which is not possible with single energy CTA images due to the presence of the calcium blooming artifact. After fabricating an anthropomorphic beating heart phantom with coronary plaques, characterization of soft plaque vulnerability to rupture or erosion was demonstrated with measurements of the distance from soft plaque to aortic ostium, percent stenosis, and percent lipid volume in soft plaque. A classification model was developed, with training data from the beating heart phantom and plaques, which utilized support vector machines to classify coronary soft plaque pixels as lipid or fibrous. Lipid versus fibrous classification with single energy CTA images exhibited a 17% error while dual energy CTA images in the classification model developed here only exhibited a 4% error. Combining the calcium blooming correction and the percent lipid volume methods developed in this work will provide physicians with metrics for increasing the positive predictive value of coronary CTA as well as expanding the use of coronary CTA to patients with highly attenuating calcium plaques.

ACKNOWLEDGMENTS

This body of work was achieved through the efforts and thoughts of several people. I would like to thank Dr. William Pavlicek and Gene Paden for their mentorship on the medical physics aspects of this work. I would also like to thank Dr. David Frakes for his continued teaching of engineering principles applicable to clinical imaging solutions. Financial support was provided both by Mayo Clinic Arizona and Arizona State University.

TABLE OF CONTENTS

CHAPTER Page

CHAPTER Page

LIST OF TABLES

Table Page

LIST OF FIGURES

Figure Page

CHAPTER 1 ABSTRACT AND SPECIFIC AIMS

ABSTRACT

Coronary computed tomography angiography (CTA) has a high negative predictive value for ruling out coronary artery disease with non-invasive evaluation of the coronary arteries. My work has attempted to provide metrics that could increase the positive predictive value of coronary CTA through the use of dual energy CTA imaging. After developing an algorithm for obtaining calcium scores from a CTA exam, a dual energy CTA exam was performed on patients at dose levels equivalent to levels for single energy CTA with a calcium scoring exam. Calcium Agatston scores obtained from the dual energy CTA exam were within ±11% of scores obtained with conventional calcium scoring exams. In the presence of highly attenuating coronary calcium plaques, the virtual non-calcium images obtained with dual energy CTA were able to successfully measure percent coronary stenosis within 5% of known stenosis values, which is not possible with single energy CTA images due to the presence of the calcium blooming artifact. After fabricating an anthropomorphic beating heart phantom with coronary plaques, characterization of soft plaque vulnerability to rupture or erosion was demonstrated with measurements of the distance from soft plaque to aortic ostium, percent stenosis, and percent lipid volume in soft plaque. A classification model was developed, with training data from the beating heart phantom and plaques, which utilized support vector machines to classify coronary soft plaque pixels as lipid or fibrous. Lipid versus fibrous classification with single energy CTA images exhibited a 17% error while dual energy CTA images in the classification model developed here only exhibited a 4% error. Combining the calcium blooming correction and the percent lipid volume methods developed in this work will provide physicians with metrics for increasing the positive predictive value of coronary CTA as well as expanding the use of coronary CTA to patients with highly attenuating calcium plaques.

1.1 Aim 1: Engineer Anthropomorphic Beating Heart Phantom

In order to develop coronary plaque assessment methods from dual energy CT imaging, comparisons had to be made between existing methods and proposed methods. Aim 1 was to engineer an anthropomorphic beating heart phantom with variable heart rates, injected iodine contrast material, and soft plaques deposits. The engineered phantom provided the initial comparisons crucial for validating the proposed methods that would be successful in patient imaging.

1.2 Aim 2: Quantify Coronary Calcium Plaque with Dual Energy CT Angiography

Single energy cardiac imaging requires one non-iodinated scan for coronary calcium quantification and one iodinated scan for coronary artery patency assessment. Dual energy cardiac imaging has the added benefit of quantifying vessel patency and possibly lipid content, but one dual energy scan requires the radiation dose of two single energy scans. Aim 2 was to develop a method for quantifying calcium from an iodinated dual energy scan. This would make it possible to perform dual energy cardiac imaging at the same radiation dose as single energy cardiac imaging but with the added benefit of tissue/material quantification.

1.3 Aim 3: Correct Calcium Blooming Artifact with Dual Energy CT Angiography

Conventional polychromatic images are susceptible to the calcium blooming artifact in coronary arteries. In the presence of highly attenuating or densely populated coronary calcium plaques, window and level settings with polychromatic images can cause the calcium blooming artifact and potentially misrepresent the stenosis due to calcium plaque. Aim 3 was to correct for the calcium blooming artifact through the use of DECT material basis images which can remove calcium from the DECT angiographic images. With calcium removed in the DECT material basis images, accurate stenosis evaluation could be made with non-invasive DECT imaging.

1.4 Aim 4: Characterize Coronary Soft Plaque Vulnerability with Dual Energy CT Angiography

Several characteristics of coronary soft plaque indicate the vulnerability to rupture or erosion, and lipid volume in soft plaque is perhaps the most important characteristic given that 80% of all coronary events are due to rupture involving lipid content. Unfortunately, single energy techniques are unable to accurately quantify lipid content due to beam hardening effects. Aim 4 was to characterize coronary soft plaque vulnerability by quantifying lipid volume in soft plaques using a Support Vector Machine model with multiple dual energy image types such as virtual monochromatic and material basis images. With accurate lipid volume measurements, soft plaque vulnerability and risk of coronary events could be developed.

CHAPTER 2 BACKGROUND AND CLINICAL SIGNIFICANCE

Cardiovascular disease is responsible for 30% of all deaths worldwide each year (Guilbert 2003). Cardiovascular disease includes myocardial infarction, angina, coronary insufficiency, coronary death, stroke, transient ischemic attacks, congestive heart failure, hypertension, valvular heart defects, and congenital heart defects (Fuster 2008). Myocardial infarction was selectively assessed on an international level by the INTERHEART study, which identified the mitigating risk factors for myocardial infarction across 52 countries (Yusuf et al. 2004). The INTERHEART study enrolled about 15,000 individuals who had an initial myocardial infarction (MI) and another 15,000 individuals for control cases who were sex-matched and age-matched to the MI cases within ±5 years. The study found 9 risk factors to be significantly related to acute myocardial infarction: smoking, raised ApoB100/ApoA1 ratio, hypertension, diabetes, abdominal obesity, psychosocial factors, poor daily fruits and vegetables consumption, regular alcohol consumption, and lack of regular physical activity ($p<0.0001$ for all risk factors). These risk factors strongly indicate the risk of an initial acute myocardial infarction for men and women, across different geographical regions and across ethnic groups. Overall, the INTERHEART study reported that smoking and increased lipid levels (ApoB100/ApoA1) are the most important risk factors to consider for risk of initial myocardial infarction. The increased risk from smoking and increased lipid levels can be explained by the direct role they play in the cardiovascular damage and repair process.

2.1 Pathology of Coronary Artery Plaque

Healthy arteries of the cardiovascular system have arterial walls free of the excess buildup of lipid, scar tissue, or calcium found in arteries with arteriosclerosis and/or atherosclerosis. The healthy arterial wall is comprised of 5 layers: vasa vasorum, external lamina, collagen matrix/smooth muscle, internal lamina, and endothelium as shown in Figure 2.2 (Fuster

2008). The layer of vasa vasorum is the outermost layer of the arterial wall and has small capillaries that supply blood to the arterial wall itself. An elastic coating known as the external lamina separates the outer layer from the middle layer. The collagen matrix and smooth muscle comprise the middle layer of the arterial wall, providing structural support as well as facilitating vasodilation and vasoconstriction. An elastic coating known as the internal lamina separates the middle layer from the inner layer. The inner layer of the arterial wall is a layer of endothelial cells that secretes vasoactive molecules, protects against thrombus formation, and prevents blood from the arterial lumen from entering the arterial wall. Blood flows through the arterial lumen. Arterial plaques most often form within the inner endothelial layer of the arterial wall.

Arteriosclerosis and atherosclerosis are the processes by which healthy arteries become diseased with plaque buildup. In the case of arteriosclerosis, the layer of vasa vasorum leaks excess lipid into the arterial wall (Fuster 2008). The vasa vasorum leaks in response to toxic conditions created by smoking and other risk factors such as those identified by the INTERHEART study. When the excess lipid accumulates across the length of the arterial wall without forming atheroma, the vessel is said to be arteriosclerotic and the arterial wall thickens in response to the excess lipid plaque. The lipid plaque can settle over time to form scar tissue that is more stable than lipid. Positive remodeling occurs as arteriosclerosis causes the artery's diameter to increase while maintaining the luminal diameter, preventing any reduction in the luminal area available for blood flow. Figure 2.1 outlines the distribution of coronary failure mechanisms from both atherosclerosis and arteriosclerosis, relating the distribution of deaths caused by myocardial infarction to deaths from other causes in the United States.

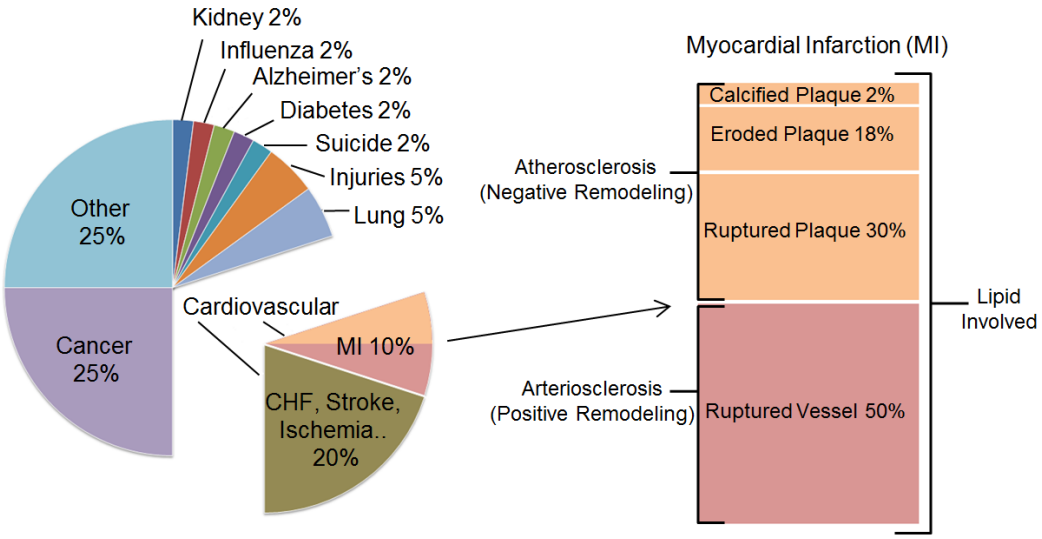

Figure 2.1: Causes of Death in the United States (CDC 2008). The pie graph shows the impact of myocardial infarction (MI) as a leading cause of death in the United States (Heron 2012). The mechanisms involved with myocardial infarction are outlined in the bar graph (Virmani et al. 2000).

Noting the mechanisms of myocardial infarction in Figure 2.1, it is clear that lipid has involvement in all myocardial infarction events. In the case of atherosclerosis, atheroma forms along the inner arterial wall as lipid deposits there. As damage occurs to the inner endothelial layer, the collagen matrix, smooth muscle, and excess lipids are exposed to the lumen of the artery. The inflammatory process then attempts to repair the exposed area by scarring the exposed collagen, smooth muscle, and lipid to form a plaque known as an atheroma attached to the arterial wall. The damage to the inner endothelial layer is most likely due to toxic conditions created by smoking and other risk factors such as those identified by the INTERHEART study. Macrophages and T-lymphocytes cause the exposed plaque to scar along its surface area, creating the fibrous cap atheroma (Virmani et al. 2000). The progression of arterial wall disease is demonstrated in Figure 2.2.

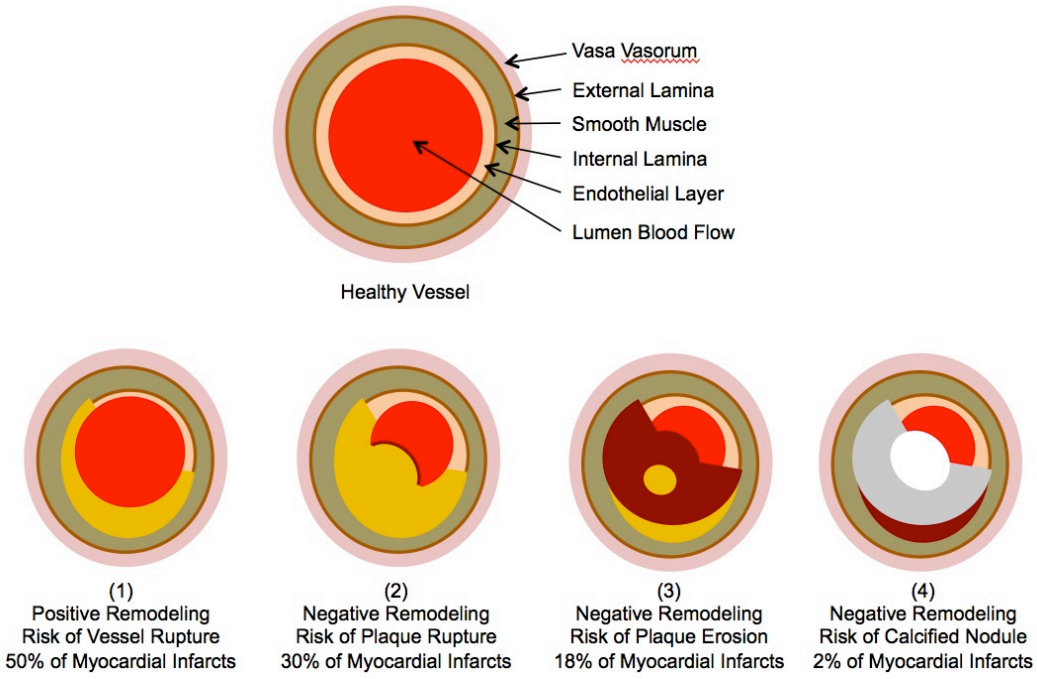

Figure 2.2: Coronary artery plaque pathology. The healthy arterial wall anatomy is shown in the "Healthy Vessel" image. The stages of coronary artery disease are shown in images (1) through (4).

As time passes, the fibrous cap atheroma either calcifies or increases in lipid content to the point that it ruptures. The fibrous cap atheroma may calcify as a result of dying smooth muscle or macrophages (Kolodgie et al. 2007). An example of a calcified atheroma is seen in image (4) of Figure 2.2. The fibrous cap atheroma may also accumulate more lipid, such that 25% or more of the plaque area is lipid, and become vulnerable to rupture when its thin cap is <65um thick, sending a thrombus into the arterial blood flow in the event of rupture (Burke et al. 1997; Finn et al. 2010). Negative remodeling occurs as the atheroma protrudes into the lumen and reduces the available luminal area for blood flow. Figure 2.2 shows the lipid rich atheroma in image (2) and the more fibrous atheroma in image (3).

Ruptured plaques commonly have an intraluminal thrombus overlying a broken thin fibrous cap in contact with an underlying necrotic core (Farb et al. 1996; Ge et al. 1999). The necrotic core houses fibrous platelet tissue as well as the lipid pool. Eroded plaques still have the fibrous cap in place but have dislodged from the arterial wall, blocking blood flow (Kolodgie et al.

2002). Important characteristics of eroded plaques include abundance of smooth muscle cells and proteoglycan matrix with the absence of a prominent lipid core. Post-mortem measurements have shown that patients with sudden cardiac death and acute myocardial infarction had ruptured plaques 55%-75% of the time, eroded plaques 25%-40% of the time, and calcified nodules 2%-7% of the time (Virmani et al. 2000). The distribution graphs in Figure 2.1 distinguish myocardial infarction as responsible for 10% of deaths in the whole United States, and emphasize how lipid is involved in all the mechanisms associated with myocardial infarction (Heron 2012). Results from the INTERHEART study also emphasize the high significance of increased lipids as increasing the risk of myocardial infarction. Therefore, coronary computed tomography angiography has been used to quantify the extent of cardiovascular disease present in terms of lipid quantification, calcium quantification, and stenosis evaluation (Lau et al. 2005).

2.2 Coronary Artery Plaque Assessment with Single Energy CT

Computed tomography of the heart is an established test for non-invasive assessment of the coronary arteries (Gerber, Kantor, and Williamson 2007; Achenbach et al. 2004). Single energy cardiac CT involves the acquisition of both a non-iodinated image set and an iodinated image set. The non-iodinated image set is used to quantify calcium with either an Agatston score, a calcium mass score, or a calcium volume score (Ulzheimer and Kalender 2003). In accordance with electron beam computed tomography measurements, axial plane images from the non-iodinated scan are used to calculate calcium scores (Becker et al. 2001). The iodinated image set is considered to be the coronary computed tomography angiography (CCTA) portion of the cardiac CT exam. Single energy CCTA acquisitions can be used to create polychromatic images of five specific planes of the heart (O'Brien et al. 2007; Achenbach et al. 2006). The first image plane of interest is the axial plane, which is used to orient the radiologist with the patient's specific anatomy. Three more image planes are direct oblique reformats created from the axial image plane. The fifth image plane is known as a center seeking curved multiplanar reformat, which

visualizes the iodinated coronary arteries individually. Coronary stenosis evaluation is heavily dependent on these five image sets. As the coronary arteries are evaluated, percent stenosis of 70% or more is considered hemodynamically significant, which means that tissues below the blockage are in danger of receiving insufficient blood supply and myocardial ischemia.

If stenosis is caused by low density plaques in low amounts, then single energy CCTA images are sufficient for percent stenosis evaluation (Raff et al. 2005). Plaque evaluation is also performed on the five image sets from single energy CCTA. Plaque density can be used to indicate the likelihood of coronary events, including myocardial infarction. High density plaques, such as calcified plaques, indicate lower risk of coronary events, but may hinder the accuracy of percent stenosis measurements due to the calcium blooming artifact exhibited in single energy polychromatic images (Raff et al. 2005; Nakanishi et al. 2005). Low density plaques, such as lipid and fibrous plaques, indicate higher risk of coronary events, but may be difficult to quantify given the energy dependence exhibited by single energy polychromatic images (Hausleiter et al. 2006).

2.3 Proposed Coronary Plaque Assessment with Dual Energy CT

Proposed dual energy cardiac imaging would require the collection of two full polychromatic image sets at high and low x-ray energies, nominally 140kVp and 80kVp. One dual energy scan is then equivalent in radiation exposure to two single energy scans. For this reason, proposed dual energy cardiac imaging acquires one iodinated cardiac scan with dual energy technology (Pavlicek et al. 2010). The iodinated exam involves injection of iodine contrast material into the coronary arteries in order to visualize blood flow and plaques. The iodinated dual energy cardiac exam is proposed because it has the potential to meet and surpass the clinical goals that single energy cardiac imaging attempts to achieve. Dual energy cardiac imaging produces image types not possible with single energy cardiac imaging, including virtual monochromatic images and material basis pair images (Barreto et al. 2008). The projection

measurements from 80kVp and 140kVp can be used to solve for the equivalent combination of any two materials from the linear attenuation values as shown in Figure 2.3.

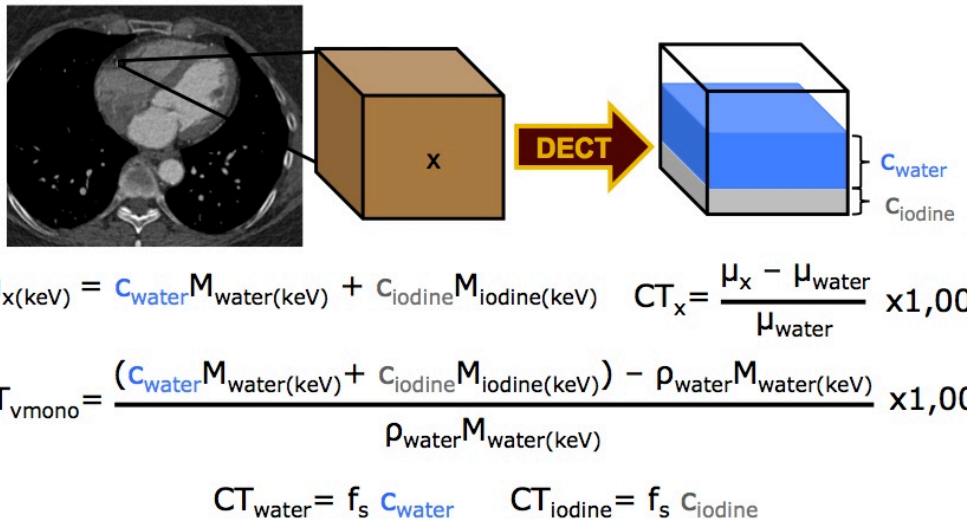

Figure 2.3: Dual energy CT image derivations. Shown are the derivations from the 80kVp and 140kVp measurements as well as the attenuation values listed in the data provided by the National Institute of Standards and Tests. For the example provided here, virtual monochromatic images have voxel values represented by the CT_{vmono} equation and material basis images have voxel values represented by the CT_{water} and CT_{iodine} values.

Although iodine and water were chosen for the derivation in Figure 2.3, any two materials can be used to create material basis images. An axial set of virtual non-iodinated images, using the materials calcium and iodine, can be made from dual energy cardiac imaging for Agatston scoring (Chapter 4). The five image planes of the heart can be made with virtual non-calcium images that correct for the calcium blooming artifact seen with single energy polychromatic images (Chapter 5). Lastly, dual energy cardiac image types can be used to quantify the amount of lipid present in the coronary arteries (Chapter 6). Dual energy cardiac imaging potentially achieves calcium blooming artifact correction, accurate percent stenosis evaluation regardless of plaque density, and lipid quantification, allowing for more patients to be eligible for and accurately evaluated with non-invasive dual energy cardiac imaging.

2.4 Goals and Problems with Calcium Plaque Quantification

Cardiac CT imaging aims to meet the clinical goal of assessing the extent of cardiovascular disease present in the heart. The Agatston score obtained with cardiac CT imaging is one method for quantifying the extent to which the coronary artery walls have undergone the damage and repair process described in Figure 2.2. Percent stenosis measurement from coronary CT angiography is a method for determining the hemodynamic health of the heart. Coronary CT angiography requires the injection of iodine contrast into the blood stream of the patient being imaged. Without injection of iodine, the blood would be too difficult to visualize on the resulting CT image, making the chambers and arteries that the blood fills difficult to visualize. Once iodine is injected into the blood stream, the blood distribution throughout the heart can be seen on the resulting CT image because iodine attenuates x-rays more highly than blood alone or the tissues of the heart. Iodine is so highly attenuating that it matches the CT values of severely calcified plaques, which is the reason that single energy imaging requires a separate non-iodinated scan to evaluate calcium (Muhlenbruch et al. 2005). The proposed dual energy cardiac CT imaging would obtain one iodinated scan, which would have calcified and iodinated pixels at nearly equivalent CT values. For this reason, dual energy acquired material basis images were investigated for use in quantifying calcified plaques even in the presence of iodine (Chapter 4).

2.5 Goals and Problems with Calcium Plaque Assessment for Coronary Artery Stenosis Evaluation

For coronary artery stenosis evaluation, the injected highly attenuating iodine allows for quick identification of stenosis along the length of the coronary arteries. Once stenosis is observed, the clinical goal is to quantify the percent stenosis. Percent stenosis over 70% is considered hemodynamically significant in that it may be reducing blood flow to the extent that tissues below the stenosis begin to die. In cases of stenosis caused by large amounts or highly

dense calcified plaques, the measured value of the percent stenosis has been shown to be inaccurate with single energy polychromatic images. The clinical goal of stenosis assessment depends on properly visualizing and measuring the percent stenosis in the coronary arteries. Percent stenosis is calculated from the luminal area measured with no stenosis and the luminal area measured where stenosis is present. If calcified plaques are causing the stenosis, then the visualization and measurement of the luminal area may be underestimated as a result of the closely attenuating values from calcium and iodine as well as the dependence of polychromatic images on window and level settings (Leber et al. 2005; Raff et al. 2005). To overcome window and level dependency in the presence of calcified plaques, dual energy acquired material basis images were investigated since they can be used to generate virtual non-calcium images (Chapter 5).

2.6 Goals and Problems with Soft Plaque Assessment for Coronary Artery Lipid Quantification

Another clinical goal for cardiac CT imaging is the assessment of soft plaques in order to quantify the amount of lipid present. Soft plaques consist of fibrous tissues (mass density 1.2-1.35g/cc) and lipid tissues (mass density 0.9-0.99g/cc). Without injecting iodine, soft plaques can not be visualized because their attenuation values are too close to the attenuation values of blood and myocardial tissue. Once iodine is injected, soft plaques associated with negative remodeling can be identified because the blood-iodine mixture is much more attenuating than soft plaque. However, iodine presence is known to cause beam hardening artifacts in surrounding tissues (Pohle et al. 2007; Yang et al. 2010). Water attenuation is calibrated in CT numbers to be zero, while water has a mass density of 1g/cc. CT numbers greater than zero theoretically have mass densities greater than 1g/cc. CT numbers less than zero theoretically have mass densities less than 1g/cc. When soft plaques are imaged with single energy CT, their CT numbers are often elevated to about 60HU even though soft plaque mass density is lower than 1g/cc (Sun et al. 2008; Hausleiter et al. 2006). The difficulty for quantifying lipid content in soft plaques is then two

fold. Beam hardening artifacts from polychromatic x-rays may elevate soft plaque's perceived mass density. Also, fibrous tissue and lipid tissue are closely attenuating such that their CT number distributions overlap. To properly identify coronary soft plaques and lipid content regardless of beam hardening iodine, dual energy acquired virtual monochromatic images and material basis pair images were investigated (Chapter 6).

CHAPTER 3 AIM 1: AN ANTHROPOMORPHIC BEATING HEART PHANTOM FOR CARDIAC X-RAY CT IMAGING EVALUATION

The anthropomorphic beating heart phantom was engineered as a tool for assessing technological advances in coronary computed tomography angiography (CCTA). The phantom mimics the challenges found in patient coronary CTA imaging such as variable heart rate, iodine injectable chambers/vessels, stents, and soft plaques (Aim 1). Imaging the phantom has provided controlled comparisons between retrospective and prospective gating techniques as well as comparisons between image types used for soft plaque classification (Aim 4).

3.1 Introduction

Successful coronary CTA requires accurate visualization and measurement of the coronary features, including coronary diameter and coronary plaques (Gerber, Kantor, and Williamson 2007). The iodine contrast material that is injected for the CTA helps to visualize the blood within the coronary arteries. Evaluation of coronary artery patency depends on the visualization of the blood-iodine mixture as well as diameter measurements taken to determine percent stenosis. For some arteries, stenosis is due to highly attenuating calcium plaque which may cause the calcium blooming artifact (Choi et al. 2004). For other arteries, stenosis is due to low attenuating soft plaque that may either be risky lipid or stable fibrous plaque, which differ in plaque density (Pavlicek et al. 2008). In order to optimize blood-iodine visualization and plaque quantification for coronary CTA exams, the beating heart phantom was engineered with a thorax, a compressor system, an ECG system, a beating heart with tortuous coronary arteries, and the option to add or remove pathologies such as aberrant beats, stents, and plaques (Nissen 2008; Ropers et al. 2003).

The successful acquisition of coronary CTA images requires proper gating of the patient ECG signal to the x-ray irradiation, precise timing of the iodine contrast injection, and image

acquisition fast enough to image the heart during the 100msec of rest in end diastole (Gerber, Kantor, and Williamson 2007; Budoff et al. 2005; Greuter et al. 2005). The challenges of successful CTA acquisition were incorporated into the heart phantom to facilitate meaningful comparisons between traditional CTA methods and newly proposed CTA methods with technologies like dual energy CTA. The completed beating heart phantom reproduces variable patient complexities, including: body habitus, heart rate, heart rate irregularities, coronary plaque, and coronary stents (Boltz et al. 2010; Mayo and Leipsic 2009; Pack et al. 2009).

3.2 Research Design and Methods

3.2.1 Average Patient Specifications for the Beating Heart Phantom

The physical attributes of the beating heart phantom were based upon a review of X-ray CT examinations of 200 patients having received a CCTA using either a Siemens Somatom Sensation 64 CT scanner or a General Electric LightSpeed VCT 64 CT scanner. To assess thorax characteristics surrounding the heart, measurements were taken of the lateral width and the anterior to posterior length. The Hounsfield unit (HU) values within the lungs, soft tissue, and bone were measured and recorded. To assess heart chamber characteristics, measurements included the longest distance from valve to apex, anterior to posterior, and left to right dimensions within the heart. The myocardium was then measured for HU values, as was the blood within the ventricles and the mixture of blood and iodine contrast material present following intravenous iodine injection. Inner diameters of the coronary arteries were also measured using CT images. The left anterior descending (LAD), left circumflex (LCX), and the right coronary artery (RCA) were all measured at the proximal, medial, and distal segments. The resulting beating heart phantom includes multiple components fabricated to match the average patient values. The components of the beating heart phantom are shown in Figure 3.1 within a CT scanner.

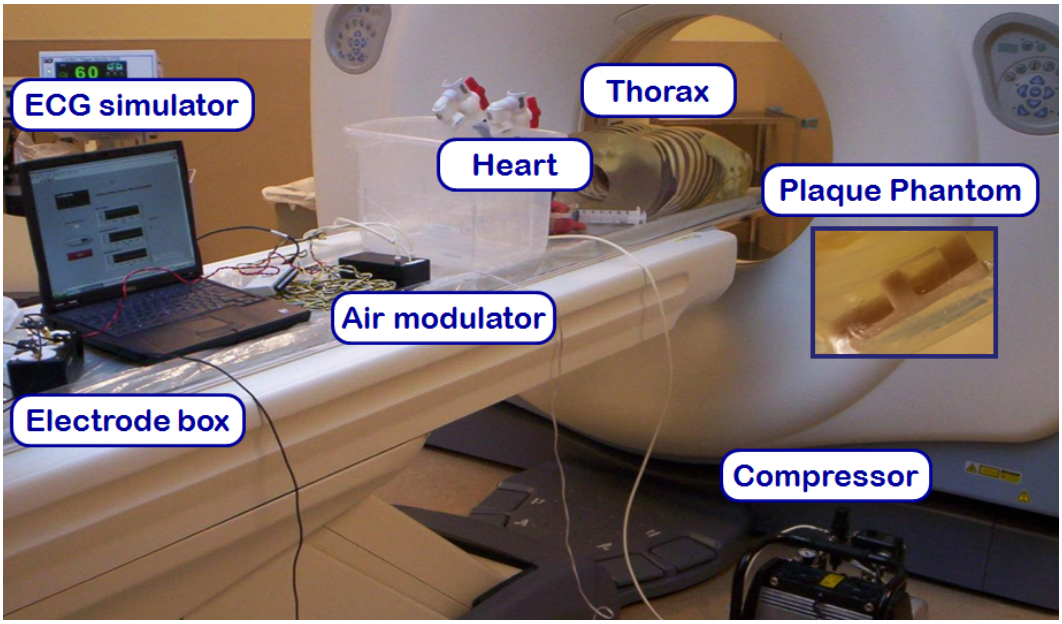

Figure 3.1: The assembled beating heart phantom within a CT scanner.

The thorax for housing the beating heart is in the far right of Figure 3.1, near the gantry, and the heart is to the left of the thorax with tubes connected for fluid and air exchange. Below the heart and outside of Figure 3.1 is the air compressor. The air modulator is the first black box to the left of the heart. LabVIEW is displayed on the laptop and the ECG electrode connection is the black box on the left of the laptop. The ECG monitor is seen in the background with a 60bpm (beats per minute) ECG waveform that the phantom is simulating.

3.2.2 The Beating Heart Phantom's Thorax

The thorax phantom is intended to house the beating heart and to produce scatter as exhibited in actual patients. The phantom's thorax is fabricated with ribs, sternum, spine, soft tissue, and lung mimicking materials with densities and HU values matching human bone, soft tissue, and lung tissues. A cavity for heart placement was constructed in the thorax, allowing the phantom heart position to match the heart position seen in the patient population. CT scanners that modulate the current (mA) exposure simultaneously with the X-ray triggering may suffer from

higher noise when imaging occurs through the lateral direction of the thorax, which is created in the phantom. An air compressor system causes the heart to beat within the thorax. The compressor is connected to the heart with lengths of plastic tubing so that it can be located in the scan room or at the operator console.

3.2.3 The Beating Heart Phantom's Compressor System

The compressor system has four parts: the compressor, the air modulator, the tubing throughout the ventricular walls of the heart, and the LabVIEW signals (National-Instruments 2005). Pneumatic tubing connects the air compressor, the air modulator, and ventricular wall tubing in series. Signals from LabVIEW to the air modulator tell the air modulator when to initiate inflow and outflow of air through the ventricular tubing. The atria and ventricle chambers are separate compartments from the pneumatic tubing that runs throughout the ventricular walls of the heart. The separate chamber and tubing compartments allow iodine contrast medium to fill the chambers themselves while air moves in and out of the ventricular walls. Outflow of air from the ventricular tubing constricts the ventricular walls and causes the heart to contract. Inflow of air through the ventricular tubing expands the ventricular walls and causes the heart to relax. In a sequential pattern, the increase and decrease of air pressure within the ventricular tubing causes contraction and relaxation of the heart's ventricles.

3.2.4 The Beating Heart Phantom's ECG System

Simulating a CCTA exam requires an ECG trace for both gating the X-ray exposure on the scanner (i.e. mimicking the electrical activity of the patient) and causing the proper cardiac motion in the beating heart. An imaging protocol that needs to trigger a momentary exposure during minimal heart motion attempts to time the X-ray exposure during the TP interval. The phantom's ECG trace allows for gating and represents true phantom motion during the QT

interval and phantom quiescence during the TP interval. Figure 3.2 outlines the phases of the human ECG signal as described.

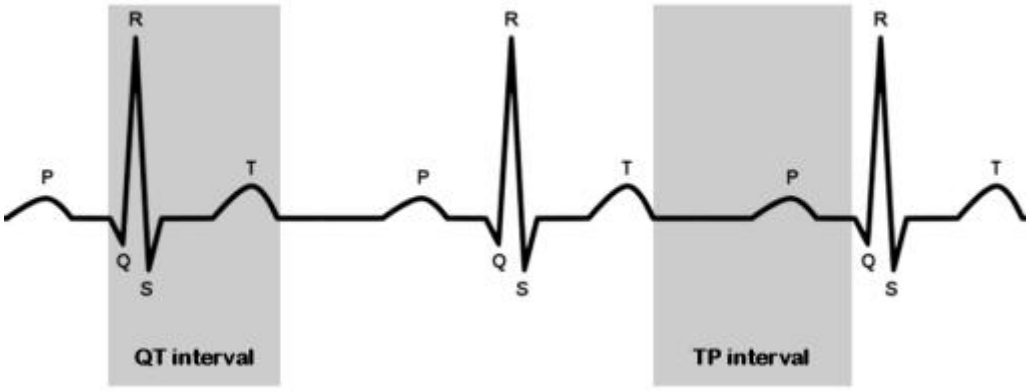

Figure 3.2: The human ECG signal used in cardiac CT scanning. The beating heart phantom has an ECG signal that matches the human ECG signal with a QT interval and a TP interval.

Ventricular systole occurs during the QT interval of electrical activity. The left and right ventricles of the heart contract during this time. It is a period of high movement and visualization of the coronary arteries is more difficult than during ventricular diastole. During the TP interval, the heart relaxes while it fills with circulating blood. Phases within 70% to 80% of the R-to-R interval occur during the TP interval when minimum coronary motion is expected.

LabVIEW, a software program capable of communicating with multiple hardware devices, is utilized to meet the several demands upon the phantom's ECG trace. The compressor's trigger signal and the scanner's gating signal both originate from LabVIEW and synchronize phantom motion to the QT interval registered on the scanner. Initial scanning with the LabVIEW program revealed that the phantom's ECG trace registered a QT interval on the scanner one half second before the compressor signal could initiate the associated movement in the heart. The ECG signal was modified to permit a timing offset in increments of one hundredth of a second to facilitate matching.

3.2.5 The Beating Heart Phantom

The phantom's heart chambers and coronaries can be sealed for use with iodine contrast medium. The beating ventricles force fluid in and out of the atria and induce movement similar to atrial diastolic filling and systolic ejection. The left atrium and left ventricle allow fluid to flow from one chamber to the other. The right atrium and right ventricle allow fluid to flow from one to the other and into the aorta and coronary arteries. When the ventricles contract, fluid pushes out of the ventricles and into the atria and coronary arteries. Ventricular contraction and relaxation displace the coronaries by about one diameter, which is the distance measured on actual patients. Once placed within the thorax, the contrast-filled beating heart phantom exhibits motion similar to that of a patient heart (Shelley-Medical-Imaging-Technologies 2006).

3.2.6 The Beating Heart Phantom's Pathology

Initial phantom trials involved the assessment of temporal resolution. Qualitative analysis of the phantom's motion artifacts provided insight into the temporal resolution achieved on a given CT scanner. Visual image comparisons were made between scans when the phantom was physically not beating and scans when the phantom was beating but imaged within the TP interval. Motion artifacts would be identified when viewing the two image sets. Ideally, little to no difference would be identified for images acquired of a stationary phantom (O'Brien et al. 2007).

In order to evaluate a scanner's ability to perform multiple phase reconstructions (using more than one cardiac cycle to capture all the projections needed to form one image of one slice of anatomy of the heart), aberrant beats can be simulated in the ECG signal. In normal ECG signal production, the electrode box generates a changing voltage per second in the form of a sawtooth wave. The peaks in the sawtooth wave trigger a QT interval in the ECG monitor, achieving a steady ECG signal. To generate aberrant beats, a second wave was added to the ECG signal that changes voltage more slowly over time, resulting in an irregular peak every 7

seconds. These beats create motion and irregular ECG data during a phase of data collection, providing a means for postprocessing evaluation.

Coronary plaques were designed in a 3D CAD environment called SolidWorks and custom machined to fit within the coronary arteries of the heart phantom (Dassault-Systemes-SolidWorks 2008). Low lipid tissue density plaques, Mid lipid density plaques, and fibrous plaques were designed for the phantom's LAD, LCX, and RCA vessels. Each plaque matches the inner diameter of a specific coronary and creates a specific blockage to the artery. The known diameters of the plaques can be compared to diameters measured on CT images. Spatial resolution assessment can then be performed on diameter comparisons that involve 0.4 mm and lower diameters. After developing a deployment method for the plaques, the method was also used for placing and removing stents into the coronary arteries, which allowed for a range of stents to be imaged using the beating heart phantom. Direct comparisons of image quality between CCTA and conventional X-ray cardiac catheterization are also possible. This is important for evaluation of stent damage or possible re-stenosis (Halpern et al. 2009; Maintz et al. 2009).

3.2.7 CT Imaging with the Beating Heart Phantom

Initial use of the phantom involved the five cardiac CT protocols listed in Table 3.1. The HU specifications of the phantom were measured with Retrospective Protocol 1. Gating capabilities were validated for the three CT scanners reported in Retrospective Protocols 1, 2, and 3. Aberrant beat and temporal resolution studies were performed with Retrospective Protocol 3. Retrospective versus prospective gating was evaluated with Retrospective Protocol 1 and Prospective Protocol. A high-resolution technique was evaluated with the High Resolution Protocol for increased spatial resolution.

Table 3.1: Beating heart phantom testing scan protocols.

Parameters	*Retrospective 1*	*Retrospective 2*	*Retrospective 3*	*Prospective*	*High Resolution*
Manufacturer	GE	GE	Siemens	GE	GE
Model	LightSpeed VCT 64	Discover HD CT750 64	Somatom Sensation 64	LightSpeed VCT 64	Discovery HD CT750 64
Scan Name	Snapshot Segment	Snapshot Segment	ThorCardioECG 033s	Snapshot Pulse	Snapshot Pulse High Res
Acquisition	Helical	Helical	Helical	Axial	Axial
Data Channels	64 by 0.625 mm	64 by 0.625 mm	32 by 0.6 mm	64 by 0.625 mm	64 by 0.625 mm
Pitch	0.22	0.22	0.3	n/a	n/a
Rotation	0.35 sec	0.35 sec	0.33 sec	0.35 sec	0.35 sec
Exposure/Rotation	0.35 sec	0.35 sec	0.33 sec	0.23 sec	0.23 sec
Voltage	120 kVp	120 kVp	120 kVp	120 kVp	120 kVp
z-Sampling	routine	routine	double	routine	routine
x,y-Sampling	routine	routine	double	routine	double
Current	750 mA	750 mA	720 mA	750 mA	750 mA
Current Modulation	OFF	OFF	OFF	OFF	OFF
Padding	n/a	n/a	n/a	0 sec	0 sec
Scan FOV	50 cm	50 cm	50 cm	50 cm	50 cm
Recon FOV	25 cm	25 cm	25 cm	25 cm	25 cm
Recon Filter	Standard	Standard	B20f	Standard	HD Standard
Recon Slick Thick	0.625 mm	0.625 mm	0.75 mm	0.625 mm	0.625 mm
Recon Increment	0.625 mm	0.625 mm	0.7 mm	0.625 mm	0.625 mm
Recon ECG Phase[(a)]	75%	75%	65%	75%	75%
CTDI Vol.	52 mGy	52 mGy	43 mGy	8 mGy	8 mGy
Effective Dose	21 mSv	21 mSv	17.4 mSv	2.4 mSv	2.4 mSv

[(a)]The 65% phase on Siemens is equivalent to the 75% phase on GE because the 65% is measured from the top of the peak in the QT interval and the 75% is measured from the start of the peak in the QT interval. Both phases represent the TP interval of quiescence in the ECG.

3.3 Results and Discussion

3.3.1 Beating Heart Phantom Specifications

The functional beating heart phantom can be seen in Figure 3.3. It is complete with soft silicone chambers, soft silicone coronary arteries, and tissue densities that cause X-ray scatter similar to an average patient (Alderson-Phantoms 2006).

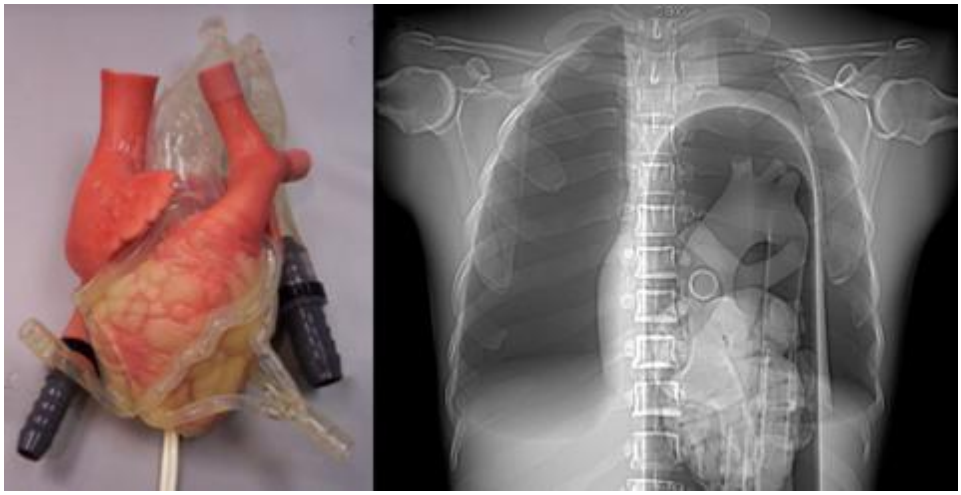

Figure 3.3: The beating heart phantom. Anterior view of the heart phantom (left). AP radiographic image of the heart phantom (right) within the thorax, showing the scatter environment that houses the heart.

Ports for accessing the heart chambers through the inferior vena cava and the aorta are shown, as well as ports for filling the coronaries through their most distal portion. These arteries may appear large, but the inner diameters match those of an average patient. Phantom specifications were measured with the Retrospective Protocol 1 acquisition and compared with the CCTA patient population. Patient averages and the phantom specifications can be seen in Table 3.2.

Table 3.2: Average patient measurements compared with heart phantom specifications.

Parameter	*Average Patient*	*Phantom*
Thorax anterior posterior	211 mm±25	209 mm
Thorax left to right	285 mm±29	302 mm
Thorax soft tissue	44 HU±18	25 HU
Thorax bone tissue	708 HU±115	751 HU
Thorax lung tissue	-778 HU±57	-684 HU
LV Aortic valve to apex[(a)]	133 mm±15	77 mm
LV anterior posterior	110 mm±16	67 mm
LV left to right	112 mm±11	93 mm
LV myocardium	115 HU±24	150 HU
LV blood	41 HU±5	20 HU
LV blood and Iodine	34 2HU±89	30 HU–1,000 HU
LAD proximal	4 mm±0.5	3.7 mm
LAD medial	3.5 mm±0.3	3.0 mm
LAD distal	1.8 mm±0.2	2.1 mm
LCX proximal	3.0 mm±0.6	3.2 mm
LCX medial	2.0 mm±0.4	2.4 mm
LCX distal	1.5 mm±0.4	1.8 mm
RCA proximal	4.0 mm±0.6	3.9 mm
RCA medial	3.5 mm±0.4	3.4 mm
RCA distal	2.0 mm±0.2	1.7 mm
Heart Rate	55–75 bpm[(b)]	40–85 bpm

[(a)]LV = Left Ventricle. [(b)]bpm = beats per minute.

Hounsfield unit measurements for the patient population and the phantom specifications were taken from images acquired using 120kVp. The HU values for saline simulating blood in the phantom were measured within the chambers. Phantom densities are generally higher than the reported average patient densities, but the contrast ratio between the vessels and the iodine contrast can be duplicated to make image quality evaluations applicable (Mah, Samei, and Peck

2001). The measurements for the left ventricle are provided as an example of the measurements performed for all chambers.

3.3.2 The Beating Heart Phantom's ECG Gating

After achieving accurate propagation of the ECG and compressor signals, typical patient heart rates were tested with routine scanning protocols. Comparison of beating and not beating phantom scan reconstructions were made to determine the level of cardiac motion artifact relative to motion artifact found in patients. Figure 3.4 shows a comparison of a patient's RCA movement with that of the phantom's RCA movement while beating, using the Retrospective Protocol 3. No appearance of motion was observed for Retrospective Protocols 1, 2, and 3 from Table 3.1. For heart rates ranging from 40bpm to 85bpm, motion artifact is not present in images acquired during the TP interval of the ECG.

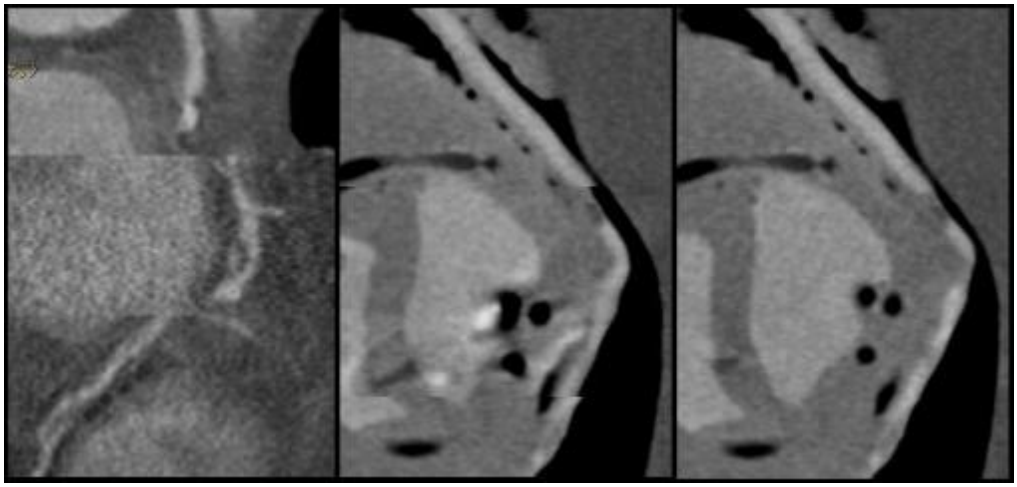

Figure 3.4: Phase mismatch comparison between patient and phantom data. Patient RCA (left) reconstructed with 3 phases: TP interval on the top, QT interval in the middle, and TP interval at the bottom. The phantom RCA (middle) reconstructed with 3 phases: TP interval on the top, QT interval in the middle, and TP interval at the bottom. The phantom RCA (right) reconstructed with only the QT interval in the top, middle, and bottom.

The completion of the ECG gating validation was followed by a study between retrospective versus prospective gating. Retrospective techniques, using pitch less than 0.3,

continuously collect data from several heart beats during all heart cycle phases. This technique ensures complete coverage of the heart and allows for correction of motion artifacts caused by non-steady cardiac rhythms. Prospective techniques only irradiate during the predicted TP interval, implying cardiac quiescence. This step-and-shoot mode reduces dose, but limits the ability to correct motion artifacts due to the smaller number of cardiac phases acquired. Once the beating heart phantom was scanned with the Retrospective Protocol 1 and Prospective Protocol from Table 3.1, it was evident that sufficient image quality could be maintained with either technique. It was also confirmed that the retrospective technique delivered 21 mSv effective dose, while the prospective technique delivered only 2.4 mSv effective dose (Hausleiter et al. 2009). The phantom study supported that prospective gating could be prescribed for patients with heart rates up to 75bpm, providing that the heart rate is steady (because the phantom's heart rate was steady during testing).

3.3.3 The Beating Heart Phantom's Pathology

Scanning the phantom with the aberrant beat signals simulates motion artifacts that the scanner and postprocessing should be able to eliminate given multiple phases. The phantom images with motion artifact in a phase reconstruction can be postprocessed to evaluate beat rejection software from a vendor. Alternatively, the beat rejection software can be evaluated during acquisition.

Removable coronary plaques provide a test plaque HU in the presence of iodine contrast enhancement and a test of percent stenosis measurements. The plaques themselves can be scanned free in air, immersed in saline, or immersed in contrast medium. The effects of increased contrast on perceived plaque HU can then be assessed as a function of scatter environment and/or kVp (Horiguchi et al. 2007). Such assessments would identify the protocol that properly visualizes the known size and shape of the plaque. Plaque phantom stenoses of 40%, 60%, and 80% were fabricated for each coronary segment and each density type. Further plaque

assessment would include evaluating the accuracy of stenoses within the image data as compared to known stenoses. Figure 3.5 depicts the presence of plaque phantoms and stents within the beating heart phantom.

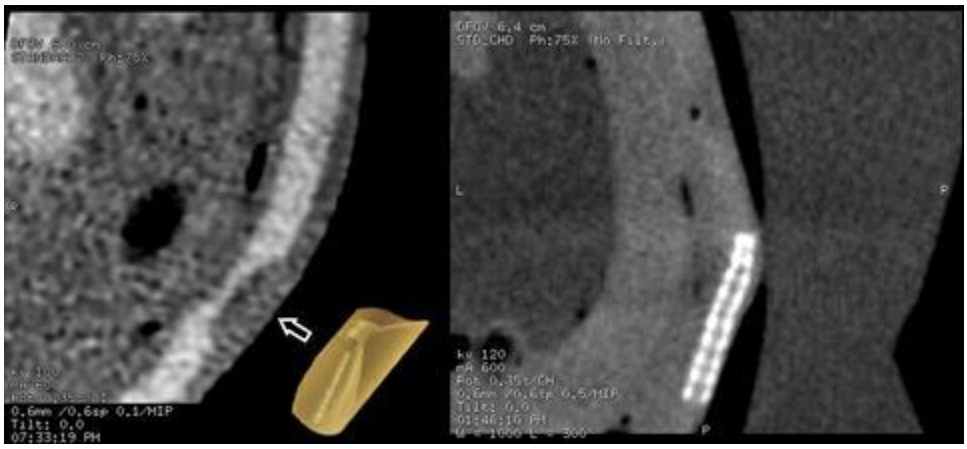

Figure 3.5: Phantom plaques and stents. A curved center-seeking multiplanar reformat (CSCMPR) (left) of the phantom's LCX and a picture of a machined fibrous plaque, with arrow denoting the location of the machined fibrous plaque within the scanned artery. CSCMPR of the phantom's RCA (right) from a high-resolution scan with a stent in the lower region of the artery.

In the left image of Figure 3.5, an arrow indicates the presence of a fibrous tissue density plaque insert in the LCX. This fibrous plaque has been machined to create a 60% blockage in the medial portion of the LCX. Image based measurements of the blockage estimate the blockage to be 68% (Pavlicek et al. 2008). As for the stent in the right image of Figure 3.5, the phantom results show that a stent can be visualized with the High Resolution Protocol from Table 3.1 while beating 63bpm. The High Resolution Protocol seen in Figure 3.5 utilized a double sampling in the x–y plane and delivered 2.4mSv effective dose, which is the same dose that a routine prospective exam would deliver. When blooming is present, the detected signal is so strong that the stent appears to be bright around its entire perimeter and limits visualization of possible tissue between stent struts. The phantom provides a means of evaluating how well a CT scanner can visualize re-stenosis and reduce blooming.

3.4 Conclusions

A beating heart phantom was constructed that strategically recreates an average patient's cardiac CT exam in terms of scatter, cardiac tissue densities, coronary size, motion, heart rate, and contrast material. Representative pathology can be simulated such as anomalous ECG activity, and stents and plaques located in the proximal, medial, and distal segments of the coronary tree. The phantom offers the ability to isolate X-ray CT acquisition parameters and provides a means of optimizing imaging strategies including: radiation dose, temporal resolution, spatial resolution, iodine image contrast, image reconstruction parameters, and accuracy of stenosis and plaque composition.

3.5 Clinical Significance

The completed beating heart phantom has been used to achieve several clinical goals: establishing the appropriateness of low dose prospective CCTA imaging, testing radiation exposure timing for dual energy CCTA imaging, and assessing soft plaque characteristics. The first CCTA technology commercially available relied on retrospective gating to acquire the angiographic images. Retrospective gating utilized 24mSv effective dose to image all phases of the cardiac cycle and reconstructed a single set of images during least motion of the heart for diagnostic evaluation. When prospective gating technology was released that captured a single phase of the cardiac cycle, it was unclear which patients qualified to receive the lower effective dose exam offered by the technology. Mayo Clinic Arizona used the beating heart phantom to exhaustively compare retrospective and prospective gating imaging across heart rates from 50bpm to 80bpm. It was then determined that patients with a steady heart rate of up to 75bpm were eligible to receive the 2.4mSv effective dose with prospective gating while maintaining the image quality achieved with retrospective gating at 24mSv effective dose (Boltz et al. 2010). For defining this distinction, the work on the beating heart phantom received the 2010 "UNFORS AWARD OF EXCELLENCE FOR THE BEST RADIATION MEASUREMENTS ARTICLE".

General Electric Healthcare initially released their fast switched dual energy CT scanner without the capability to scan hearts with dual energy. The dual energy technology was quickly applied to tissue characterization and quantification problems pertaining to pancreas uptake, uric acid build up, and liver fat. Once the need emerged to quantify tissues in the heart, General Electric Healthcare used the beating heart phantom to test the application of dual energy with retrospective and prospective gating technologies (Pack et al. 2009). The result was a scanner and software package that allowed for prospective CCTA imaging of the heart with dual energy. In helping to develop dual energy CCTA technology, the beating heart phantom also helped make it possible for future implementation of Aim 2, Aim 3, and Aim 4 of this dissertation.

While the dual energy CCTA technology was being developed, the beating heart phantom and its engineered soft plaques were used to develop soft plaque classification systems. The plaques from the beating heart phantom were scanned with dual energy technology and images were made with and without the presence of iodine. With these images, a training data set was established that could be used for classification systems like support vector machines (SVM). Being that the phantom plaques were stable fibrous plaque and risky lipid plaque, the SVM system was theoretically set up to distinguish between stable and risky plaques in the coronary arteries. Once classified as fibrous or lipid, soft plaque deposits could be scored to produce a lipid mass burden. Accurate lipid mass values would give physicians a new metric for tracking the correlation between coronary lipid mass burden and coronary events.

CHAPTER 4 AIM 2: CORONARY CALCIUM PLAQUE QUANTIFICATION WITH DUAL ENERGY CT ANGIOGRAPHY

Dual energy image types have been used to quantify several tissues and materials found in the body, ranging from gout in joints to iodine in the liver (Glazebrook et al. 2011; Santamaria-Pang et al. 2010). Cardiac scanning may also benefit from the ability to quantify tissues and materials, but one dual energy scan has equal radiation dose to that of two single energy scans. My proposed method obtains an Agatston score from one iodinated dual energy scan with ±11% error (Bland-Altman Error), eliminating the need for a non-iodinated scan. If my proposed method is used, patients may reap the benefits of quantifying iodine and lipid content without increased radiation dose.

4.1 Introduction

Coronary calcium scoring with CT is a non-invasive method for quantifying the extent of atherosclerotic disease in the coronary arteries (Agatston et al. 1990; Schmermund, Mohlenkamp, and Erbel 2003; Greenland et al. 2007). A coronary calcium score of zero has a high predictive value for minimal risk of death from coronary artery disease (CAD) when considered in addition to cardiovascular risk factors, such as the Framingham study risk factors (Halliburton, Stillman, and White 2002; Sarwar et al. 2009). Single energy cardiac CT imaging requires the acquisition of both a non-enhanced scan for coronary artery calcium scoring (CACS) and an iodinated scan for coronary computed tomography angiography (CCTA) (O'Brien et al. 2007). The proposed dual energy cardiac CT imaging requires only a single iodinated CT scan to provide image sets for both CACS and CCTA (Pavlicek et al. 2010). Unlike the polychromatic images derived from single energy CT, dual energy CT provides virtual monochromatic images and material basis pair images. My work aimed to determine the best dual energy image type for obtaining a calcium score from an iodinated exam. Comparisons were made between calcium

scores from conventional non-iodinated single energy images and calcium scores from iodinated dual energy images.

Successful calcium scoring from one iodinated dual energy CT scan would keep the radiation dose from the total dual energy cardiac CT imaging equivalent to single energy cardiac CT imaging (Gerber et al. 2009). The benefits of dual energy cardiac CT imaging over single energy cardiac CT imaging are the added applications enabled by dual energy image types (Zachrisson et al. 2010; Leschka et al. 2008). Only dual energy CT scanning is able to produce virtual monochromatic images and material basis images (Gerber, Kantor, and Williamson 2007). Virtual monochromatic images have several corrections for beam hardening that should make them useful for areas where single energy images suffer from beam hardening (Xu et al. 2009; Groen et al. 2008). Material basis pair images have the ability to separate two materials within an image data set. Cardiac CT imaging would benefit from material basis separation of calcium and iodine in the coronary arteries for correcting the calcium blooming artifact (Nakanishi at al 2005). Cardiac CT imaging would also benefit from material basis separation of lipid and fibrous tissue in the coronary arteries for quantifying the lipid burden (Kristensen et al. 2010). In order to benefit from the added applications that dual energy imaging provides and keep the radiation dose equivalent to single energy cardiac CT imaging, my study has investigated the elimination of a separate non- iodinated CT scan for coronary calcium scoring.

4.2 Research Design and Methods

4.2.1 Calcium Scores from Single Energy CT

Both the Agatston score and the calcium mass score are used to quantify the atherosclerotic disease present in the coronary arteries (Agatston et al. 1990; Hong et al. 2004; Rumberger et al. 1995). The Agatston score for single energy CT is the summation of the weighted calcium burden from each calcium plaque in the coronary tree. Often times, the

Agatston score is reported for all coronary arteries to establish a disease percentile ranking while also reporting the score separately for the left anterior descending coronary artery (LAD), the left circumflex coronary artery (LCX), and the right coronary artery (RCA) (Halliburton, Stillman, and White 2002). Once a non-iodinated scan of the coronary arteries is obtained, each axial image is evaluated for calcium plaques. Any pixels above the threshold of 130HU (at 120kVp) and within the coronary arteries are considered to be calcium and are counted toward the overall Agatston score. The summated score from all calcium plaques is denoted by equation 4.1:

$$AS = \sum^{N} w \cdot A \tag{4.1}$$

where *AS* is the total Agatston score, *w* is the weighting factor, *A* is the area of the calcium plaque for a given image, and *N* is the total number of calcium plaques in the entire coronary artery tree. The weighting factor is determined by the maximum pixel value (CT_{MAX}) found within the area (*A*) of a single calcium plaque. Agatston et al. established the weighting factors as follows:

w = 0, if CT_{MAX} < 130HU,

w = 1, if 130HU ≤ CT_{MAX} < 200HU,

w = 2, if 200HU ≤ CT_{MAX} < 300HU,

w = 3, if 300HU ≤ CT_{MAX} < 400HU,

w = 4, if CT_{MAX} ≥ 400HU.

Figure 4.1 gives an example of how the Agatston score evaluates calcium plaques in a single image, grouping together pixels greater than 130HU. Each group of pixels can then be evaluated to find the CT_{MAX} in the group and the area of the group for summation into the total Agatston score.

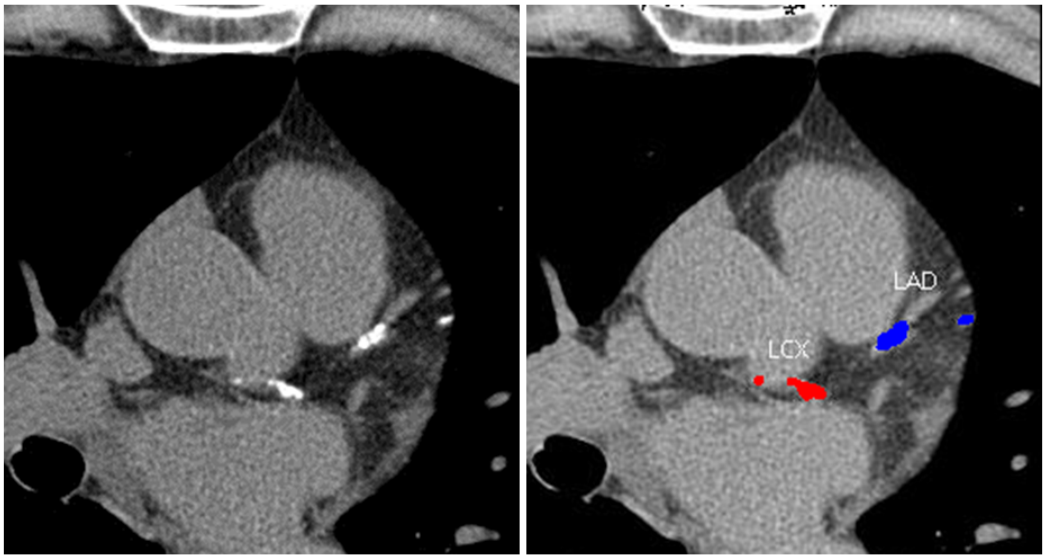

Figure 4.1: Non-iodinated data for calcium scoring. The left image is the first image in the axial data set with pixels above 130HU (seen as the bright white pixels). The right image shows how the Agatston score considers there to be 2 calcium plaques in the LCX and 2 calcium plaques in the LAD.

The calcium mass score for single energy CT is determined using a calcium calibration factor (density/HU) and the unknown HU values from suspect patient calcium plaques (Halliburton, Stillman, and White 2002). The calibration factor (c_{HA}) is calculated using a known density of calcium hydroxyapatite and the HU values that correspond to the known density. The calibration factor is described using the equation 4.2:

$$(4.2) \quad c_{HA} = \frac{\rho_{HA}}{CT_{HA} - CT_{water}}$$

where c_{HA} is the calibration factor, ρ_{HA} is the mass density of the known calcium hydroxyapatite sample, CT_{HA} is the mean HU value of the calcium hydroxyapatite, and CT_{water} is the mean HU value of water. After computing the c_{HA}, the total calcium mass score can be calculated for the entire coronary tree using calcium mass scores from each calcium plaque as shown in equation 4.3:

$$(4.3) \quad CS = \sum^{N} c_{HA} \cdot V_{plaque} \cdot CT_{plaque}$$

where CS is the total calcium score, N is the total number of calcium plaques in the coronary artery tree, c_{HA} is the calibration factor, V_{plaque} is the volume of the suspect calcium plaque, and CT_{plaque} is the mean HU value of the suspect calcium plaque. With single energy CT, a separate non-iodinated scan must be obtained for performing Agatston and calcium mass scoring because calcium and iodine both produce pixels above the 130HU threshold used in calcium scoring (Muhlenbruch et al. 2005). The proposed dual energy CT calcium scoring could be performed using the iodinated dual energy CTA scan alone.

4.2.2 Proposed Calcium Scores from Dual Energy CT

In order to develop an Agatston score and a calcium mass score for dual energy iodinated exams, comparisons had to be made between the scores from non-iodinated single energy scans and iodinated dual energy scans. The single energy scans in conventional scanning produce polychromatic images at 120kVp. The proposed dual energy scan has images for comparison with 70keV images and Calcium(Iodine) images. The images for comparison are shown in Figure 4.2. The first image (A) in Figure 4.2 shows a bright region in the LAD that is coronary calcium plaque. Once the iodine is administered, the whole image is bright in the middle image (B), but the Calcium(Iodine) image is able to separate out the iodine and leave the single bright region (C).

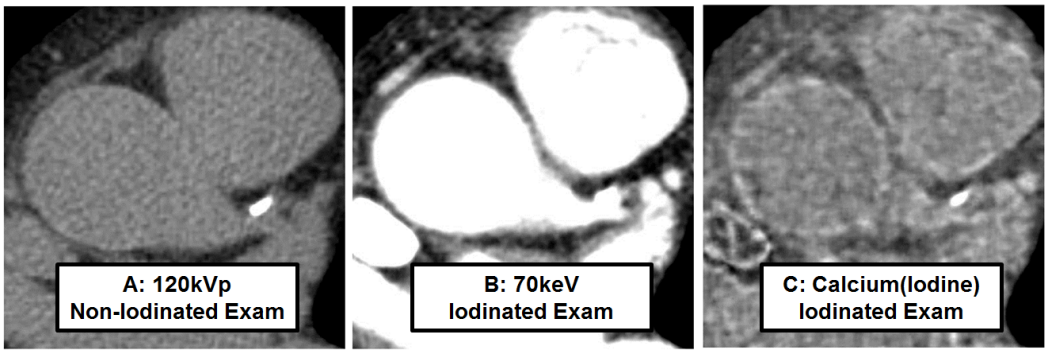

Figure 4.2: Data sets for iodinated and non-iodinated calcium scoring. The same LAD is seen branching off of the aorta in 3 different image types. Single energy cardiac imaging produced a non-iodinated image set at 120kVp (A). The proposed dual energy CT produced an iodinated image set at 70keV (B) and a Calcium(Iodine) image set (C).

The 70keV images have effectively the same HU distributions as 120kVp images, but 70keV images have corrections for beam hardening that theoretically makes them more accurate at representing true attenuation values. The Calcium(Iodine) images are images made by assuming that each pixel represents attenuation due to only calcium or iodine. Using the convention “Calcium(Iodine)” means that the calcium attenuation values are represented in the pixel values while “Iodine(Calcium)” means that the iodine attenuation values are represented in the pixel values. Comparisons of calcium scores are made among the non-iodinated 120kVp images, the iodinated 70keV images, and the virtual non-iodinated Calcium(Iodine) images.

4.2.3 Calibration of DECT Calcium Score Parameters

When working with non-iodinated 120kVp images, the Agatston score relies upon the threshold of 130HU to identify calcium pixels from non-calcium pixels. The Agatston score also depends upon the HU values associated with each weighting factor. In order to calculate an Agatston score for the iodinated 70keV images and virtual non-iodinated Calcium(Iodine) images, the equivalent CT values had to be correlated for the threshold and weighting factor. The correlation produced the values reported in Table 4.1.

Table 4.1: Needed dual energy CT parameters for calculating calcium scores. The value of “CT” below is the numerical value of the pixel from the associated image type. Several CT pixel values need to be determined for dual energy CT calculation of calcium scores and their corresponding single energy CT pixel values.

Calcium Score Metric	120kVp Non-Iodinated	70keV Iodinated	Calcium(Iodine) Virtual Non-Iodinated
w = 0	CT <130	CT <?	CT <?
w = 1	130≤ CT ≤200	?≤ CT ≤?	?≤ CT ≤?
w = 2	200≤ CT ≤300	?≤ CT ≤?	?≤ CT ≤?
w = 3	300≤ CT ≤400	?≤ CT ≤?	?≤ CT ≤?
w = 4	CT ≥400	CT ≥?	CT ≥?
c_{HA} (mg/cm^3)	0.838	?	?

In order to determine the missing values in Table 4.1, ex-vivo samples of femoral calcium plaques were scanned with single energy and dual energy imaging. The pixel values could then be compared among the 120kVp data set, the 70keV data set, and the Calcium(Iodine) data set. The phantom used to provide attenuation for the ex-vivo phantom scans is seen in Figure 4.3.

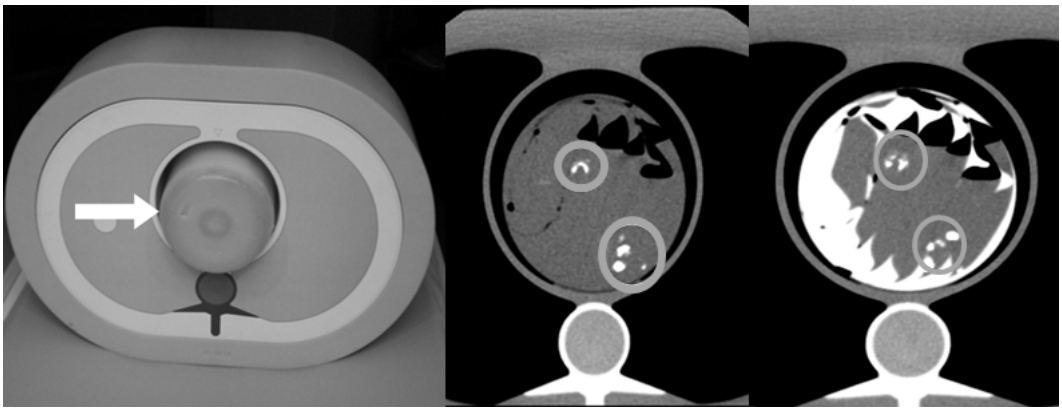

Figure 4.3: Ex-vivo samples for calcium scoring tests. The left picture shows a phantom thorax with a cylindrical container (arrow) that houses the ex-vivo calcium samples. The middle CT image has circles depicting the ex-vivo calcium samples within the container and phantom thorax and right CT image with iodine injected.

4.2.4 Phantom Validation of DECT Calcium Scores

After deriving the equivalent weighting factor thresholds and calibration factor value for 70keV and Calcium(Iodine), known amounts of calcium hydroxyapatite were scanned to determine the accuracy of measurements taken from 70keV images and Calcium(Iodine) images as previously tested for other image types (Muhlenbruch et al. 2005). Separate vials contained known calcium hydroxyapatite samples in the amounts of 15mg, 30mg, 60mg, 120mg, 180mg, and 240mg. Each vial was scanned with a non-iodinated setup and an iodinated setup as well as single energy and dual energy. Agatston scores and calcium scores were calculated for the known amounts of calcium hydroxyapatite and compared among 120kVp, 70keV, and Iodine(Calcium).

4.2.5 Patient Validation of DECT Calcium Scores

The comparison of calcium scores for the known amounts of calcium served as a means of identifying the most accurate image type for quantifying calcium from an iodinated exam. Patients were then scanned under IRB and HIPAA approval such that 6 males and 1 female received both a non-iodinated and an iodinated exam. Non-iodinated exams were prospectively triggered using 120kVp, 750mA, 0,35sec rotation, 1.0pitch, and 64x0.625mm detector configuration. Iodinated exams were fast switched dual energy acquisitions using 80kvp/140kVp, 715mA, 0.35sec rotation, and 64x0.625mm detector configuration. The result was 120kVp images used to create calcium scores from non-iodinated scans and Calcium(Iodine) images used to create calcium scores from iodinated scans.

4.3 Results and Discussion

4.3.1 Calibration of DECT Calcium Score Parameters

Ex-vivo calcium samples from patient femoral arteries were scanned to determine the conversion from 120kVp CT pixel values to 70keV CT pixel values and to Calcium(Iodine) CT pixel values (ex-vivo samples obtained under pathology IRB consent). The ex-vivo samples were placed in the phantom thorax shown in Figure 4.3 and scanned in the presence of a 4% iodine:saline mixture. Regions of interest were then taken on the calcium samples and compared among the CT values from 120kVp images, 70keV images, and Calcium(Iodine) images. Being that 70keV is the equivalent effective energy to 120kVp, the 120kVp CT values were found to be within ±5% of the 70keV CT values. However, the Calcium(Iodine) CT values had to be converted using the correlation seen in Figure 4.4.

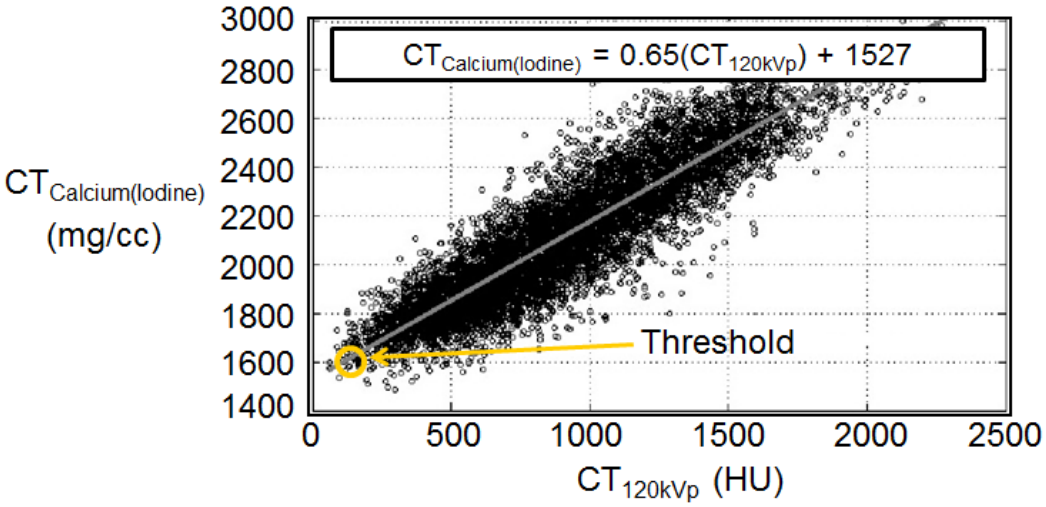

Figure 4.4: The data for mean values of ex-vivo calcium plaques in the presence of iodine. Using the correlation equation, the 130HU calcium threshold from 120kVp CT values was converted to be 1617mg/cm^3 in Calcium(Iodine) CT values.

The correlation equation presented in Figure 4.4 was determined using linear regression (R=0.85, p<0.001), and was used to convert the 130HU calcium threshold from 120kVp CT values to 1617mg/cm^3 for Calcium(Iodine) CT values. All pixels with a value of 1617mg/cm^3 and greater were considered to be calcium when calculating an Agatston score with Calcium(Iodine) images. After converting the 120kVp CT values to 70keV CT values and to Calcium(Iodine) CT values, the calibration of dual energy CT values was completed and the unknown CT values from Table 4.1 were recorded in Table 4.2.

Table 4.2. Correlated dual energy CT parameters for calculating calcium scores.

Calcium Score Metric	120kVp Non-Iodinated	70keV Iodinated	Calcium(Iodine) Virtual Non-Iodinated
w = 0	CT <130	CT <130	CT <1617
w = 1	130≤ CT ≤200	130≤ CT ≤200	1617≤ CT ≤1662
w = 2	200≤ CT ≤300	200≤ CT ≤300	1662≤ CT ≤1724
w = 3	300≤ CT ≤400	300≤ CT ≤400	1724≤ CT ≤1786
w = 4	CT ≥400	CT ≥400	CT ≥1786
c_{HA} (mg/cm^3)	0.838	0.838	0.084 for w=1 0.124 for w=2 0.167 for w=3 0.209 for w=4

All the values were correlated for the Agatston weighting factors in Table 4.2 as well as the calibration factor for 120kVp and 70keV. The weighting factors and calibration factor are equivalent between 120kVp and 70keV because the ±5% error was not greater than the standard deviations reported for the CT values from each image type. Also, leaving the values equivalent made for a direct comparison of accuracy between 120kVp and 70keV given that the effective energies are the same. The Calcium(Iodine) weighting factors were converted from the correlation equation presented in Figure 4.4. Several calcium calibration factors were determined for Calcium(Iodine) because the Calcium(Iodine) CT values do not increase linearly with increasing calcium mass density. It is assumed with 120kVp CT values that the calibration factor applies across all 120kVp CT values, but that was not found to be the case with Calcium(Iodine) CT values (Muhlenbruch et al. 2005). Phantom and patient validation testing were then performed with the converted weighting factors and calibration factors.

4.3.2 Phantom Validation of DECT Calcium Scores

A non-iodinated scan was performed on the calcium phantom vials at 120kVp, matching the non-iodinated scan that patients receive for measuring an Agatston score and a calcium mass score. Once the non-iodinated scan was completed, an iodinated scan was performed on the calcium phantom vials. Figure 4.5 shows the comparison of Agatston scores from the non-iodinated and iodinated scans for measurements from the 120kVp images, 70keV images, and Calcium(Iodine) images. The Agatston score was calculated using the weighting factors shown in Table 4.2 with the exception of the Calcium(Iodine) 1617 CT threshold, which was too low and returned elevated Agatston values compared to measurements made on 120kVp. In following the methodology utilized by Hong with iodinated single energy data, the next CT level of calcium (CT=1662) was used to set the threshold above that of iodine and to reduce the number of pixels misclassified as calcium (Hong et al. 2002).

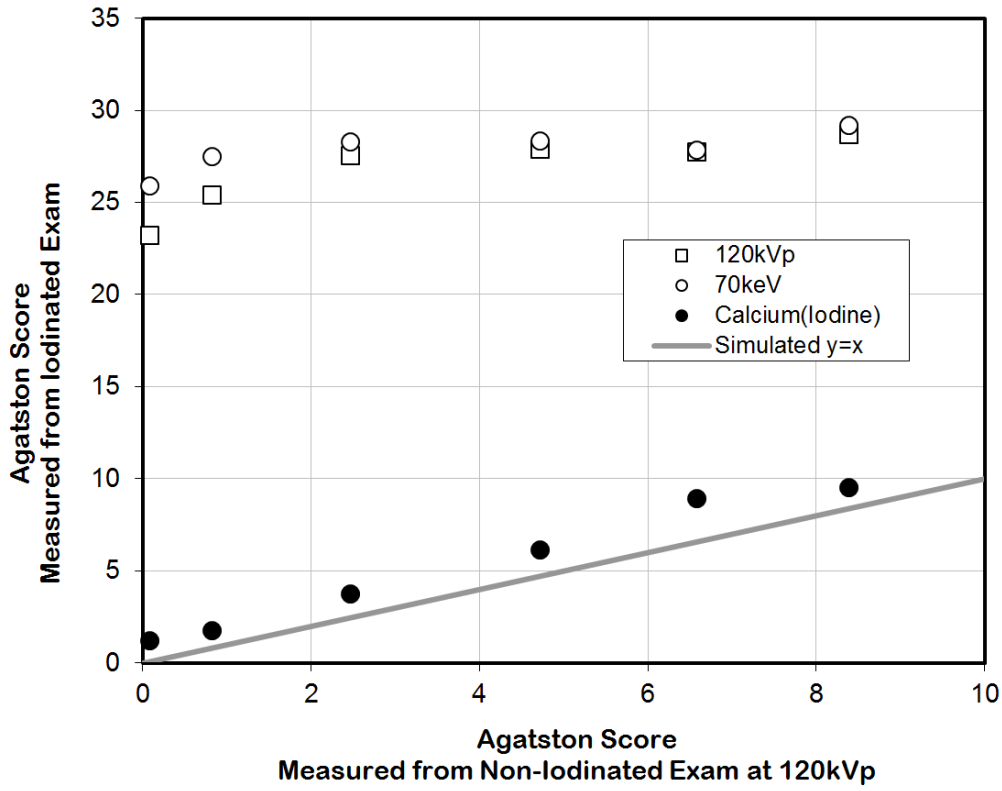

Figure 4.5: Agatston scores comparisons from measurements with 120kVp images, 70keV images, and Calcium(Iodine) images. The 6 data points for each image type represent the 6 calcium phantom vials with known amounts of calcium hydroxyapatite: 15mg, 30mg, 60mg, 120mg, 180mg, and 240mg.

The results for the 120kVp image measurements, shown in Figure 4.5, indicate that the Agatston score is elevated far above the simulated y=x line. If the 120kVp data were on the simulated y=x line, then the 120kVp image type would be providing accurate measurements for both the non-iodinated scan and the iodinated scan. Agatston scores obtained from Calcium(Iodine) images are only slightly elevated above the y=x line, which is achieved in part by utilizing the CT=1662 as the calcium threshold. Since the original threshold of CT=1617 was determined from human samples of calcium, the phantom vials required a higher calcium threshold due to a different attenuation environment and the use of calcium HAP instead of human calcium samples. The increased Agatston score for 120kVp and 70keV is due to the false classification of iodine pixels as calcium pixels in the iodinated scan. Falsely classified calcium pixels and correctly classified

iodine pixels are adding together and increasing the Agatston score well above the conventionally obtained Agatston score at 120kVp and 70keV. The Calcium(Iodine) image removes the iodine and allows for correct classification the calcium pixels when the threshold is correctly chosen, creating a more accurate Agatston score than either 120kVp or 70keV.

Accurate measurement of the Agatston score depends on correctly classifying and quantifying calcium pixels in terms of their weighting factor. The calcium mass score depends on accurately quantifying the calcium pixels in terms of their calcium mass content. The same data, used to create Figure 4.5, were used to calculate calcium mass scores using 120kVp, 70keV, and Calcium(Iodine). Figure 4.6 shows measurements from an iodinated exam compared to measurements from an analytical balance. The analytical balance provided a true measure of the calcium mass in each vial.

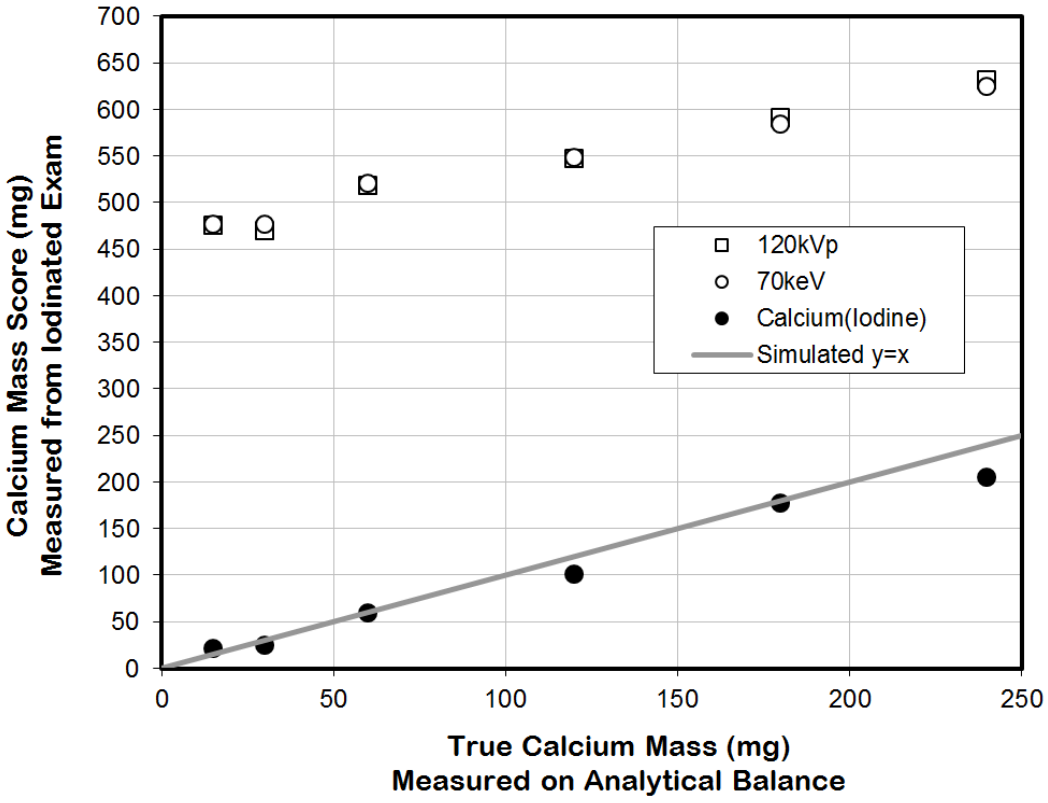

Figure 4.6: Calcium mass scores comparisons from measurements taken on 120kVp images, 70keV images, and Calcium(Iodine) images. The 6 data points for each image type represent the 6 calcium phantom vials with known amounts of calcium hydroxyapatite: 15mg, 30mg, 60mg, 120mg, 180mg, and 240mg.

Measurements from 120kVp and 70keV are again much greater than the simulated y=x line in Figure 4.6, which supports that incorrectly classified iodine pixels are adding to the calcium mass score and elevating it well above the true calcium mass (mg). Figure 4.5 and Figure 4.6 both show that Calcium(Iodine) images correctly represent calcium pixels, through successful separation of calcium and iodine, for more accurate Agatston and calcium mass scores even with iodinated exams. Clinical decisions are most commonly based on Agatston score and its associated disease percentile ranking. The last data comparison in this work involves the comparison of Agatston scores obtained with non-iodinated 120kVp imaging and iodinated Calcium(Iodine) imaging.

4.3.3 Patient Validation of DECT Calcium Scores

Under IRB consent, 5 patients were scanned with both a non-iodinated 120kVp scan and an iodinated dual energy scan (Pavlicek et al. 2009). The non-iodinated 120kVp images and the iodinated Calcium(Iodine) images were then used to calculate Agatston scores, which served as a patient comparison of the traditional and proposed Agatston scoring methods. From the IRB consented patients, 3 patients had cardiac exams and 2 patients had lung exams, providing 11 vessels for performing Agatston scoring (9 coronary arteries and 2 aortas). The calcium threshold used for calculating these Agatston scores was again elevated to set calcium attenuation above iodine attenuation. Using logistic regression techniques outlined by Yamak et al., the calcium threshold was changed to CT=1700 (Yamak et al. 2013). Figure 4.7 shows Agatston scores from all 11 vessels both from measurements on non-iodinated 120kVp images and measurements on iodinated Calcium(Iodine) images.

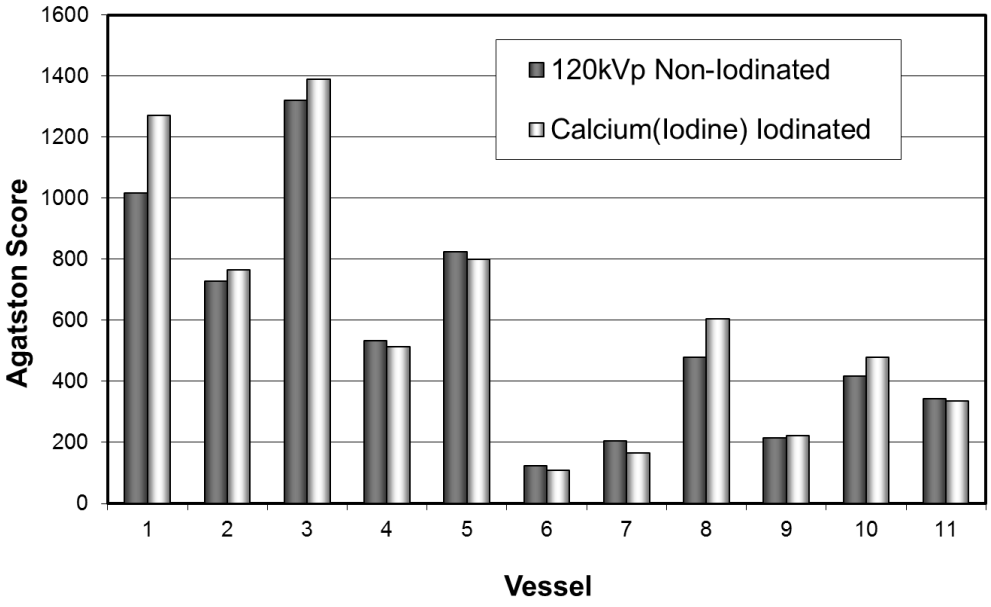

Figure 4.7: Agatston score comparisons from non-iodinated 120kVp images and iodinated Calcium(Iodine) images.

Figure 4.7 shows acceptable error (±11% from Bland-Altman analysis) between scores from the traditional non-iodinated 120kVp images and scores from my proposed iodinated Calcium(Iodine) images. Current standards for Agatston scores are ±13% error as established from scans taken on the same patients but days apart, which makes my proposed method within the range of acceptable Agatston scoring (Horiguchi et al. 2006; McCollough et al. 2007). The Agatston scores measured from Calcium(Iodine) images nearly doubled when using the calcium threshold of CT=1662. Upon increasing the threshold to 1700 as proposed by Yamak et al., the Agatston values reduced by one half and the number of pixels counted as calcium reduced by about one half as well. Pixels counted as calcium and the Agatston score are directly related because the Agatston score considers the area of each pixel for its calculation. It is then important to properly calibrate the calcium threshold for the particular scan data in question. In fact, Ferencik et al. have used calcium calibration phantoms scanned with the patient to arrive at a more accurate Agatston and volume score (Ferencik et al. 2003). My method would benefit from calcium calibration phantoms that set the calcium threshold for individual scans.

4.4 Conclusions

Although single energy CT imaging requires a separate non-iodinated scan to obtain an Agatston score, equivalent Agatston scores can be successfully obtained from iodinated dual energy scans using Calcium(Iodine) images and the correct calcium threshold. The Agatston scores obtained from iodinated dual energy scans exhibit an error of ±11% (Bland-Altman), which is equivalent to the error seen when the same patient has an Agatston score measured days apart from non-iodinated single energy scans. As long as the calcium threshold is calibrated to the patient scan, a dual energy cardiac scan can be performed on patients that produces an equivalent Agatston score and several image types not available with single energy CT.

4.5 Clinical Significance

With single energy cardiac scanning, calcium scores can be calculated and vessel patency can be qualitatively assessed. With dual energy cardiac scanning, calcium scores can be calculated, vessel patency can be qualitatively assessed, calcium blooming artifacts may be reduced, myocardial uptake of iodine may be quantifiable, and lipid versus fibrous classification may be possible (Nagao et al. 2008; Schaar et al. 2007). If dual energy images reduce the calcium blooming artifact, patients with high amounts of calcium could still get accurate stenosis measurements from dual energy cardiac scans. If dual energy images can enable iodine quantification as they have enabled calcium quantification in this chapter, then iodine uptake in the heart muscles could be accomplished without having the patient undergo a nuclear medicine stress test. Lastly, dual energy image types may allow for classification of suspect soft plaques as lipid rich or fibrous as well as quantification of the lipid content. With a method for quantifying lipid content in a patient's coronary arteries, risk scores could be developed for the likelihood of a coronary event. The dual energy Agatston scoring method validated in this chapter allows for obtaining more information about cardiac viability while maintaining the same radiation dose as single energy cardiac scanning.

CHAPTER 5 AIM 3: CORONARY CALCIUM BLOOMING ARTIFACT CORRECTION WITH DUAL ENERGY CT ANGIOGRAPHY

5.1 Abstract

5.1.1 Rationale and Objectives

Accurate percent stenosis evaluation in the presence of dense calcium is not currently possible with computed tomography polychromatic images (such as 120kVp) due to the calcium blooming artifact (Zhang et al. 2008). As a result, patients with high calcium scores are a relative contraindication for noninvasive computed tomography (CT) angiography (Nakanishi et al. 2005; Leber et al. 2005; Raff et al. 2005). The calcium blooming CT artifact causes artificial overestimating of the vessel lumen's stenosis due to display brightening of overlapping pixel intensities at the iodine and calcium border as visualized across display window settings. This work aims at markedly reducing this artifact by removing calcium with virtual non-calcium images obtained using dual energy computed tomography (DECT), making it possible for accurate evaluation of coronary stenosis in patients presenting with a high calcium burden.

5.1.2 Materials and Methods

A calcified vessel phantom was constructed with an iodine tube of known diameter in the presence of dense calcium hydroxyapatite (HAP). Iodine tube diameter measurements were made on the calcified phantom, comparing the known diameter with the measured diameter from polychromatic 120kVp images, 70keV and 100keV DECT virtual monochromatic images, and DECT virtual non-calcium images. Iodine area measurements were then made in patients presenting with severe calcium blooming artifacts and Agatston scores above 1,000 (IRB approved).

5.1.4 Results

For calcified phantom tests, measurements with DECT virtual non-calcium images were accurate to within 3% to 5% of the known iodine tube diameter whereas measurements with polychromatic 120kVp images varied from -38% to 43% of the known iodine tube diameter across display window settings (Bland-Altman Analysis). For patient tests, iodine area measurements from DECT virtual non-calcium images had a 49% lower standard deviation across display window settings as compared to DECT virtual monochromatic images, supporting a reduced dependence on display window settings for more accurate measurements of iodine vessel diameter with (DECT) virtual non-calcium images (p-values<0.05).

5.1.5 Conclusion

Since both the density and the amount of calcium burden in a vessel affect the degree of calcium blooming artifact, these data show that it is unlikely that any single window setting can be used with polychromatic 120kVp images to correctly specify residual vessel lumen in all patients. Stenosis evaluation of iodinated vessels having a high calcified plaque burden was found to be more accurate with DECT virtual non-calcium images than either polychromatic 120kVp images or DECT virtual monochromatic (70keV and 100keV) images.

5.2 Introduction

Fluoroscopic coronary angiography is the current gold standard for accurate assessment of stenosis even in the presence of highly attenuating calcified plaques. However, the cost and risk associated with fluoroscopic coronary angiography make it compelling to investigate noninvasive methods as a reasonable alternative. Coronary computed tomography angiography (CCTA) provides a noninvasive test for the presence of coronary artery disease but is unable to accurately assess stenosis in the presence of highly attenuating calcified plaques (Nakanishi et al. 2005). The calcium blooming artifact, caused by highly attenuating calcified plaques, distorts

stenosis visualization and confounds the percent stenosis measurement observed in polychromatic (kVp) images (Leber et al. 2005; Raff et al. 2005).

5.2.1 Calcium Blooming Artifact in Coronary Arteries

CCTA exams acquire an iodinated image set with polychromatic-derived Hounsfield units (HU). A polychromatic x-ray beam is characterized by several x-ray quanta energies being present in the beam versus a monochromatic beam where all x-ray quanta are of a single energy level. Polychromatic images suffer from the calcium blooming artifact and can create a falsely increased appearance of stenosis in areas of highly attenuating calcium (Nakanishi et al. 2005; Raff et al. 2005). Patients having a known high calcium burden may be contraindicated for a CCTA exam. The calcium blooming artifact arises from dense and/or large calcium plaques and the polychromatic image's dependence on display window settings (Leber et al. 2005). The operator selected window value will significantly change the perceived extent of highly attenuating (bright) materials that have intensity values above the maximum window value. In Figure 5.1, three different maximum window settings are applied to the same polychromatic image of a patient's vessel. Pixel values from cross-sectional profiles through calcium and iodine are depicted in the intensity line plot.

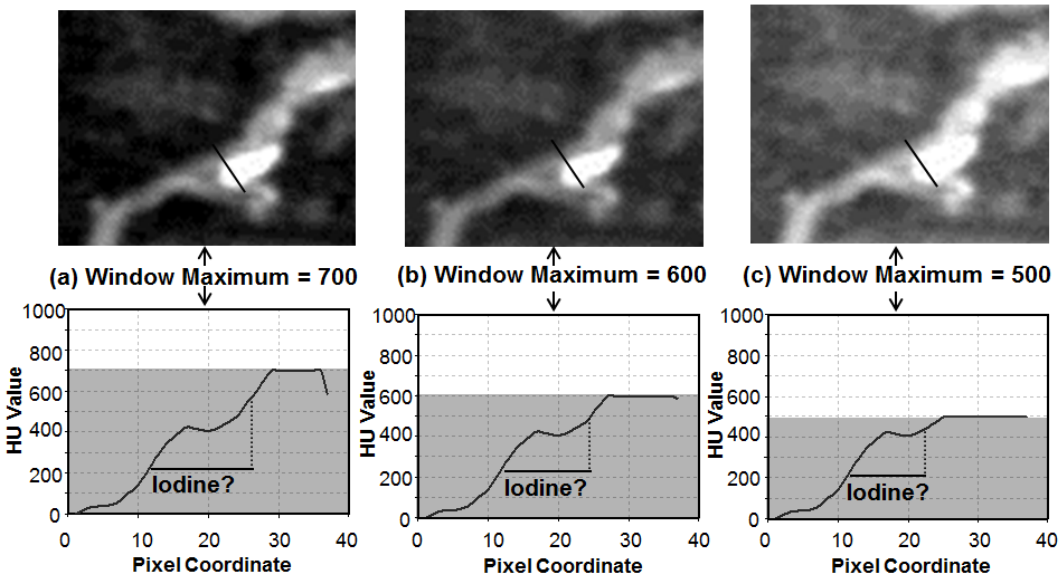

Figure 5.1: Left anterior descending (LAD) coronary artery with calcium blooming and window maximum decreasing left to right from 700HU (a) to 600HU (b) to 500HU (c) while the window width is constant at 600HU. The pixel intensity profile at each setting is shown below the polychromatic images corresponding to the line plot through the image. Note that the width of the calcified plot is expanding.

Manipulating the display width and level by the radiologist to evaluate vessel patency alters the perceived residual diameter. Visualized iodine (a) is enhanced by reducing the maximum window setting (b and c). However the intensity profiles below each image have two peaks, with iodine represented by the left peak (~400HU) and calcium represented by the right peak (~800HU). The two bright intensities overlap as the window maximum is reduced, confounding the evaluation of material borders. Brightening iodine has the unintended consequence of having more pixels to appear white like calcium, i.e. the calcium blooming artifact is occurring. Polychromatic display window settings can't be standardized for all patients because the extent of the calcium blooming artifact depends both on the density and amount (mg) of calcium present.

5.2.2 Expanding on Prior Works

The blooming artifact will occur with high concentrations of iodine or metal (biopsy needles) or any highly attenuating material. Previous studies have presented iodine blooming reduction techniques using correction algorithms and three-material decomposition with DECT (Boll et al. 2008; Clavijo and Pelc 2009; Flohr and Ohnesorge 2008). The enhancement correction algorithms showed consistent and accurate measurements of iodine, correcting for the iodine blooming artifact, when iodine measurements are made without the presence of calcium (Alvarez and Macovski 1976). Three-material decomposition has been shown to accurately quantify calcium in the coronary arteries, without describing the effects of calcium blooming on the perceived iodine content (Boll et al. 2008; Flohr and Ohnesorge 2008).

I expand on prior works with the analysis of iodine content in the presence of severe calcium blooming. The operator selected display window settings are key to routine visualization of vasculature but also contribute to the variability of the calcium blooming artifact and variability of perceived iodine content. I therefore included window setting choices in my investigation of improving the accuracy of coronary stenosis evaluation with DECT coronary angiography, specifically addressing vessels suffering from the calcium blooming artifact.

5.3 Materials and Methods

5.3.1 Scanning Protocols

Fast switched DECT technology emits x-ray exposures and detects them within 200 microseconds, collecting low energy and high energy measurements separated by 200 microseconds at effectively every angle of x-ray exposure. My work used fast switched DECT technology from the GE HDCT750 GSI scanner to generate virtual monochromatic images and material basis images from the low energy and high energy polychromatic measurements as proposed by earlier theoretical work (Alvarez and Macovski 1976; Xu et al. 2009). DECT virtual

monochromatic images are reconstructed by estimating the water and iodine linear attenuation combination that would be equivalent to the voxel projection measurements of the low energy and high energy data. Once the water and iodine linear attenuation values are estimated, they can be combined to represent the whole image at any keV energy found in the NIST x-ray attenuation tables, creating a virtual monochromatic image (Goodsitt, Christodoulou, and Larson 2011; NIST 1996).

Material basis images separate the linear attenuation measurements to generate two complete image sets. An Iodine(Calcium) image can be created that displays the iodine attenuation (but not the calcium attenuation) values from an iodine and calcium combination, while the Calcium(Iodine) image displays the calcium attenuation values from the same iodine and calcium combination (Johnson et al. 2007). Both fast switch DECT scans and conventional 120kVp CT scans were performed on a calcified vessel phantom and nine patients (HIPAA and IRB compliant). The protocol parameters used for this study are described in Table 5.1.

Table 5.1: Scanning protocol parameters for phantom and patient calcium blooming tests.

	Phantom 120kVp Scan	Phantom DECT Scan	Patient 120kVp Scan	Patient DECT Scan
Manufacturer	GE Healthcare	GE Healthcare	GE Healthcare	GE Healthcare
Model	Discovery HD CT750 64	Discovery HD CT750 64	Discovery HD CT750 64	Discovery HD CT750 64
Acquisition	Helical	Helical	Cine	Cine
Data Channels	32 x 0.625	32 x 0.625	64 x 0.625	64 x 0.625
Pitch	0.531	0.531	0.22	0.22
Rotation	0.5sec	1sec	0.35sec	0.35sec
Tube Voltage	120kVp	80kVp, 140kVp	120kVp	80kVp, 140kVp
Tube Current	600mA	600mA	600mA	715mA
Scan FOV	50cm	50cm	50cm	50cm
Recon FOV	10cm	10cm	10cm	10cm
Recon Plane	Coronal	Coronal	Axial	Axial
Recon Filter	Standard	Standard	Standard	Standard
Recon Slice Thick	0.625mm	0.625mm	0.625mm	0.625mm
Recon Increment	0.625mm	0.625mm	0.625mm	0.625mm
Recon ECG Phase	N/A	N/A	75%	75%
Recon Time	30sec	45sec	30sec	45sec
Contrast Material	Omnipaque350	Omnipaque350	Omnipaque350	Omnipaque350
CTDIvol	49.83mGy	65.64mGy	33.95mGy	30mGy

Conventional CCTA images are obtained at 120kVp, making 120kVp images appropriate for comparison in my work (Funabashi et al. 2004). Virtual monochromatic images are theoretically free of beam hardening and therefore of interest for correcting the calcium blooming artifact. The 70keV image type was evaluated because it is the effective energy equivalent to 120kVp for the (average patient) water phantom used to calibrate the CT scanner. The 100keV image type was evaluated because the 100keV beam energy penetrates the calcium more easily than 70keV, possibly reducing the calcium blooming artifact. For virtual non-calcium image testing, Iodine(Calcium) images were evaluated as an attempt to separate out the calcium and leave the iodine free of the calcium blooming artifact (Brodoefel, Burgstahler, et al. 2008; Choi et al. 2004). Iodine(HAP) images were also evaluated as a virtual non-calcium images since HAP represented calcium in the calcified vessel phantom.

5.3.2 Calcium Blooming Artifact Phantom Tests

In order to visualize the calcium blooming artifact and test the DECT image types, a calcified vessel phantom was created that combined an iodine filled tube inside of a HAP filled tube (iodine in Omnipaque350; GE Healthcare, Princeton, NJ) (HAP; Berkeley Advanced Biomaterials, Berkeley, CA). The iodine tube had a known inner diameter of 1.9mm, a wall thickness of 0.2mm, and an iodine contrast material of 400HU (as measured with 120kVp). The outer HAP tube had a known inner diameter of 10mm and calcium HAP material of 700HU (as measured with 120kVp) (Leber et al. 2005). Both tubes were made of polypropylene. The phantom was scanned in a 25cm diameter by 20cm long water bath both with the “Phantom 120kVp Scan” protocol and with the “Phantom DECT Scan” protocol from Table 5.1. Figure 5.2 shows the calcified vessel phantom and the water bath in which it was scanned.

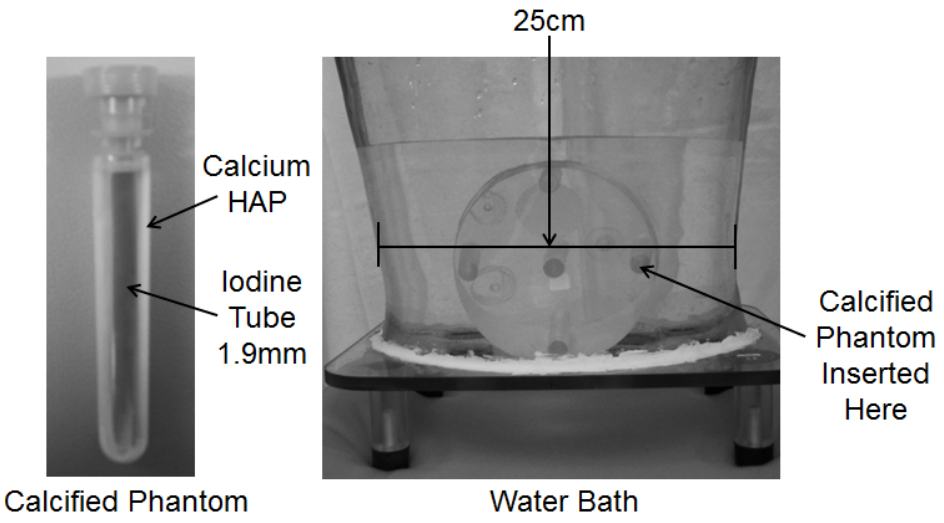

Figure 5.2: Calcified plaque phantom scan setup. The calcified plaque phantom (left) shows a calcium HAP section with a known diameter and an iodine section with a known diameter. Placing the phantom in the torso water bath (right) provided an experimental setup for scanning a contrast-enhanced iodine tube in the presence of highly attenuating calcium HAP.

Iodine tube diameter measurements were obtained using polychromatic 120kVp, virtual monochromatic (70keV and 100keV), and virtual non-calcium images. Visual comparisons involved changing the display window settings and observing the extent of the iodine lumen. Quantitative accuracy tests involved measuring five total image types, evaluating iodine tube measurement accuracy of the 1.9mm inner diameter iodine tube in the presence of dense calcium HAP. Iodine content was measured across several display window range settings, for all image types, and final settings were chosen so as to optimize the iodine enhancement near calcium. The normalized 100% range setting corresponds to a window with a maximum value equal to the maximum value of the calcium. Once this display window setting was determined, settings that extended the window beyond and below the maximum calcium value were tested. The iodine tube diameter was measured at five window settings, determined as the percentage of the window width extending from the background value to the maximum calcium value, for each of the six image types: 25%, 50%, 75%, 100% and 125%. For example, the range value of 125%

was defined as the nominal value of the maximum calcium intensity minus the background multiplied by 1.25.

For a single image type and display window setting, twenty-five independent measurements of diameter were automatically taken along the length of the iodine tube with a MATLAB program (MATLAB; Mathworks, Natick, MA). The iodine tube diameter was considered to be the linear distance from one side of the iodine to the other side. For 120kVp, 70keV, and 100keV images, pixels with intensities between the minimum iodine value and the half-maximum calcium value were counted as iodine toward the iodine tube diameter measurement, which was previously described for iodine measurements by Funabashi et al (Funabashi et al. 2004; Lau et al. 2005). For Iodine(Calcium) and Iodine(HAP) images, pixels with intensities above the half-maximum iodine value were counted as iodine toward the iodine tube diameter measurement, which was previously described for iodine measurements by Funabashi et al (Funabashi et al. 2004; Lau et al. 2005).

5.3.3 Calcium Blooming Artifact Tests in Patients

Fast switched DECT coronary angiography was scheduled on nine patients with calcium scores above 1,000 and under consent of approved IRB. Two patients were excluded from analysis due to technology failure. Of the seven patients receiving the “Patient DECT Scan” protocol from Table 5.1, data from four of the patients demonstrated severe calcium blooming artifacts. Image sets were generated for these four patients, including 70keV images, 100keV images, and Iodine(Calcium) images. Visual assessment involved changing the display by an experienced cardiothoracic radiologist. Quantitative accuracy testing of the patient DECT images involved iodine measurements performed automatically with a MATLAB program at the same five display window settings as the phantom measurements: 25%, 50%, 75%, 100% and 125%. For a single image type and display window setting, the area of iodine near the calcium was measured

using the MATLAB program. For 70keV, 100keV and Iodine(Calcium) images, iodine pixel evaluation used the same criteria used in the phantom testing.

5.3.4 Statistical Tests

One way ANOVA and Bland-Altman error analyses were performed on the iodine tube diameter measurements recorded for the phantom testing. One way ANOVA was also performed on the iodine area measurements recorded for the patient testing.

5.4 Results

5.4.1 Calcium Blooming Artifact Correction in Phantoms

Figure 5.3 displays four different display window settings for visualizing the calcified vessel phantom with 120kVp polychromatic images, 70keV virtual monochromatic images, and Iodine(Calcium) virtual non-calcium images.

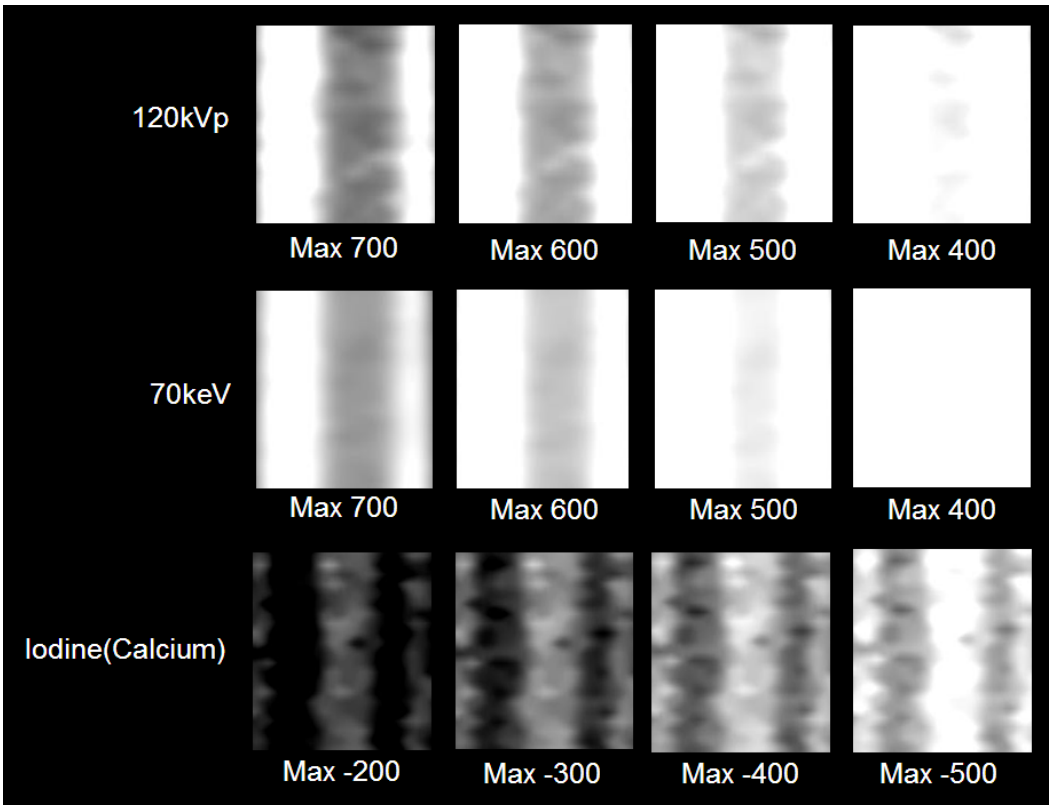

Figure 5.3: The calcified vessel phantom with four display window settings for 120kVp (top row), 70keV (middle row), and Iodine(Calcium) (bottom row). The maximum value is the maximum window value chosen for that image.

All of the images in Figure 5.3 are coronal cross sections of the calcified vessel phantom having calcium on both sides of an iodine tube. Both 120kVp and 70keV images show a strong dependence on the maximum window setting and are vulnerable to calcium blooming into the middle iodine region. The Iodine(Calcium) images appear less dependent on the display window settings. They avoid calcium blooming since calcium is virtually removed on both sides of the middle iodine region. Expanding upon visual observations, Figure 5.4 graphs the mean measured diameter values from all image types across the defined display window settings above and below 100%. Window range values above 100% extend the maximum window value above the maximum calcium or iodine value.

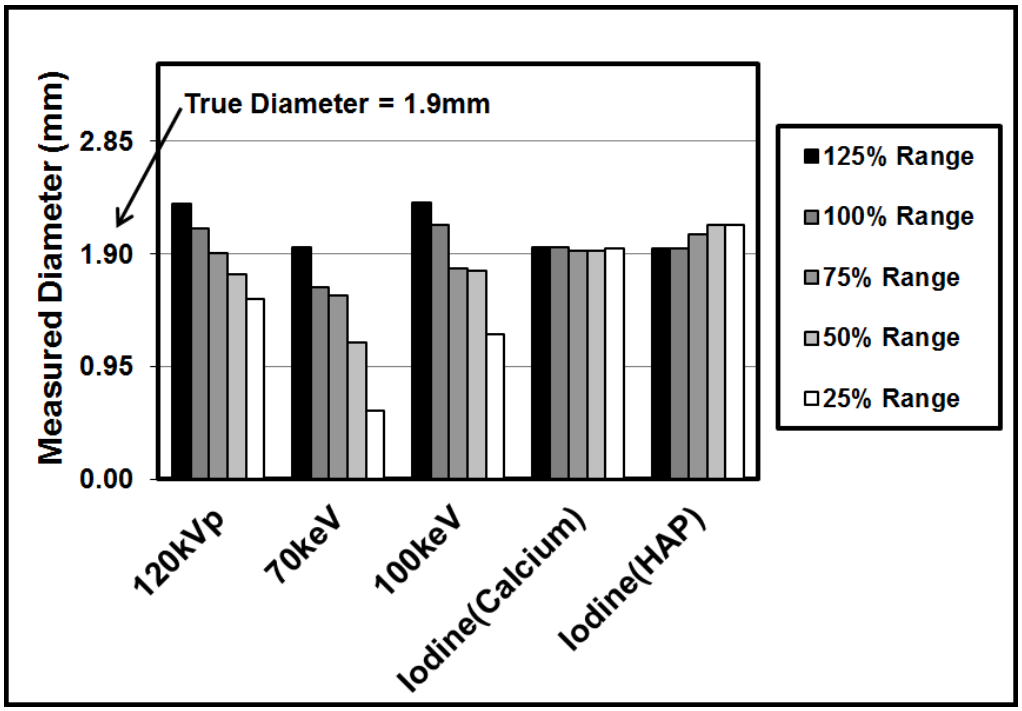

Figure 5.4: Results of diameter measurements with single energy and dual energy images. Dependence of diameter measurements on display window settings is shown here for several image types. The true diameter was 1.9mm, and the measured diameters are graphed from across 5 range settings.

In Figure 5.4, the reported diameter values at each window range are the mean values from 25 measurements along the iodine tube with the true diameter being 1.9mm. The least variability is seen for Iodine(Calcium) and Iodine(HAP). The accuracy of each image type can be observed in Figure 5.4 by comparing the image measurements with the known 1.9mm diameter. Note that virtual non-calcium images have the closest measurements to ground truth diameter.

For a 95% confidence interval, the one-way ANOVA (F-Test) results showed strong support for statistically significant mean values that differed according to image type (p-value of 0.6×10^{-18}). Error within a single image type's measurements was determined using the Bland-Altman analysis as shown in Figure 5.5.

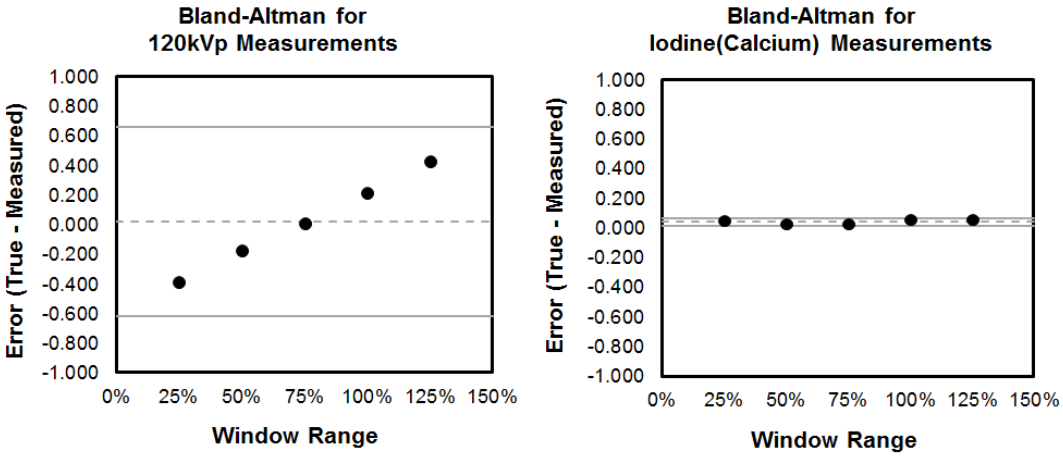

Figure 5.5: The Bland-Altman plots for mean diameter measurement error with the calcified phantom.

For the calcified vessel phantom, errors in measured iodine tube diameter ranged from -38% to 43% for 120kVp images, 3% to 5% for Iodine(Calcium) images, and 5% to 25% for Iodine(HAP) images across display window settings. The DECT virtual non-calcium images were the image type of least variability.

5.4.2 Calcium Blooming Artifact Correction in Patients

Figure 5.6 compares visualization of coronary stenosis in a left anterior descending (LAD) coronary artery. Each row in Figure 5.6 shows the same coronary artery for a particular image type across the five window range settings used to calculate iodine area.

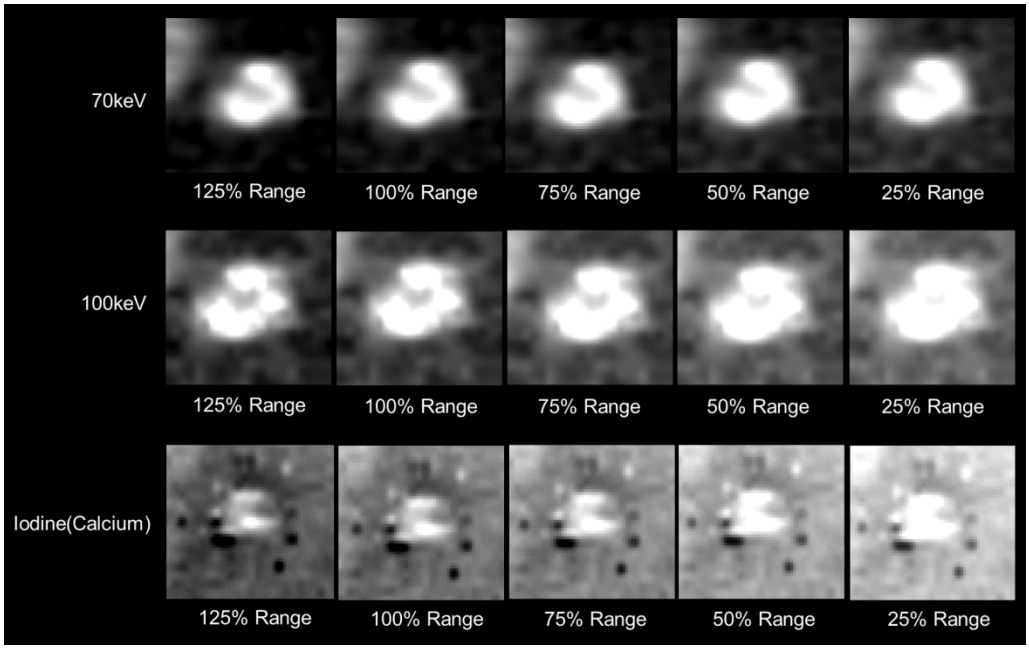

Figure 5.6: Patient axial vessel views with window width constant at 600 for 70keV and 100keV images (top and middle rows, Calcium bright) while the maximum changed from high to low. The window width was constant at 50 for Iodine(Calcium) images (bottom row, Iodine bright) while the maximum changed from high to low.

The iodine border visually decreases in the 70keV and 100keV images as the window range decreases from left to right in Figure 5.6. The bottom row shows Iodine(Calcium) virtual non-calcium images but with reduced dependence on display window settings for the representation of iodine content. Uniform whitening is apparent in the bottom right Iodine(Calcium) image, correctly depicting the true iodine tube diameter. The black and white speckle artifact throughout the Iodine(Calcium) images that could hinder measurements was due to early DECT image processing. Similar to the phantom measurements, iodine area was measured in each of the four patients with severe calcium blooming artifact. Figure 5.7 shows results of iodine area measurements from the four patients who demonstrated severe calcium blooming artifacts.

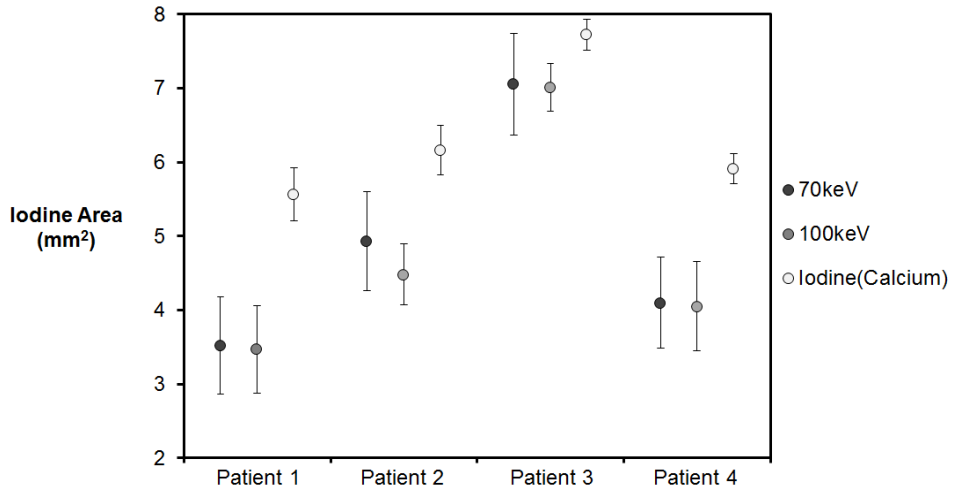

Figure 5.7: The mean values from measurements at five window ranges on patient images. They are reported with error bars representing the standard deviation of the mean values.

For a 95% confidence interval, the one-way ANOVA results show strong support for statistically significant mean values that differ according to image type for patient 1, patient 2, patient 3, and patient 4 (p-values = 0.07×10^{-5}, 0.05×10^{-4}, 0.05, and 0.01×10^{-1}, respectively). For all patients, virtual non-calcium images exhibited the lowest standard deviation. Note that for virtual non-calcium images, compared to polychromatic images or virtual monochromatic images, patent and obstructed regions are both free of overlapping bright intensities between calcium and iodine, presenting only bright iodine for stenosis evaluation. The images in Figure 5.8 show how the absence of calcium makes artery diameter measurements easier to perform in the absence of the calcium blooming artifact.

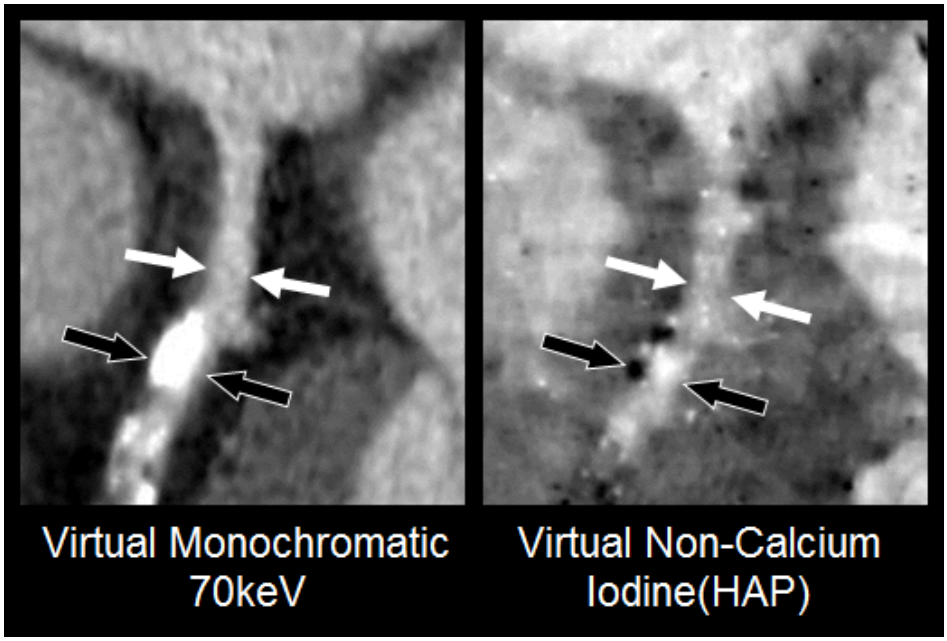

Figure 5.8: The left main coronary artery shown with a DECT virtual monochromatic image (left) and with a DECT virtual non-calcium image (right). The white arrows show where a measurement would be made to estimate the patent artery diameter where there is no obstruction. The black arrows show where a measurement would be made to estimate the artery diameter where there is obstruction.

The left 70keV image in Figure 5.8 has a strong display window dependence that could change the perceived percent stenosis. With the calcium removed in the right image of Figure 5.8, the iodine percent stenosis assessment is less dependent on display window settings. This particular patient in Figure 5.8 has calcium deposits to the left of the iodine. Once the calcium is removed, the patent region and obstructed region represent iodine with the same diagnostic task of measuring iodine free of the calcium blooming artifact.

5.5 Discussion

CCTA has an extremely high specificity to rule out coronary disease (Litt et al. 2012). However, the calcium blooming artifact is a significant hindrance in the use of CCTA for patients who may have a significant calcium burden. This serves as a major limitation, particularly in

elderly population who present with a lot of calcific atherosclerotic disease. CCTA, though with great potential, has been mostly useful in patients with low to intermediate risk (Nikolaou et al. 2003). Various scientific publications have alluded to the overestimation of stenosis in presence of significant calcium thus with a lower sensitivity to predict stenosis. The clinical utility of CCTA thus tends to utilize the negative predictive value of the modality (rule out disease) while the positive predictive value of CCTA has not lived up to its potential (Sajjadieh, Hekmatnia, and Keivani 2013). It is shown that, by using DECT, the calcium blooming artifact is removed with the image type Iodine(Calcium) since display window settings do not create blooming from calcium when altered.

Aspects of the calcified phantom testing could be improved for future study. Phantom measurements quantified iodine tube diameter from a coronal image of a calcified vessel phantom, which may not be applicable to institutions that measure iodine area from cross-sectional images of the longitudinal vessel. Phantom data characterized for accuracy using Iodine(Calcium) images were obtained at 65mGy and 49mGy. These radiation doses are greater than that used for obtaining patient data at 30mGy. The reduced error range found with Iodine(Calcium) images may not be achievable until improved denoising is available for Iodine(Calcium) images. The optimization of dose prescription with DECT is ongoing and will benefit from denoising techniques (Boas and Fleischmann 2012; Park et al. 2009).

DECT virtual monochromatic images of patients were shown to suffer the same calcium blooming artifact seen with conventional polychromatic images (Figure 5.6) and do not appear to provide any advantage for this application. DECT virtual non-calcium images had nearly a 50% lower standard deviation (better repeatability) in measurements of calcified stenotic patient vessels. The iodine lumen, as measured with the five display window settings, suggests that increasing or decreasing window selection does not vary as much as with DECT virtual monochromatic images due to the absence of highly attenuating calcium in the DECT virtual non-calcium images.

With DECT virtual non-calcium image types, image quality would benefit from the identification of areas where completely subtracted calcium appears as dark regions. These dark artifacts can be seen in Figure 5.9 where a calcium deposit has been removed and a darker region remains.

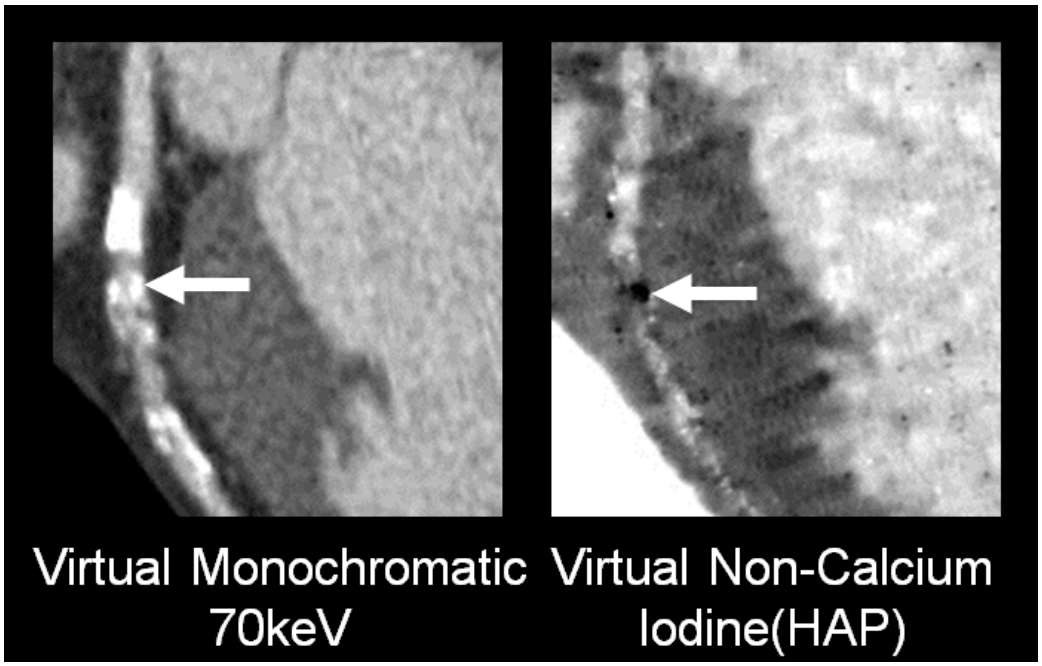

Figure 5.9: Dark artifact left from calcium removal. This left anterior descending coronary artery has several calcium deposits seen here in a DECT virtual monochromatic image (left) and a DECT virtual non-calcium image (right). The white arrow shows one particular calcium deposit that appears bright white in the left virtual monochromatic image and appears dark when removed in the right virtual non-calcium image.

Without identifying where calcium has been removed in Figure 5.9, the dark region may be mistaken to be risky lipid plaque since low-attenuating lipid appears dark in CT data images. The removed calcium deposit could be denoted with a color map or an iodine only image rendering. Although none of the patients in my study had a comparison from fluoroscopic coronary angiography catheterization, future studies would benefit from a comparison between stenosis measurements from virtual non-calcium images and from fluoroscopic coronary angiography.

Measurements from 120kVp, 70keV, and 100keV images underestimated iodine content by 9% to 70% compared to measurements from Iodine(Calcium) images, supporting an overestimation of calcium and stenosis across display window settings. Currently when non-invasive CT exams overestimate stenosis to be greater than 70%, patients potentially receive an invasive procedure that they may not need. These patients would benefit from virtual non-calcium images, obtained with non-invasive DECT, that more accurately measure percent stenosis regardless of dense calcium presence. Other patients may also benefit from virtual non-calcium image types for correcting the calcium blooming artifact with examinations for aortic stent placement and femoral diameter measurements for catheter access (Lau et al. 2005; Tran et al. 2009).

5.6 Conclusions

Virtual non-calcium images correct for the calcium blooming artifact through the removal of calcium in iodinated DECT coronary angiograms. With calcium removed, blood flow assessment can be performed using the injected iodine contrast material free from calcium blooming and window setting dependence. Virtual monochromatic images are not able to correct for the calcium blooming artifact because they are unable to remove calcium and remain dependent on window level settings. Confident stenosis evaluation can be achieved with virtual non-calcium images because they combine successful visualization of iodine and accurate measurement of iodine diameter in any artery of importance, regardless of calcium presence.

CHAPTER 6 AIM 4: CHARACTERIZATION OF CORONARY SOFT PLAQUE VULNERABILITY WITH DUAL ENERGY CT ANGIOGRAPHY

Coronary soft plaque vulnerability to rupture or erosion is based on the characteristics of the soft plaque, some of which can now be measured with dual energy computed tomography (CT) angiography: distance between aortic ostium and soft plaque, percent stenosis, and lipid content in plaque. Fabricated plaques with known stenosis were measured on center seeking curved multiplanar reformats and orthogonal images, but accuracy was low for measurements taken on each type of image reformat (10% to 40% error). The image reformats can be used qualitatively to convey the distance between the aortic ostium and soft plaque, as well as the lipid volume in the plaque. A multiple feature Support Vector Machine (SVM) model was developed to quantify the lipid content using dual energy CT images types (4% error). Combining the vulnerability parameters developed here could provide physicians with the metrics to determine risk of coronary events from a dual energy CT angiogram.

6.1 Introduction

Coronary CT angiography, with single energy CT, provides a non-invasive test for visualizing the extent of disease present in the arteries and chambers of the heart (O'Brien et al. 2007; Gerber, Kantor, and Williamson 2007; Hoffmann et al. 2005). Evaluations made with single energy CT angiography assess the viability of the heart, determining if a myocardial infarction has occurred and the likelihood of tissues to recover if disease is present (Brodoefel, Burgstahler, Heuschmid, et al. 2009; Gerber et al. 2006). One clinical goal that has been difficult to meet with polychromatic images from single energy CT is the ability to quantify the risk of future coronary events based on the vulnerability of coronary soft plaques to rupture or erosion. Soft plaques are early stage atherosclerotic disease and are comprised of both lipid and fibrous content. The

current work aims at quantifying soft plaque characteristics for use in assessing the vulnerability of coronary soft plaques.

6.1.1 Thin Cap Fibroatheroma of Soft Plaque

As a coronary soft plaque undergoes the repair process from atherosclerosis, scarring occurs across the surface of the plaque that protrudes into luminal blood flow, forming a thin cap fibroatheroma (TCFA) that keeps the necrotic core from coming in contact with blood. If the TCFA breaks and the necrotic core comes in contact with blood, thrombogenic agents in the necrotic core quickly attract inflammatory cells. The exposed necrotic core and attached inflammatory cells are vulnerable to detachment from the plaque site and formation of a coronary thrombus. In cases of sudden death due to coronary syndrome, coronary thrombus is caused most frequently by rupture (55% to 60%), then erosion (30% to 35%), and lastly calcified nodules (2% to 7%) (Virmani et al. 2006; Motoyama et al. 2009). The precursor to acute rupture is thought to be TCFA surrounding a necrotic core with a cap thickness less than 65μm. Computed Tomography (CT) currently achieves spatial resolution no greater than 350μm, which is not high enough to quantify meaningful TCFA thicknesses for assessing plaque vulnerability.

Plaque fatigue and cholesterol crystals have both been identified as possible precursors to coronary thrombus formation. Plaque fatigue is defined as an incremental failure progression under the influence of repetitive stresses (Versluis, Bank, and Douglas 2006). As the stresses increase in number and/or pressure, the plaque fatigues and possibly becomes more vulnerable to thrombus formation either by TCFA rupture or erosion at stress sites. Decreasing TCFA thickness notably decreases the cycles to rupture. However, CT may not be able to quantify fatigue because it begins in plaques with less than 50% stenosis and before patients have symptoms like chest pain or decreased cardiac function. Dual energy CT imaging may be able to quantify the lipid content in soft plaques in order to identify the presence of cholesterol crystals. As lipid content solidifies in the soft plaque, cholesterol crystals are form and begin to expand in

volume by as much as 25%. The expansion causes increased pressure on the TCFA, and the cholesterol crystals have been shown to pierce fibrous caps due to increased pressure and the sharp edges of the cholesterol crystals (Abela 2010; Abela et al. 2009). The main goals of this work are identifying possible characteristics of soft plaque, such as morphology and lipid content, that measure the vulnerability of soft plaque to coronary thrombus formation.

6.1.2 Soft Plaque Proximity to Aortic Ostium

Between 50% and 70% of fatal soft plaque ruptures occur in the proximal portion of coronary arteries, including the left anterior descending (LAD), left circumflex (LCX), and right coronary artery (RCA) (Virmani et al. 2006). The proximal portion of the artery is defined as the region close to the aortic ostium where the coronary artery branches off of the aorta. Soft plaque location in proximity to the aortic ostium could easily be obtained with CT images. The common center seeking curved multiplanar reformat (CSCMPR) already tracks the centerline of each coronary artery from the aortic ostium to its distal end, and distance measurements could be taken from the CSCMPR image. Distance from the soft plaque to the aortic ostium is commonly used to indicate the severity of damage that would occur in the event of a coronary thrombus. This is because increasing the proximity to the aortic ostium places the soft plaque where more tissues would be cut off from blood supply by a myocardial infarction.

6.1.3 Soft Plaque and Coronary Artery Stenosis

Coronary artery stenosis can lead to coronary thrombosis or myocardial ischemia. As previously mentioned, coronary thrombosis can form before stenosis reaches even 70%, while myocardial ischemia occurs with stenosis above 70%. Stenosis above 70% is then considered to be hemodynamically significant because it causes myocardial ischemia. In nearly two thirds of patients who suffered coronary thrombosis, soft plaques exhibited less than 70% diameter stenosis but were characterized by a large lipid core often greater than 40% of the soft plaque

volume (Shah 2003). Characterizing soft plaque vulnerability then depends more directly on the lipid content of the plaque and not the percent stenosis. This work aimed at determining optimal image reformats for measurement of lipid and fibrous content in soft plaque coronary stenosis.

6.1.4 Lipid and Fibrous Classification in Soft Plaque

Several methods have attempted to quantify the lipid content present in the coronary arteries but were unable to provide accurate quantification with single energy CT polychromatic image types (Horiguchi et al. 2007; Hausleiter et al. 2006; Kristensen et al. 2010). Once iodine is injected into the blood stream, the coronary CT angiogram images the heart at peak concentrations of the blood:iodine mixture in the coronary arteries. The iodine creates high contrast between the tissues of the heart and blood:iodine mixture, providing visualization of the blood distribution throughout the heart. The blood could not be visualized without the iodine because the x-ray attenuation properties of blood and heart tissue are too similar. However, the iodine is often so attenuating that it causes beam hardening artifacts which hinder the quantification of low attenuating tissues like coronary lipid plaques and fibrous plaques.

Coronary disease creates soft plaques in the coronary arteries that consist of both more vulnerable lipid content (mass density 0.9-0.99g/cc) and less vulnerable fibrous content (mass density 1.2-1.35g/cc). In the presence of beam hardening, the soft plaque attenuation may be artificially elevated to above the attenuation of water (Brodoefel, Reimann, et al. 2008). In other words, the low attenuating soft plaque appears to attenuate more highly than water, which is characteristic of a mass density greater than 1g/cc. A single HU threshold for lipid content is also not possible because iodine concentration shifts the lipid attenuation distribution and iodine concentration changes from patient to patient as demonstrated in Figure 6.2. Quantification of more vulnerable lipid plaque is further complicated by the overlap of lipid and fibrous attenuation distributions (Nair et al. 2002).

Dual energy derived images are investigated here for their ability to reduce beam hardening effects and to classify materials through material decomposition. Deaths (US) due to myocardial infarction are broken down into 50% from ruptured arteriosclerosis, 30% from ruptured atherosclerosis, 18% from eroded atherosclerosis, and 2% from calcified atherosclerotic nodules. Classifying lipid content in soft plaque could be used to characterize rupture vulnerability, while fibrous content could characterize erosion vulnerability. Lipid plaque has been attributed to rupture vulnerability due to the prevalence in coronary thrombi and its formation of cholesterol crystals (Shah 2003; Abela 2010). Fibrous plaque has been attributed to erosion vulnerability due to its prevalence in coronary thrombi. Whether coronary thrombosis is due to rupture or erosion, quantifying lipid and fibrous plaque content is a strong indicator of soft plaque vulnerability. This work aims at classifying lipid and fibrous content through classification with SVM utilizing the dual energy image types: virtual monochromatic and material basis pair images.

6.2 Research Design and Methods

6.2.1 Fabrication of Phantom Soft Plaques

Quantification studies using polychromatic 120kVp images show that lipid plaque measures 40HU-100HU and fibrous plaque measures 100HU-140HU in the presence of iodine (Horiguchi et al. 2007; Hausleiter et al. 2006; Dalager et al. 2011). The studies attribute the variation in lipid HU values to a number of variables: beam hardening from multiple levels of iodine concentration, HU shift due to plaque location within the injected iodine, HU shift due to plaque location within the CT gantry, and HU shift due to amount of plaque present. One quantification method automatically colorizes and measures the number of voxels that represent soft plaque but relies upon the user to input the HU range that represents soft plaque (Hausleiter et al. 2006). This approach has a high margin for inaccuracy given the variability in plaque HU

values across patients and does not quantify lipid plaque separate from fibrous plaque (Pohle et al. 2007).

In order to test classification of lipid and fibrous plaques with single energy CT and dual energy CT, coronary plaque phantoms were designed and fabricated for use in the previously built anthropomorphic beating heart phantom (Boltz et al. 2010; Pavlicek et al. 2008). The phantom plaques were designed in a 3D computer aided design environment called SolidWorks with designs for phantom plaques to fit in each coronary artery of the beating heart phantom: LAD, LCX, and RCA (Dassault-Systemes-SolidWorks 2008).

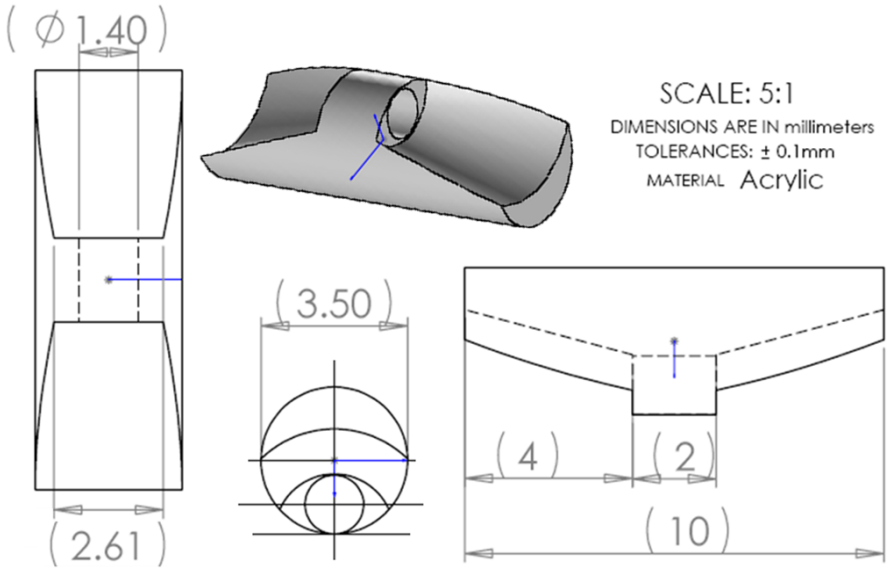

Figure 6.1: SolidWorks design for soft plaque phantoms. This design creates a plaque with a known 40% stenosis and a 3.5mm outer diameter.

Once the design from Figure 6.1 was created, dimensions could be changed to create different percent stenosis plaques as well as different outer diameters depending on the diameter of the vessel of interest. Phantom soft plaques were fabricated with mass densities of 0.92g/cc, 0.96g/cc, and 1.2g/cc as well as stenoses in each artery of 40%, 60%, and 80% by diameter. These stenosis values were chosen for testing image measurements near the 70% hemodynamically significant threshold. The known outer diameter of each plaque made it possible to place plaques either proximally or medially in the phantom heart. Once deployment of

phantom plaques into the heart was achieved, the known density and volume of each plaque could then be compared between SVM models from single energy CT and dual energy CT.

6.2.2 Stenosis Measurements with Phantom Soft Plaques

After fabricating the phantom soft plaques, a study was conducted to determine the best image plane for measuring stenosis created from the phantom plaques. CSCMPR images and images orthogonal to CSCMPR (OCSCMPR) images were constructed as image planes for testing stenosis measurements, chosen for their targeted visualization of coronary blood flow and plaques. Several considerations are made to assess soft plaque vulnerability to coronary thrombosis, including plaque proximity to the aortic ostium, whether stenosis is less than or greater than 70%, and whether the lipid content is greater than 40% of the soft plaque volume. Proximity to aortic ostium is automatically calculated in the formation of CSCMPR images, but stenosis and lipid content require user input and sophisticated classification methods.

Stenosis measurements were performed on CSCMPR and OCSCMPR images of the phantom soft plaques in the phantom heart. Reviewers included two radiologists and two 3D technologists experienced in cardiac measurements, and they measured the diameter of the patent region and the diameter of the stenosis region. The reviewers received images of plaques from a coronary CT angiogram performed on the phantom plaques and heart. Table 6.1 shows the plaques included for reviewers to measure.

Table 6.1: Soft plaque distributions deployed for plaque quantification testing. For example, Test 1 deployed 3 plaques in the phantom with a phantom plaque in the LAD that measured 0.92g/cc and 40% stenosis.

	LAD Phantom Plaque	LCX Phantom Plaque	RCA Phantom Plaque
Test 1	0.92g/cc 40% stenosis	1.2g/cc 60% stenosis	0.92g/cc 80% stenosis
Test 2	0.96g/cc 40% stenosis	0.96g/cc 60% stenosis	0.96g/cc 80% stenosis
Test 3	1.2g/cc 40% stenosis	0.92g/cc 60% stenosis	None
Test 4	0.92g/cc 80% stenosis	0.92g/cc 80% stenosis	0.92g/cc 40% stenosis
Test 5	0.96g/cc 80% stenosis	0.96g/cc 80% stenosis	1.2g/cc 80% stenosis
Test 6	0.92g/cc 60% stenosis	1.2g/cc 40% stenosis	1.2g/cc 40% stenosis
Test 7	0.96g/cc 40% stenosis	1.2g/cc 60% stenosis	None

The plaques described in Table 6.1 included all densities in all coronary arteries and stenosis above and below 70% in all coronary arteries. Once the reviewers had measured stenosis in all plaques, t-tests were individually performed on all plaques of the same density and stenosis in order to determine if there was a difference in the measurements made with CSCMPR images versus OCSCMPR images. Then Bland-Altman error was calculated to compare the error found with each image type.

6.2.3 Lipid and Fibrous Classification in Patient Soft Plaques

Lipid quantification was attempted with dual energy CT as a multiple step process: inject iodine for plaque visualization, classify plaque pixels based on training data, and quantify the amount of lipid present in plaque pixels. Although increased lipid levels are a strong indicator of vulnerability to coronary thrombosis, lipid quantification has not been accurate enough with single

energy CT to be incorporated into the conventional coronary CT angiogram evaluation (Kitagawa et al. 2009). Lipid plaque has a lower mass density (0.9-0.99 g/cc) than water (1.0 g/cc), but in the presence of iodine, lipid plaque measures between 40HU to 100HU with 120kVp imaging while water measures between -5HU and 5HU. Figure 6.2 shows the variability in patient soft plaque measurements as iodine content changed between patient scans.

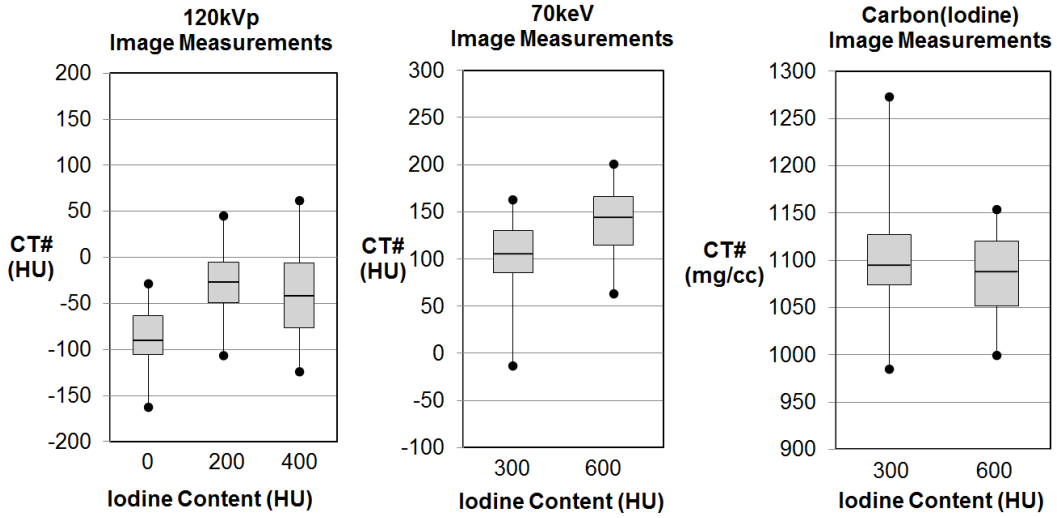

Figure 6.2: Patient soft plaque distributions in increasing iodine amounts. Measurements are taken in varying amounts of iodine from no iodine present to 600HU iodine content.

The three image types in Figure 6.2 have soft plaque measurements that varied in response to the iodine content present. Measurements from 120kVp support that soft plaque without iodine present elevates from 0HU to as much as 60HU in the presence of iodine. The variability in soft plaque pixel values was also seen in the measurements from 70keV and Carbon(Iodine) images, which was compelling support for using a classification system with several dual energy image types (Liaw and Wiener 2002; Schoenhagen, Barreto, and Halliburton 2008; Schroeder et al. 2004; Tkaczyk and Langan 2009). The training data sets for SVM consisted of the phantom lipid and fibrous plaques scanned within the phantom heart and thorax. Single energy and dual energy scans were performed on the phantom soft plaques as outlined in Table 6.2, then SVM analysis calculated the specificity and error exhibited by measurements with

single energy versus dual energy images. An expanded list of parameters for phantom plaque scans is given in Table 6.3.

Table 6.2: Testing parameters for soft plaque classification scans. For example, Scan 5 scanned phantom lipid and fibrous plaques with 350HU iodine content in the phantom coronaries, 120kVp CT acquisition, and 23mGy radiation dose.

	Iodine Content	CT Acquisition	Radiation Dose
Scan 1	Saline Only	120kVp	23mGy
Scan 2	Saline Only	DECT	19mGy
Scan 3	200HU	120kVp	23mGy
Scan 4	200HU	DECT	19mGy
Scan 5	350HU	120kVp	23mGy
Scan 6	350HU	DECT	19mGy
Scan 7	350HU	120kVp	14mGy
Scan 8	350HU	DECT	29mGy
Scan 9	350HU	DECT	63mGy

Building an SVM classifier to be used on patient data required identifying the image type features that reduced error, selecting a classification kernel, and optimizing the parameters of the classification kernel. Using the training data scans explained in Table 6.2, the total number of false negatives was calculated for single energy and dual energy image types using single feature SVM. Lipid content indicates highest risk of coronary events, and the more false negatives exhibited by an image type, the more lipid that would be missed by measurements with that image type. Once the false negatives were calculated, image types that minimized false negatives were used for multiple feature SVM, utilizing the radial basis function (RBF) as suggested by previous work (Hongzong et al. 2007).

For 120kVp feature consideration, the SVM classifier was built with Scan 5 (5% Iodine, 23mGy) and tested on Scan 3 (2.5% Iodine, 23mGy) as well as Scan 7 (5% Iodine, 14mGy). For dual energy feature considerations, the SVM classifier was built with Scan 6 (5% Iodine, 19mGy) and tested on Scan 4 (2.5% Iodine, 19mGy) as well as Scan 8 (5% Iodine, 29mGy), performing the tests individually on virtual monochromatic images 50keV to 140keV in 10keV increments and

on material basis images from the materials: water, iodine, calcium, and carbon. Optimization of multiple feature SVM involved minimizing error on RBF kernel parameters (e.g. C and γ).

Under IRB consent, seven patient exams were obtained with cardiac dual energy CT, resulting in one data set with soft plaques suspect for lipid content and imaged at two levels of iodine content. The scanning parameters used to obtain the patient data were recorded in Table 6.3. The SVM model built with the features and parameters from Figure 6.6 was used on the patient data set with possible lipid plaque to determine the lipid volume compared to the total volume of the plaque.

Table 6.3: Patient scan parameters for single and dual energy CT soft plaque testing.

	Phantom 120kVp Scan	Phantom DECT Scan	Patient 120kVp Scan	Patient DECT Scan
Manufacturer	GE Healthcare	GE Healthcare	GE Healthcare	GE Healthcare
Model	Discovery HD CT750 64	Discovery HD CT750 64	Discovery HD CT750 64	Discovery HD CT750 64
Acquisition	Cine	Cine	Cine	Cine
Data Channels	64 x 0.625	64 x 0.625	64 x 0.625	64 x 0.625
Rotation	0.6sec	0.6sec	0.35sec	0.35sec
Tube Voltage	120kVp	80kVp, 140kVp	120kVp	80kVp, 140kVp
Tube Current	Varied	Varied	600mA	715mA
Scan FOV	50cm	50cm	50cm	50cm
Recon FOV	15cm	15cm	15cm	15cm
Recon Plane	Axial	Axial	Axial	Axial
Recon Filter	Standard	Standard	Standard	Standard
Recon Slice Thick	0.625mm	0.625mm	0.625mm	0.625mm
Recon Increment	0.625mm	0.625mm	0.625mm	0.625mm
Recon ECG Phase	N/A	N/A	75%	75%
Recon Time	30sec	45sec	30sec	45sec
Contrast Material	Varied Visipaque320	Varied Visipaque320	Varied Omnipaque350	Varied Omnipaque350
CTDIvol	Varied	Varied	33.95mGy	30mGy

6.3 Results and Discussion

6.3.1 Attenuation Measurements of Fabricated Phantom Plaques

Phantom lipid plaques (0.96g/cc) and fibrous plaques (1.2g/cc) were imaged with the CT protocols described in Table 6.3 in the absence and presence of iodine. Attenuation values for each plaque type were then plotted in Figure 6.3 for no iodine present, 200HU iodine content present, and 350HU iodine content present. The box plots show variation in the plaque types' measured attenuation values in relation to beam hardening from iodine and changing radiation dose.

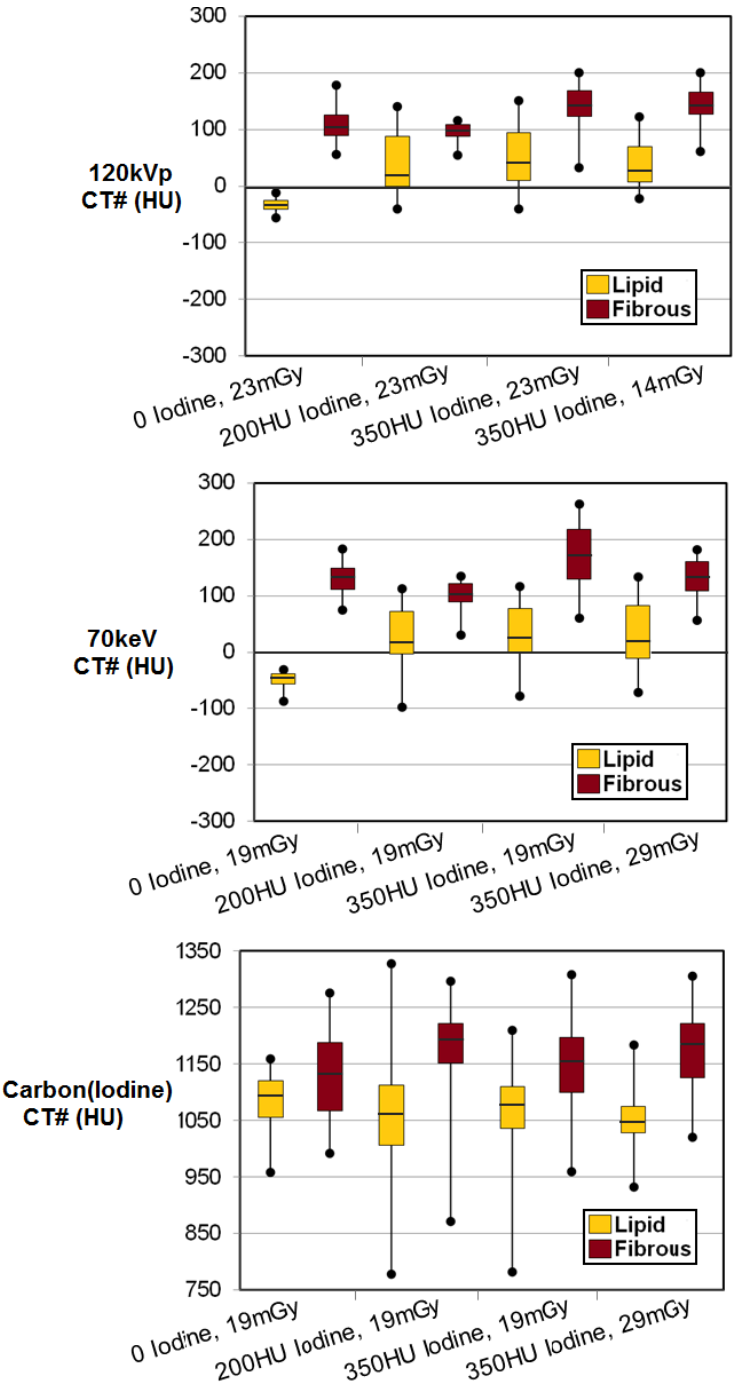

Figure 6.3: Box plots of lipid and fibrous phantom plaques captured in single energy and dual energy images.

The 120kVp box plot in Figure 6.3 shows a nearly 50HU separation between lipid plaque and fibrous plaque when iodine is not present. When 200HU and 350HU iodine content is added,

the lipid and fibrous distributions have almost complete overlap of values. This overlap is the reason that single energy HU values alone can not be used to characterize lipid plaque separately from fibrous plaque. The 70keV box plot shows almost equivalent trends with lipid and fibrous distributions separated when no iodine is present and overlapping when iodine is present. Changing the radiation dose does not appear to have a significant effect on the lipid and fibrous distributions. For the Carbon(Iodine) box plot, the lipid and fibrous distributions have a lot of overlap but tend to remain in the same range between 200HU iodine and 350HU iodine. No single image type successfully separates lipid and fibrous plaques for accurate quantification. For this reason, several virtual monochromatic and material basis image types were used to develop an SVM model that could reliably classify lipid and fibrous plaques for quantification.

6.3.2 Stenosis Measurements with Phantom Soft Plaques

Phantom soft plaques were deployed in the LAD, LCX, and RCA of the phantom heart. The fabricated phantom plaques can be seen in Figure 6.4 with examples for all plaque densities and visualization in both CSCMPR and OCSCMPR images.

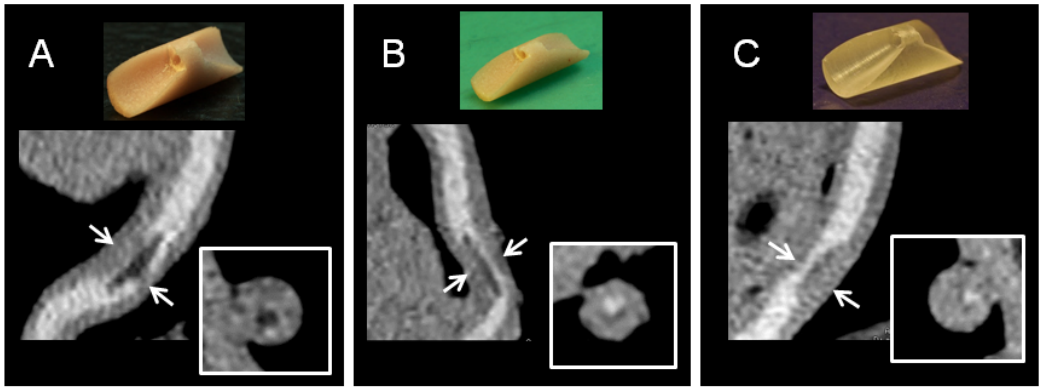

Figure 6.4: Phantom soft plaques with CSCMPR and OCSCMPR images. Arrows denote where OCSCMPR images were reformatted. “A” is 0.92g/cc with 80% stenosis; “B” is 0.96g/cc with 80% stenosis; “C” is 1.2g/cc with 80% stenosis.

Phantom soft plaques presented the reviewers with plaques of known percent stenosis as well as the same iodine content used in patients (400HU as measured with 120kVp). The phantom

plaques visualized in Figure 6.4 are deployed in phantom coronary arteries from mold casts of patient coronary arteries. The phantom plaques were scanned with the same 120kVp technique used in patients and within a phantom thorax that attenuates as a patient thorax would attenuate. All of the imaging challenges presented with patients were present in the testing of stenosis produced by the phantom soft plaques, including a 60 beats per minute heart rate. The strategic replication of the patient imaging challenges was done in order to ensure meaningful results from measurements made on the phantom soft plaques. The error in measuring stenosis across plaque densities and coronary arteries is shown in Figure 6.5.

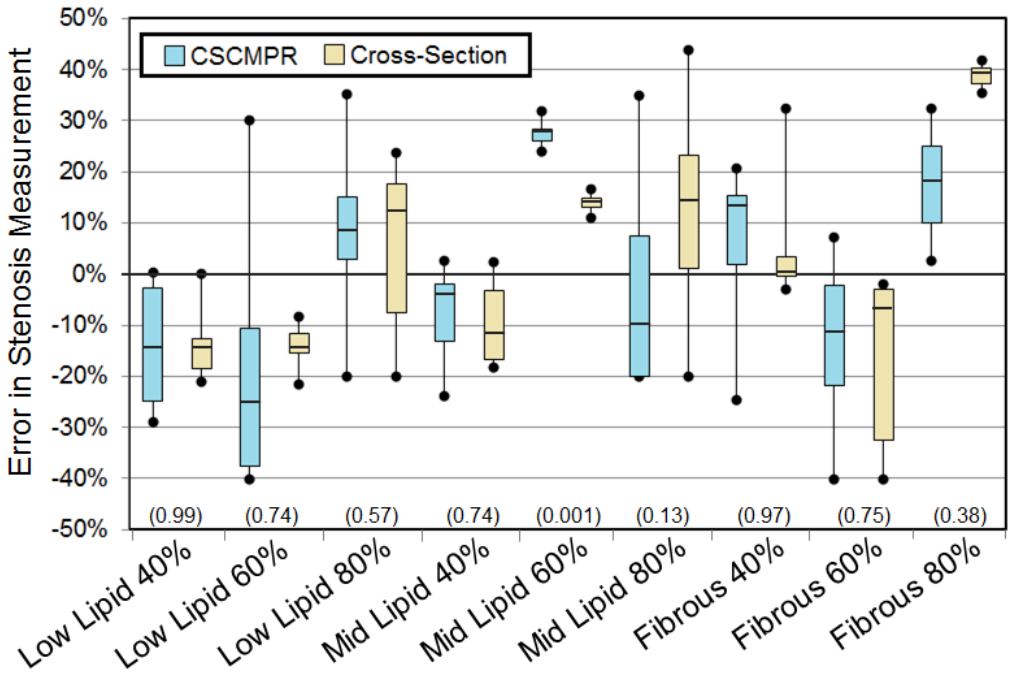

Figure 6.5: Box plot of error in stenosis measurements for CSCMPR and OCSCMPR images. The horizontal axis shows the plaque density type and stenosis percentage for the diameter measurements. P-Values (reported in parenthesis) compare means of stenosis measurements between CSCMPR and OCSCMPR. The middle bars of the box plots represent the median stenosis measurement.

Phantom plaques are characterized by density-type in Figure 6.5; very low density lipid is 0.92g/cc, low density lipid is 0.96g/cc, and fibrous is 1.2g/cc. Given the distribution of errors seen in Figure 6.5, measurements were not significantly more accurate based on image type or

phantom plaque density. After performing t-tests individually on each plaque data set, it was determined that stenosis measurements did not consistently differ between CSCMPR and OCSCMPR image types as shown by the many high p-values in parenthesis of Figure 6.5. These data show that CSCMPR or OCSCMPR images achieve similar error across plaque densities and stenosis values. Several factors strongly influenced the reviewers as stenosis measurements were made with the diameter technique. Reviewers differed in identifying which portion of the plaque exhibited the highest stenosis, changing the location of diameter measurement between reviewers. Only a portion of the reviewers magnified the image when measuring stenosis, making the distance placement easier than reviewers who did not magnify.

The large and varying errors seen with this diameter method, along with the strong reviewer influence, make it compelling to investigate other methods of stenosis quantification. Analysis of iodine and plaque pixels could be used to automatically calculate stenosis values by area or diameter (Sato et al. 2008; Gouya et al. 2009). Although diameter stenosis measurements are equally poor with CSCMPR and OCSCMPR images, it may be beneficial to use both image types for identifying and conveying the soft plaque vulnerability to rupture or erosion. CSCMPR images could be used for identifying the soft plaque and obtaining its distance from the aortic ostium, while OCSCMPR images could be used to visualize stenosis as well as lipid and fibrous content as classified by an SVM model.

6.3.3 Lipid and Fibrous Classification in Patient Soft Plaques

Measurements of the known lipid and fibrous plaques were made with 120kVp images, virtual monochromatic images, and material basis images. After performing single feature SVM on each image type individually, 120kVp images were found to have 9% of the pixels misclassified as false negatives and a total of 17% error. The virtual monochromatic and material basis images that had equivalent or less false negatives/error, compared to 120kVp images, were then chosen for building an SVM model. The optimization of the SVM model is seen in Figure 6.6

where the testing data set was run 200 times through the SVM model created by the testing data set, changing kernel function parameters C and/or γ for each iteration.

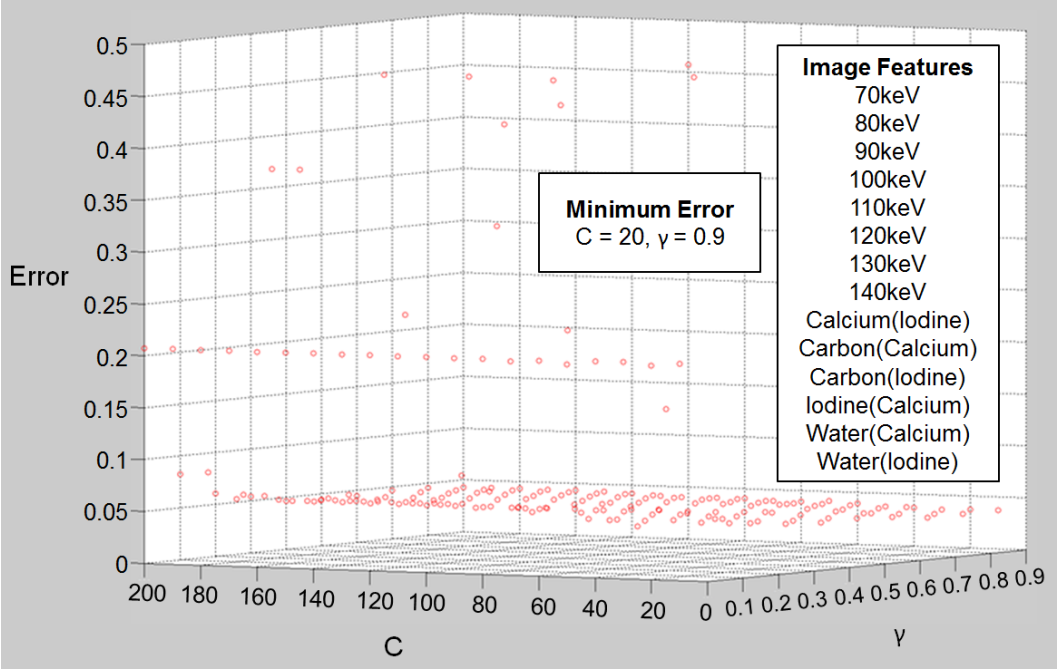

Figure 6.6: Optimization of the SVM model. RBF kernel features were optimized using the training data scans explained in Table 6.2. Error was minimum (4%) for SVM classification with RBF parameters of C = 20, and γ = 0.9.

The optimal SVM classification model was determined to be with RBF kernel parameters of C = 20 and γ = 0.9, achieving a 4% total error on the testing data set. These parameters were then used to classify lipid and fibrous pixels in patients. The patient images were reformatted to visualize the soft plaques present, and all pixels of a given soft plaque were measured for classification after excluding pixels representing iodine. Soft plaque identification required visualizing the plaque as protruding into the lumen, which was accomplished with the CSCMPR image type shown in Figure 6.7 (left). This image type was also optimal for quantifying the distance from the aortic ostium for the soft plaque's location.

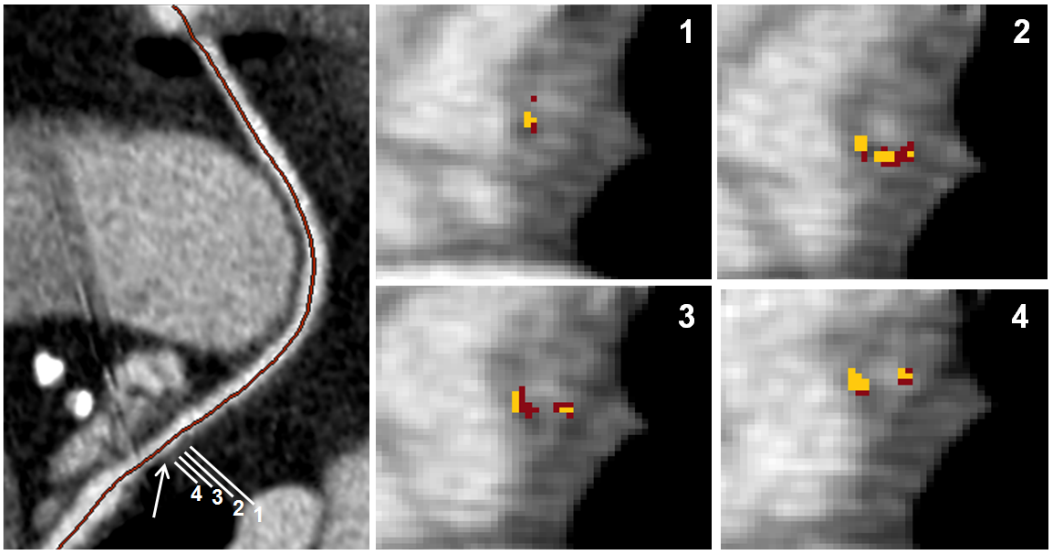

Figure 6.7: Visualization of a coronary soft plaque (arrow on left image) using a CSCMPR image (left) and OCSCMPR images (1-4). The straight lines on the left image show where OCSCMPR images were reformatted, and the red line is the central line used to reformat the CSCMPR images. Gold pixels represent lipid plaque and maroon pixels represent fibrous plaque in OCSCMPR images (1-4).

Figure 6.7 summarizes the results of SVM classification for a patient's coronary soft plaque and serves as a model for conveying the vulnerability of soft plaque to rupture or erosion. The patient exam in Figure 6.7 utilized iodine content at 300HU, which is within the 200HU to 350HU iodine range used in the training data set. A comprehensive reporting of the vulnerability to plaque rupture or erosion includes: distance between aortic ostium and soft plaque, percent stenosis, and percentage of plaque that is comprised of lipid content. The patient exam from Figure 6.7 exhibits 8cm from aortic ostium to soft plaque, 40% stenosis, and 35% lipid volume to total volume. The distance from aortic ostium to soft plaque and percent stenosis are easily captured with minimal input in measuring software. The 35% lipid volume is calculated from the optimized SVM model. Even though the patient soft plaque in Figure 6.7 has lipid content, the vulnerability to rupture or erosion is moderate based on the lipid volume being below 40% as well as the large distance from the aortic ostium to the soft plaque. The strongest indicator of rupture vulnerability is the extent of lipid content present, which has not been possible with single energy CT techniques.

6.4 Conclusions

Soft plaque vulnerability to rupture is heavily dependent on lipid content, while vulnerability to erosion is more heavily dependent on distance from soft plaque to aortic ostium and percent stenosis. Measurements with CSCMPR and OCSCMPR images both achieved low accuracy of percent stenosis with the use of manual operator measurements and not automated algorithms. However, it may be beneficial to use these image types qualitatively to identify and convey the vulnerability characteristics of soft plaques. Distance from aortic ostium, percent stenosis, and lipid content were ideally conveyed for a patient's coronary soft plaque with the use of CSCMPR images and OCSCMPR images. The SVM model developed here exhibited only 4% error for classifying lipid and fibrous plaques in the presence of 300HU iodine content, showing a 35% lipid volume in patient data and associated moderate vulnerability of the plaque to rupture or erosion.

6.5 Clinical Significance

Soft plaque vulnerability and risk of coronary events remain crucial clinical goals of the CT angiogram (Brodoefel, Burgstahler, Sabir, et al. 2009). This work successfully calculates lipid content based on SVM classification and dual energy CT data for the purpose of soft plaque vulnerability characterization. This work also shows how CSCMPR images could be used for identifying the soft plaque and obtaining its distance from the aortic ostium, while OCSCMPR images could be used to visualize stenosis as well as lipid volume. These parameters combined provide the physician with the metrics for developing scores that quantify risk of coronary events due to plaque rupture or erosion. The greatest significance of the vulnerability metrics formulated here is the ability to take the metrics and develop a coronary risk score that can be calculated as part of the CT angiogram.

CHAPTER 7 FUTURE WORK AND CLINICAL APPLICATIONS

There is a mix of clinical goals and engineering solutions throughout this body of work. Physicians attempt to diagnose the severity of coronary artery disease while CT angiography provides visualization of morphology, blood flow, and density of plaque present. This body of work aimed at shifting what is provided to the physician from CT angiography, using dual energy images to correct for highly attenuating coronary plaques and to quantify vulnerable soft plaques even to produce a percent lipid volume value. My work succeeds at providing the physician with more quantifiable measures of coronary disease severity for a subset of patients, but expanding my work could make these metrics available for a significant number of patients.

7.1 Aim 1: The Anthropomorphic Beating Heart Phantom

Multiple clinical questions have been answered with the fabricated beating heart phantom in this work. It was determined, using the heart phantom, that a steady heart rate and less than 75bpm were the criteria for a patient to be scanned with the low dose prospective cardiac CT technology. The phantom was then used to test stent imaging technologies in CT and interventional fluoroscopy as well as stenosis and lipid volume measurements for Aim 4. Plaque fabrication was also successfully completed for the heart phantom, and expanding the heart phantom's utility to include the effects of calcium plaques on soft plaque classification would be worthwhile. The results for lipid volume presented here include the confounding effects of iodine and radiation dose but would benefit from calcium plaques present in the heart phantom. Known percent stenosis calcium plaques could also be used in the heart phantom for increasing the number of phantom trials that validate the virtual non-calcium images tested here for calcium blooming artifact correction. The clinical cases reviewed here had a few instances of soft plaques in direct contact with highly attenuating calcium, and patient lipid volume classification would be more robust if it accounted for dense calcium.

7.2 Aim 2: Coronary Calcium Plaque Scores with Dual Energy CT Angiography

The conventional Agatston score was validated here for the first time from a CT angiogram using a dual energy acquisition. My method obtained an Agatston score from one iodinated dual energy scan with ±11% error (Bland-Altman) after testing the method on eleven patient coronary arteries. One possible source of error was discovered when scanning the Cardio CT Phantom, from Quality Assurance in Radiology and Medicine (QRM), used to compare Agatston calcium scores from different vendors, different post-processing computers, and different operators (McCollough et al. 2007; QRM 2006). The QRM Cardio CT Phantom has inserts with three different diameters and three different HAP densities 200mg/cc, 400mg/cc, and 800mg/cc. While comparing 120kVp, 70keV, and Calcium(Iodine) images of the QRM Cardio CT Phantom, it was discovered that the lowest density HAP inserts were not present in the Calcium(Iodine) images as shown in Figure 7.1.

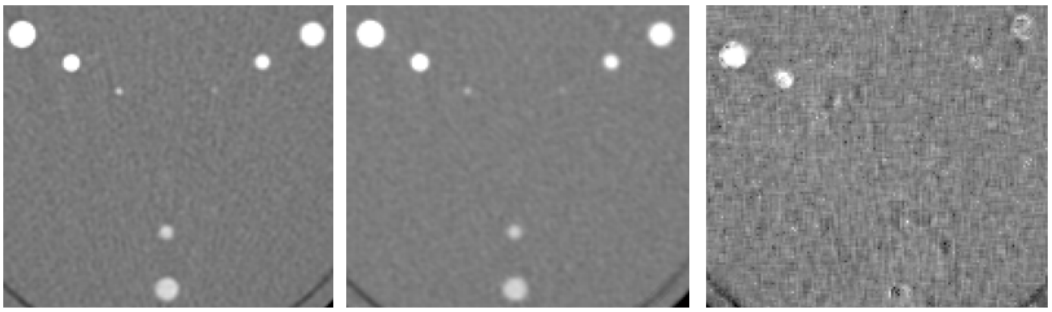

Figure 7.1: The QRM Cardio CT Phantom is prepared with the calcium HAP inserts. In each image, the three top left inserts are all 800mg/cc HAP; the three top right inserts are all 400mg/cc HAP; and the three bottom inserts are all 200mg/cc.

Derivation of the Calcium(Iodine) image type includes several input parameters, including elemental calcium density and elemental calcium attenuation values representative of the density specified. Future tests could incorporate varying levels of elemental calcium density, which could change the presence or absence of calcium pixels in the Calcium(Iodine) image. Once a value is chosen for elemental calcium density that appropriately assigns calcium pixels, the error seen

with my method could be reduced. My method would also benefit from testing on more patient coronary arteries as the Agatston score is an established clinic score for diagnosis and prognosis of coronary calcium disease.

7.3 Aim 3: Calcium Blooming Artifact Correction with Dual Energy CT Angiography

Coronary artery stenosis evaluation is not possible in the presence of severe calcium blooming artifacts, and dense calcium that causes blooming is common among patients presenting with symptoms indicative of a coronary event. My work conveys for the first time the major factor that causes the blooming artifact. Window and level settings are the major factors that cause the calcium blooming artifact. The virtual non-calcium images, tested for Aim 3, correct for the calcium blooming artifact by removing calcium from the image, but my method has not been improved with reduced image noise or tested against the gold standard of coronary fluoroscopic angiography. Since the completion of my tests with virtual non-calcium images, significant noise suppression algorithms have been developed that would greatly increase the image quality of virtual non-calcium images as well as lowering the radiation dose required to obtain the dual energy images. Aim 3 would also benefit from performing fluoroscopic comparisons on patients and additional controlled comparisons on fabricated calcified vessel phantoms.

7.4 Aim 4: Coronary Soft Plaque Vulnerability Characterization with CT Angiography

My work for Aim 4 achieves a percent lipid volume that accounts for iodine content between 200HU and 350HU. Using the multiple feature SVM model improves upon the 17% misclassification error measured with 120kVp images and achieves 4% misclassification error with the combination of virtual monochromatic and material basis images. The percent lipid volume could be used clinically for risk of a coronary event because lipid volumes above 40% are more vulnerable to rupture. However, the tests performed here were on patient data with 300HU

iodine content and subsequent patients have had iodine values as high as 600HU. In fact, the patient used to demonstrate the use of the SVM model had a scan with both 300HU and 600HU iodine content. Figure 7.2 shows classification on both scans produced different lipid volume percentages in the presence of elevated iodine content.

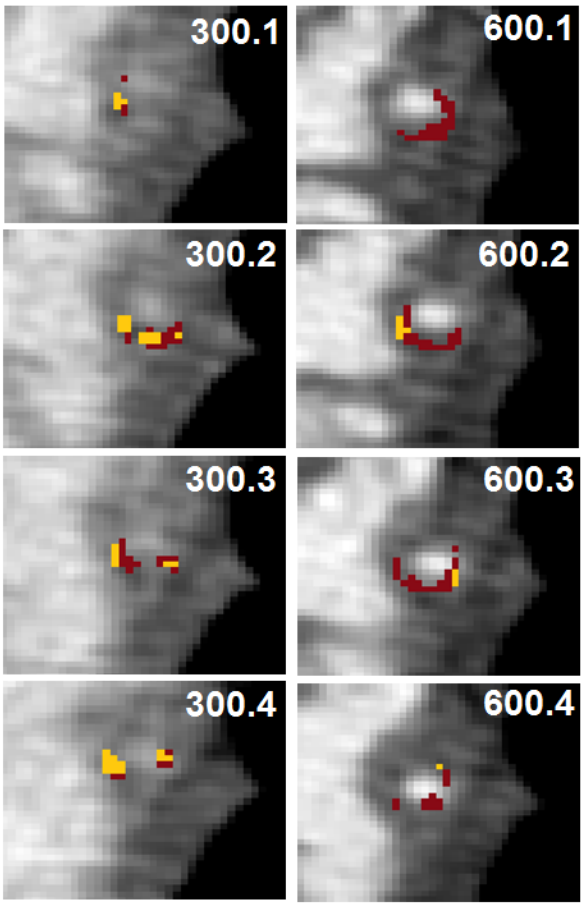

Figure 7.2: Results from SVM classifier run on same patient with a data set of 300HU (left) iodine content and 600HU (right) iodine content.

With 300HU iodine content surrounding the patient soft plaque, the SVM model classifies 35% of the plaque to be lipid whereas 13% are classified lipid when there is 600HU iodine content present. Previous studies and my own comparisons show the dependence of soft plaque attenuation measurements on plaque location in the gantry, amount of plaque present, and iodine concentration present. Future work would aim to more accurately measure lipid content with

individual models for varying iodine content present. For instance, my model already measures the iodine present to exclude iodine pixels from classification but it could also apply an SVM model with iodine content training data representative of the iodine measured. Non-invasive risk assessment of coronary soft plaques could be achieved for the first time with the use of SVM models like the one presented here and SVM models that account for varying iodine content from patient to patient.

REFERENCES

Abela, G. S. 2010. Cholesterol crystals piercing the arterial plaque and intima trigger local and systemic inflammation. *Journal of clinical lipidology* 4 (3):156-64.

Repeated Author. 2010. Cholesterol crystals piercing the arterial plaque and intima trigger local and systemic inflammation. *J Clin Lipidol* 4 (3):156-64.

Abela, G. S., K. Aziz, A. Vedre, D. R. Pathak, J. D. Talbott, and J. Dejong. 2009. Effect of cholesterol crystals on plaques and intima in arteries of patients with acute coronary and cerebrovascular syndromes. *The American journal of cardiology* 103 (7):959-68.

Achenbach, S., F. Moselewski, D. Ropers, M. Ferencik, U. Hoffmann, B. MacNeill, K. Pohle, U. Baum, K. Anders, I. K. Jang, W. G. Daniel, and T. J. Brady. 2004. Detection of calcified and noncalcified coronary atherosclerotic plaque by contrast-enhanced, submillimeter multidetector spiral computed tomography: a segment-based comparison with intravascular ultrasound. *Circulation* 109 (1):14-7.

Achenbach, S., D. Ropers, A. Kuettner, T. Flohr, B. Ohnesorge, H. Bruder, H. Theessen, M. Karakaya, W. G. Daniel, W. Bautz, W. A. Kalender, and K. Anders. 2006. Contrast-enhanced coronary artery visualization by dual-source computed tomography--initial experience. *European Journal of Radiology* 57 (3):331-5.

Agatston, A. S., W. R. Janowitz, F. J. Hildner, N. R. Zusmer, M. Viamonte, Jr., and R. Detrano. 1990. Quantification of coronary artery calcium using ultrafast computed tomography. *J Am Coll Cardiol* 15 (4):827-32.

Alderson-Phantoms. *Anthropomorphic Radiation Therapy Phantom* [Online Manual] 2006 [cited June 10, 2009.

Alvarez, R. E., and A. Macovski. 1976. Energy-Selective Reconstructions in X-Ray Computerized Tomography. *Physics in Medicine and Biology* 21 (5):733-744.

Barreto, M., P. Schoenhagen, A. Nair, S. Amatangelo, M. Milite, N. A. Obuchowski, M. L. Lieber, and S. S. Halliburton. 2008. Potential of dual-energy computed tomography to characterize atherosclerotic plaque: ex vivo assessment of human coronary arteries in comparison to histology. *J Cardiovasc Comput Tomogr* 2 (4):234-42.

Becker, C. R., T. Kleffel, A. Crispin, A. Knez, J. Young, U. J. Schoepf, R. Haberl, and M. F. Reiser. 2001. Coronary artery calcium measurement: agreement of multirow detector and electron beam CT. *AJR Am J Roentgenol* 176 (5):1295-8.

Boas, E, and D Fleischmann. 2012. CT Artifacts: Causes and Reduction Techniques. *Imaging in Medicine* 4 (2):229-240.

Boll, D. T., E. M. Merkle, E. K. Paulson, R. A. Mirza, and T. R. Fleiter. 2008. Calcified vascular plaque specimens: Assessment with cardiac dual-energy multidetector CT in anthropomorphically moving heart phantom. *Radiology* 249 (1):119-126.

Boltz, T., W. Pavlicek, R. Paden, M. Renno, A. Jensen, and M. Akay. 2010. An anthropomorphic beating heart phantom for cardiac x-ray CT imaging evaluation. *J Appl Clin Med Phys* 11 (1):3129.

Brodoefel, H., C. Burgstahler, M. Heuschmid, A. Reimann, F. Khosa, A. Kopp, S. Schroeder, C. D. Claussen, and M. E. Clouse. 2009. Accuracy of dual-source CT in the characterisation of non-calcified plaque: use of a colour-coded analysis compared with virtual histology intravascular ultrasound. *Br J Radiol* 82 (982):805-12.

Brodoefel, H., C. Burgstahler, A. Sabir, C. S. Yam, F. Khosa, C. D. Claussen, and M. E. Clouse. 2009. Coronary plaque quantification by voxel analysis: dual-source MDCT angiography versus intravascular sonography. *AJR Am J Roentgenol* 192 (3):W84-9.

Brodoefel, H., C. Burgstahler, I. Tsiflikas, A. Reimann, S. Schroeder, C. D. Claussen, M. Heuschmid, and A. F. Kopp. 2008. Dual-source CT: effect of heart rate, heart rate variability, and calcification on image quality and diagnostic accuracy. *Radiology* 247 (2):346-355.

Brodoefel, H., A. Reimann, M. Heuschmid, I. Tsiflikas, A. F. Kopp, S. Schroeder, C. D. Claussen, M. E. Clouse, and C. Burgstahler. 2008. Characterization of coronary atherosclerosis by dual-source computed tomography and HU-based color mapping: a pilot study. *Eur Radiol* 18 (11):2466-74.

Budoff, M. J., M. C. Cohen, M. J. Garcia, J. M. Hodgson, W. G. Hundley, J. A. C. Lima, W. J. Manning, G. M. Pohost, P. M. Raggi, G. P. Rodgers, J. A. Rumberger, A. J. Taylor, M. A. Creager, J. W. Hirshfeld, B. H. Lorell, G. Merli, G. P. Rodgers, C. M. Tracy, and H. H. Weitz. 2005. ACCF/AHA clinical competence statement on cardiac imaging with computed tomography and magnetic resonance - A report of the American College of Cardiology Foundation/American Heart Association/American college of Physicians Task Force on clinical competence and training. *Circulation* 112 (4):598-617.

Burke, A. P., A. Farb, G. T. Malcom, Y. H. Liang, J. Smialek, and R. Virmani. 1997. Coronary risk factors and plaque morphology in men with coronary disease who died suddenly. *N Engl J Med* 336 (18):1276-82.

Choi, H. S., B. W. Choi, K. O. Choe, D. H. Choi, K. J. Yoo, M. I. Kim, and J. Kim. 2004. Pitfalls, artifacts, and remedies in multi-detector row CT coronary angiography. *Radiographics* 24 (3):787-800.

Clavijo, C, and N Pelc. 2009. Image-Quality Optimization for Dual Energy Computed Tomography (DECT) Three-Material Decomposition. *Revista Ingenieria Biomedica* 3 (5):33-42.

Dalager, M. G., M. Bottcher, G. Andersen, J. Thygesen, E. M. Pedersen, L. Dejbjerg, O. Gotzsche, and H. E. Botker. 2011. Impact of luminal density on plaque classification by CT coronary angiography. *Int J Cardiovasc Imaging* 27 (4):593-600.

Dassault-Systemes-SolidWorks. *Solidworks Premium Computer Aided Desgin 2008* [Online Manual] 2008 [cited August 4, 2009. Available from http://files.solidworks.com/supportfiles/Whats_new/2008/English/whatsnew.pdf

Farb, A., A. P. Burke, A. L. Tang, T. Y. Liang, P. Mannan, J. Smialek, and R. Virmani. 1996. Coronary plaque erosion without rupture into a lipid core. A frequent cause of coronary thrombosis in sudden coronary death. *Circulation* 93 (7):1354-63.

Ferencik, M., A. Ferullo, S. Achenbach, S. Abbara, R. C. Chan, S. L. Booth, T. J. Brady, and U. Hoffmann. 2003. Coronary calcium quantification using various calibration phantoms and scoring thresholds. *Invest Radiol* 38 (9):559-66.

Finn, A. V., M. Nakano, J. Narula, F. D. Kolodgie, and R. Virmani. 2010. Concept of vulnerable/unstable plaque. *Arterioscler Thromb Vasc Biol* 30 (7):1282-92.

Flohr, T. G., and B. M. Ohnesorge. 2008. Imaging of the heart with computed tomography. *Basic Res Cardiol* 103 (2):161-73.

Funabashi, N., Y. Kobayashi, M. Kudo, M. Asano, K. Teramoto, I. Komuro, and G. D. Rubin. 2004. New method of measuring coronary diameter by electron-beam computed tomographic angiography using adjusted thresholds determined by calibration with aortic opacity. *Circulation Journal* 68 (8):769-777.

Fuster, Valentin. 2008. *Hurst's the heart: Biology of the Vessel Wall*. 12th ed. xxxi, 2477, I-63 p. in 2 vols. New York: McGraw-Hill Medical.

Repeated Author. 2008. *Hurst's the heart: The Burden of Increasing Worldwide Cardiovascular Disease*. 12th ed. xxxi, 2477, I-63 p. in 2 vols. New York: McGraw-Hill Medical.

Ge, J., F. Chirillo, J. Schwedtmann, G. Gorge, M. Haude, D. Baumgart, V. Shah, C. von Birgelen, S. Sack, H. Boudoulas, and R. Erbel. 1999. Screening of ruptured plaques in patients with coronary artery disease by intravascular ultrasound. *Heart* 81 (6):621-7.

Gerber, B. L., B. Belge, G. J. Legros, P. Lim, A. Poncelet, A. Pasquet, G. Gisellu, E. Coche, and J. L. Vanoverschelde. 2006. Characterization of acute and chronic myocardial infarcts by multidetector computed tomography: comparison with contrast-enhanced magnetic resonance. *Circulation* 113 (6):823-33.

Gerber, T, B Kantor, and E Williamson. 2007. Computed Tomography of the Cardiovascular System. *Informa Healthcare*.

Gerber, T. C., J. J. Carr, A. E. Arai, R. L. Dixon, V. A. Ferrari, A. S. Gomes, G. V. Heller, C. H. McCollough, M. F. McNitt-Gray, F. A. Mettler, J. H. Mieres, R. L. Morin, and M. V. Yester. 2009. Ionizing radiation in cardiac imaging: a science advisory from the American Heart Association Committee on Cardiac Imaging of the Council on Clinical Cardiology and Committee on Cardiovascular Imaging and Intervention of the Council on Cardiovascular Radiology and Intervention. *Circulation* 119 (7):1056-65.

Glazebrook, K. N., L. S. Guimaraes, N. S. Murthy, D. F. Black, T. Bongartz, N. J. Manek, S. Leng, J. G. Fletcher, and C. H. McCollough. 2011. Identification of intraarticular and periarticular uric acid crystals with dual-energy CT: initial evaluation. *Radiology* 261 (2):516-24.

Goodsitt, M. M., E. G. Christodoulou, and S. C. Larson. 2011. Accuracies of the synthesized monochromatic CT numbers and effective atomic numbers obtained with a rapid kVp switching dual energy CT scanner. *Medical Physics* 38 (4):2222-2232.

Gouya, H., O. Varenne, L. Trinquart, E. Touze, O. Vignaux, C. Spaulding, J. L. Mas, and J. L. Sablayrolles. 2009. Coronary artery stenosis in high-risk patients: 64-section CT and coronary angiography--prospective study and analysis of discordance. *Radiology* 252 (2):377-85.

Greenland, P., R. O. Bonow, B. H. Brundage, M. J. Budoff, M. J. Eisenberg, S. M. Grundy, M. S. Lauer, W. S. Post, P. Raggi, R. F. Redberg, G. P. Rodgers, L. J. Shaw, A. J. Taylor, and

W. S. Weintraub. 2007. ACCF/AHA 2007 clinical expert consensus document on coronary artery calcium scoring by computed tomography in global cardiovascular risk assessment and in evaluation of patients with chest pain: a report of the American College of Cardiology Foundation Clinical Expert Consensus Task Force (ACCF/AHA Writing Committee to Update the 2000 Expert Consensus Document on Electron Beam Computed Tomography) developed in collaboration with the Society of Atherosclerosis Imaging and Prevention and the Society of Cardiovascular Computed Tomography. *J Am Coll Cardiol* 49 (3):378-402.

Greuter, M. J. W., J. Dorgelo, W. G. J. Tukker, and M. Oudkerk. 2005. Study on motion artifacts in coronary arteries with an anthropomorphic moving heart phantom on an ECG-gated multidetector computed tomography unit. *European Radiology* 15 (5):995-1007.

Groen, J. M., M. J. Greuter, R. Vliegenthart, C. Suess, B. Schmidt, F. Zijlstra, and M. Oudkerk. 2008. Calcium scoring using 64-slice MDCT, dual source CT and EBT: a comparative phantom study. *Int J Cardiovasc Imaging* 24 (5):547-56.

Guilbert, J. J. 2003. The world health report 2002 - reducing risks, promoting healthy life. *Educ Health (Abingdon)* 16 (2):230.

Halliburton, S. S., A. E. Stillman, and R. D. White. 2002. Noninvasive quantification of coronary artery calcification: methods and prognostic value. *Cleve Clin J Med* 69 Suppl 3:S6-11.

Halpern, E. J., D. J. Halpern, J. H. Yanof, S. Amin-Spector, D. Fischman, G. Aviram, and J. Sosna. 2009. Is coronary stent assessment improved with spectral analysis of dual energy CT? *Acad Radiol* 16 (10):1241-50.

Hausleiter, J., T. Meyer, M. Hadamitzky, A. Kastrati, S. Martinoff, and A. Schomig. 2006. Prevalence of noncalcified coronary plaques by 64-slice computed tomography in patients with an intermediate risk for significant coronary artery disease. *J Am Coll Cardiol* 48 (2):312-8.

Hausleiter, J., T. Meyer, F. Hermann, M. Hadamitzky, M. Krebs, T. C. Gerber, C. McCollough, S. Martinoff, A. Kastrati, A. Schomig, and S. Achenbach. 2009. Estimated radiation dose associated with cardiac CT angiography. *JAMA* 301 (5):500-7.

Heron, M. 2012. Deaths: leading causes for 2008. *Natl Vital Stat Rep* 60 (6):1-94.

Hoffmann, M. H., H. Shi, B. L. Schmitz, F. T. Schmid, M. Lieberknecht, R. Schulze, B. Ludwig, U. Kroschel, N. Jahnke, W. Haerer, H. J. Brambs, and A. J. Aschoff. 2005. Noninvasive coronary angiography with multislice computed tomography. *JAMA* 293 (20):2471-8.

Hong, C., C. R. Becker, U. J. Schoepf, B. Ohnesorge, R. Bruening, and M. F. Reiser. 2002. Coronary artery calcium: absolute quantification in nonenhanced and contrast-enhanced multi-detector row CT studies. *Radiology* 223 (2):474-80.

Hong, C., T. K. Pilgram, F. Zhu, and K. T. Bae. 2004. Is coronary artery calcium mass related to Agatston score? *Acad Radiol* 11 (3):286-92.

Hongzong, S., W. Tao, Y. Xiaojun, L. Huanxiang, H. Zhide, L. Mancang, and F. BoTao. 2007. Support vector machines classification for discriminating coronary heart disease patients from non-coronary heart disease. *The West Indian medical journal* 56 (5):451-7.

Horiguchi, J., C. Fujioka, M. Kiguchi, Y. Shen, C. E. Althoff, H. Yamamoto, and K. Ito. 2007. Soft and intermediate plaques in coronary arteries: how accurately can we measure CT attenuation using 64-MDCT? *AJR Am J Roentgenol* 189 (4):981-8.

Horiguchi, J., H. Yamamoto, N. Hirai, Y. Akiyama, C. Fujioka, K. Marukawa, H. Fukuda, and K. Ito. 2006. Variability of repeated coronary artery calcium measurements on low-dose ECG-gated 16-MDCT. *AJR Am J Roentgenol* 187 (1):W1-6.

Johnson, T. R., B. Krauss, M. Sedlmair, M. Grasruck, H. Bruder, D. Morhard, C. Fink, S. Weckbach, M. Lenhard, B. Schmidt, T. Flohr, M. F. Reiser, and C. R. Becker. 2007. Material differentiation by dual energy CT: initial experience. *European Radiology* 17 (6):1510-7.

Kitagawa, T., H. Yamamoto, J. Horiguchi, N. Ohhashi, F. Tadehara, T. Shokawa, Y. Dohi, E. Kunita, H. Utsunomiya, N. Kohno, and Y. Kihara. 2009. Characterization of noncalcified coronary plaques and identification of culprit lesions in patients with acute coronary syndrome by 64-slice computed tomography. *JACC Cardiovasc Imaging* 2 (2):153-60.

Kolodgie, F. D., A. P. Burke, A. Farb, D. K. Weber, R. Kutys, T. N. Wight, and R. Virmani. 2002. Differential accumulation of proteoglycans and hyaluronan in culprit lesions: insights into plaque erosion. *Arterioscler Thromb Vasc Biol* 22 (10):1642-8.

Kolodgie, F. D., A. P. Burke, G. Nakazawa, and R. Virmani. 2007. Is pathologic intimal thickening the key to understanding early plaque progression in human atherosclerotic disease? *Arterioscler Thromb Vasc Biol* 27 (5):986-9.

Kristensen, T. S., T. Engstrom, H. Kelbaek, P. von der Recke, M. B. Nielsen, and K. F. Kofoed. 2010. Correlation between coronary computed tomographic angiography and fractional flow reserve. *Int J Cardiol* 144 (2):200-5.

Lau, G. T., L. J. Ridley, M. C. Schieb, D. B. Brieger, S. B. Freedman, L. A. Wong, S. K. Lo, and L. Kritharides. 2005. Coronary artery stenoses: Detection with calcium scoring, CT angiography, and both methods combined. *Radiology* 235 (2):415-422.

Leber, A. W., A. Knez, F. von Ziegler, A. Becker, K. Nikolaou, S. Paul, B. Wintersperger, M. Reiser, C. R. Becker, G. Steinbeck, and P. Boekstegers. 2005. Quantification of obstructive and nonobstructive coronary lesions by 64-slice computed tomography - A comparative study with quantitative coronary angiography and intravascular ultrasound. *Journal of the American College of Cardiology* 46 (1):147-154.

Leschka, S., H. Scheffel, L. Desbiolles, A. Plass, O. Gaemperli, P. Stolzmann, M. Genoni, T. Luescher, B. Marincek, P. Kaufmann, and H. Alkadhi. 2008. Combining dual-source computed tomography coronary angiography and calcium scoring: added value for the assessment of coronary artery disease. *Heart* 94 (9):1154-61.

Liaw, A, and M Wiener. 2002. Classification and Regression by randomForest. *R News* 2 (3):18-22.

Litt, H. I., C. Gatsonis, B. Snyder, H. Singh, C. D. Miller, D. W. Entrikin, J. M. Leaming, L. J. Gavin, C. B. Pacella, and J. E. Hollander. 2012. CT angiography for safe discharge of patients with possible acute coronary syndromes. *The New England journal of medicine* 366 (15):1393-403.

Mah, E., E. Samei, and D. J. Peck. 2001. Evaluation of a quality control phantom for digital chest radiography. *J Appl Clin Med Phys* 2 (2):90-101.

Maintz, D., M. C. Burg, H. Seifarth, A. C. Bunck, M. Ozgun, R. Fischbach, K. U. Jurgens, and W. Heindel. 2009. Update on multidetector coronary CT angiography of coronary stents: in vitro evaluation of 29 different stent types with dual-source CT. *Eur Radiol* 19 (1):42-9.

Mayo, J. R., and J. A. Leipsic. 2009. Radiation Dose in Cardiac CT (vol 192, pg 646, 2009). *American Journal of Roentgenology* 192 (5):1167-1167.

McCollough, C. H., S. Ulzheimer, S. S. Halliburton, K. Shanneik, R. D. White, and W. A. Kalender. 2007. Coronary artery calcium: a multi-institutional, multimanufacturer international standard for quantification at cardiac CT. *Radiology* 243 (2):527-38.

Motoyama, S., M. Sarai, H. Harigaya, H. Anno, K. Inoue, T. Hara, H. Naruse, J. Ishii, H. Hishida, N. D. Wong, R. Virmani, T. Kondo, Y. Ozaki, and J. Narula. 2009. Computed tomographic angiography characteristics of atherosclerotic plaques subsequently resulting in acute coronary syndrome. *J Am Coll Cardiol* 54 (1):49-57.

Muhlenbruch, G., J. E. Wildberger, R. Koos, M. Das, T. G. Flohr, M. Niethammer, C. Weiss, R. W. Gunther, and A. H. Mahnken. 2005. Coronary calcium scoring using 16-row multislice computed tomography: nonenhanced versus contrast-enhanced studies in vitro and in vivo. *Invest Radiol* 40 (3):148-54.

Nagao, M., H. Matsuoka, H. Kawakami, H. Higashino, T. Mochizuki, K. Murase, and M. Uemura. 2008. Quantification of myocardial perfusion by contrast-enhanced 64-MDCT: characterization of ischemic myocardium. *AJR Am J Roentgenol* 191 (1):19-25.

Nair, A., B. D. Kuban, E. M. Tuzcu, P. Schoenhagen, S. E. Nissen, and D. G. Vince. 2002. Coronary plaque classification with intravascular ultrasound radiofrequency data analysis. *Circulation* 106 (17):2200-6.

Nakanishi, T., Y. Kayashima, R. Inoue, K. Sumii, and Y. Gomyo. 2005. Pitfalls in 16-detector row CT of the coronary arteries. *Radiographics* 25 (2):425-438.

National-Instruments. *NI LabVIEW base development system for WIndows* [Online Manual] 2005 [cited June 10, 2009. Available from http://sine.ni.com/nips/cds/print/p/lang/en/nid/1385.

Nikolaou, K., S. Sagmeister, A. Knez, E. Klotz, B. J. Wintersperger, C. R. Becker, and M. F. Reiser. 2003. Multidetector-row computed tomography of the coronary arteries: predictive value and quantitative assessment of non-calcified vessel-wall changes. *Eur Radiol* 13 (11):2505-12.

Nissen, S. E. 2008. Limitations of computed tomography coronary angiography. *J Am Coll Cardiol* 52 (25):2145-7.

NIST. *Tables of X-Ray Mass Attenuation Coefficients and Mass-Energy Absorption Coefficients* [Online Table]. National Institute of Instruments and Standards 1996 [cited November 6, 2012. Available from http://www.nist.gov/physlab/data/xraycoef/index.cfm.

O'Brien, A. P., M. B. Srichai, E. M. Hecht, D. C. Kim, and F. E. Jacobs. 2007. Anatomy of the heart at multidetector CT: What the radiologist needs to know. *Radiographics* 27 (6):1569-1582.

Pack, J, D Langan, X Wu, D Wu, W Pavlicek, and T Boltz. 2009. Fast kVp Switching CT Imaging of a Dynamic Cardiac Phantom. Paper read at SPIE Medical Imaging.

Park, K, M Akay, P Pavlicek, T Boltz, and R Paden. 2009. Image-based Dual Energy CT Improvements Using Gram-Schmidt Method. In *SPIE Medical Imaging*: SPIE Medical Imaging.

Pavlicek, W, T Boltz, J Collins, J Gruden, A Hara, G Paden, and A Silva. 2009. Dual Energy Histology: Use of GSI Viewer with Fast Switched Dual Energy Computed Tomography. edited by I. M. Clinic.

Pavlicek, W, T Boltz, K Park, R Paded, M Peter, and J Leverentz. 2008. Lipid Plaque Phantom Design and Fabrication. In *RSNA*: RSNA.

Pavlicek, W, P Panse, A Hara, and T Boltz. 2010. Initial Use of Fast Switched Dual Energy CT for Coronary Artery Disease. Paper read at SPIE Medical Imaging.

Pohle, K., S. Achenbach, B. Macneill, D. Ropers, M. Ferencik, F. Moselewski, U. Hoffmann, T. J. Brady, I. K. Jang, and W. G. Daniel. 2007. Characterization of non-calcified coronary atherosclerotic plaque by multi-detector row CT: comparison to IVUS. *Atherosclerosis* 190 (1):174-80.

QRM, Quality Assurance in Radiology and Medicine:. *Anthropomorphic Cardio CT Phantom* [Online Manual] 2006 [cited August 13, 2013. Available from http://www.qrm.de/content/pdf/QRM-Cardio-Phantom.pdf.

Raff, G. L., M. J. Gallagher, W. O'Neill, and J. A. Goldstein. 2005. Diagnostic accuracy of noninvasive coronary angiography using 64-slice spiral computed tomography. *Journal of the American College of Cardiology* 46 (3):552-557.

Ropers, D., U. Baum, K. Pohle, K. Anders, S. Ulzheimer, B. Ohnesorge, C. Schlundt, W. Bautz, W. G. Daniel, and S. Achenbach. 2003. Detection of coronary artery stenoses with thin-slice multi-detector row spiral computed tomography and multiplanar reconstruction. *Circulation* 107 (5):664-6.

Rumberger, J. A., D. B. Simons, L. A. Fitzpatrick, P. F. Sheedy, and R. S. Schwartz. 1995. Coronary artery calcium area by electron-beam computed tomography and coronary atherosclerotic plaque area. A histopathologic correlative study. *Circulation* 92 (8):2157-62.

Sajjadieh, A, A Hekmatnia, and M Keivani. 2013. Diagnostic performance of 64-row coronary CT angiography in detecting significant stenosis as compared with conventional invasive coronary angiography. *ARYA Atherosclerosis* 9 (2):157-163.

Santamaria-Pang, A, S Dutta, S Makrogiannis, A Hara, W Pavlicek, A Silva, B Thomsen, S Robertson, D Okerlund, D Langan, and R Bhotika. 2010. Automated Liver Lesion Characterization using fast kVp switching Dual Energy Computed Tomography Imaging. Paper read at SPIE Medical Imaging.

Sarwar, A., L. J. Shaw, M. D. Shapiro, R. Blankstein, U. Hoffmann, R. C. Cury, S. Abbara, T. J. Brady, M. J. Budoff, R. S. Blumenthal, and K. Nasir. 2009. Diagnostic and prognostic value of absence of coronary artery calcification. *JACC Cardiovasc Imaging* 2 (6):675-88.

Sato, A., M. Hiroe, M. Tamura, H. Ohigashi, T. Nozato, H. Hikita, A. Takahashi, K. Aonuma, and M. Isobe. 2008. Quantitative measures of coronary stenosis severity by 64-Slice CT angiography and relation to physiologic significance of perfusion in nonobese patients: comparison with stress myocardial perfusion imaging. *Journal of nuclear medicine : official publication, Society of Nuclear Medicine* 49 (4):564-72.

Schaar, J. A., F. Mastik, E. Regar, C. A. den Uil, F. J. Gijsen, J. J. Wentzel, P. W. Serruys, and A. F. van der Stehen. 2007. Current diagnostic modalities for vulnerable plaque detection. *Curr Pharm Des* 13 (10):995-1001.

Schmermund, A., S. Mohlenkamp, and R. Erbel. 2003. Coronary artery calcium and its relationship to coronary artery disease. *Cardiol Clin* 21 (4):521-34.

Schoenhagen, P., M. Barreto, and S. S. Halliburton. 2008. Quantitative plaque characterization with coronary CT angiography (CTA): current challenges and future application in atherosclerosis trials and clinical risk assessment. *Int J Cardiovasc Imaging* 24 (3):313-6.

Schroeder, S., A. Kuettner, M. Leitritz, J. Janzen, A. F. Kopp, C. Herdeg, M. Heuschmid, C. Burgstahler, A. Baumbach, M. Wehrmann, and C. D. Claussen. 2004. Reliability of differentiating human coronary plaque morphology using contrast-enhanced multislice spiral computed tomography: a comparison with histology. *J Comput Assist Tomogr* 28 (4):449-54.

Shah, P. K. 2003. Mechanisms of plaque vulnerability and rupture. *J Am Coll Cardiol* 41 (4 Suppl S):15S-22S.

Shelley-Medical-Imaging-Technologies. *Dynamic Multi-Modality Heart Phantom* [Online Manual] 2006 [cited June 9, 2009. Available from http://www.simutec.com/Media/pumps/Dynamic_Heart_Phantom_Brochure_LR.pdf.

Sun, J., Z. Zhang, B. Lu, W. Yu, Y. Yang, Y. Zhou, Y. Wang, and Z. Fan. 2008. Identification and quantification of coronary atherosclerotic plaques: a comparison of 64-MDCT and intravascular ultrasound. *AJR Am J Roentgenol* 190 (3):748-54.

Tkaczyk, E, and D Langan. 2009. Quantization of Liver Tissue in Fast Switched Dual kVp Computed Tomography Using Linear Discriminant Analysis. Paper read at SPIE Medical Imaging.

Tran, D. N., M. Straka, J. E. Roos, S. Napel, and D. Fleischmann. 2009. Dual-energy CT Discrimination of Iodine and Calcium: Experimental Results and Implications for Lower Extremity CT Angiography. *Academic Radiology* 16 (2):160-171.

Ulzheimer, S., and W. A. Kalender. 2003. Assessment of calcium scoring performance in cardiac computed tomography. *Eur Radiol* 13 (3):484-97.

Versluis, A., A. J. Bank, and W. H. Douglas. 2006. Fatigue and plaque rupture in myocardial infarction. *J Biomech* 39 (2):339-47.

Virmani, R., A. P. Burke, A. Farb, and F. D. Kolodgie. 2006. Pathology of the vulnerable plaque. *J Am Coll Cardiol* 47 (8 Suppl):C13-8.

Virmani, R., F. D. Kolodgie, A. P. Burke, A. Farb, and S. M. Schwartz. 2000. Lessons from sudden coronary death: a comprehensive morphological classification scheme for atherosclerotic lesions. *Arterioscler Thromb Vasc Biol* 20 (5):1262-75.

Xu, D, D Langan, X Wu, J Pack, T Benson, A Schmitz, and E Tkaczyk. 2009. Dual Energy CT via Fast kVp Switching Spectrum Estimation. Paper read at SPIE Medical Imaging.

Yamak, D, W Pavlicek, T Boltz, P Panse, and M Akay. 2013. Coronary calcium quantification using contrast-enhanced dual energy computed tomography. *Journal of Applied Clinical Medical Physics*.

Yang, W. I., J. Hur, Y. G. Ko, B. W. Choi, J. S. Kim, D. Choi, J. W. Ha, M. K. Hong, Y. Jang, N. Chung, W. H. Shim, and S. Y. Cho. 2010. Assessment of tissue characteristics of noncalcified coronary plaques by 64-slice computed tomography in comparison with integrated backscatter intravascular ultrasound. *Coron Artery Dis* 21 (3):168-74.

Yusuf, S., S. Hawken, S. Ounpuu, T. Dans, A. Avezum, F. Lanas, M. McQueen, A. Budaj, P. Pais, J. Varigos, and L. Lisheng. 2004. Effect of potentially modifiable risk factors associated with myocardial infarction in 52 countries (the INTERHEART study): case-control study. *Lancet* 364 (9438):937-52.

Zachrisson, H., E. Engstrom, J. Engvall, L. Wigstrom, O. Smedby, and A. Persson. 2010. Soft tissue discrimination ex vivo by dual energy computed tomography. *Eur J Radiol* 75 (2):e124-8.

Zhang, S., D. C. Levin, E. J. Halpern, D. Fischman, M. Savage, and P. Walinsky. 2008. Accuracy of MDCT in assessing the degree of stenosis caused by calcified coronary artery plaques. *AJR Am J Roentgenol* 191 (6):1676-83.